Field-Theoretical Studies of a Doped Mott Insulator

ISBN: 90-393-4266-0

Field-Theoretical Studies of a Doped Mott Insulator

Veldentheoretische Studie van een Gedoteerde Mott Isolator

(met een samenvatting in het Nederlands)

Proefschrift

ter verkrijging van de graad van doctor aan de Universiteit Utrecht op gezag van de Rector Magnificus, Prof. dr. W. H. Gispen, ingevolge het besluit van het College voor Promoties in het openbaar te verdedigen op donderdag 22 juni 2006 des middags te 12.45 uur

door

Vladimir Juričić

geboren op 4 juni 1976, te S. Palanka, Servië

promotor:

Prof. dr. C. Morais Smith

Instituut voor Theoretische Fysica
Departement Natuur- en Sterrenkunde
Faculteit Bètawetenschappen
Universiteit Utrecht

Dedicated to my parents, Branislav and Mira

Contents

Chapter 1

Introduction

Conventional (low-temperature) superconductors

The phenomenon of superconductivity was discovered in 1911 by the Dutch physicist Heike Kamerlingh Onnes [1]. He observed that the electrical resistivity of mercury suddenly disappeared when the metal was cooled below the critical temperature of 4.2K, see Fig. 1.1. He also discovered that superconductivity disappears when the current exceeds a critical value, or above a critical value of an externally applied magnetic field. Later, in 1933 Meissner and Ochsenfeld found that a superconductor completely expels the externally applied magnetic field, i.e., it is an ideal diamagnet [2]. This effect is known as Meissner effect.

More than 40 years have passed before a consistent microscopic theory of superconductivity has been formulated. Early theoretical studies concentrated on the macroscopic aspects of the phenomenon. In 1934, Gorter and Casimir explained the thermodynamic features of superconductivity [3], whereas London and London, in 1935, established a theory that could explain the electrodynamic properties of a superconductor [4, 5]. A phenomenological theory of superconductivity, valid in the vicinity of the critical temperature, has been proposed by Ginzburg and Landau in 1950 [6]. Two crucial experimental observations that led towards the microscopic theory of superconductivity are the isotope effect and the direct observation of the bandgap. The former led Fröhlich in 1950 to propose the electron-phonon interaction as responsible for superconductivity [7]. But it was only in 1957 that John Bardeen, Leon Cooper, and Robert Schrieffer formulated the microscopic theory of superconductivity, the so-called BCS theory [8]. The basic idea of this theory is that two electrons, which are in the vicinity of the Fermi level, and with opposite momenta and spins, form a pair, the so-called Cooper pair, due to the interaction with phonons. At the critical temperature, Cooper pairs are formed and, at the same time, they condense to form the superconducting state.

During the sixties and seventies, it was found that other classes of materials,

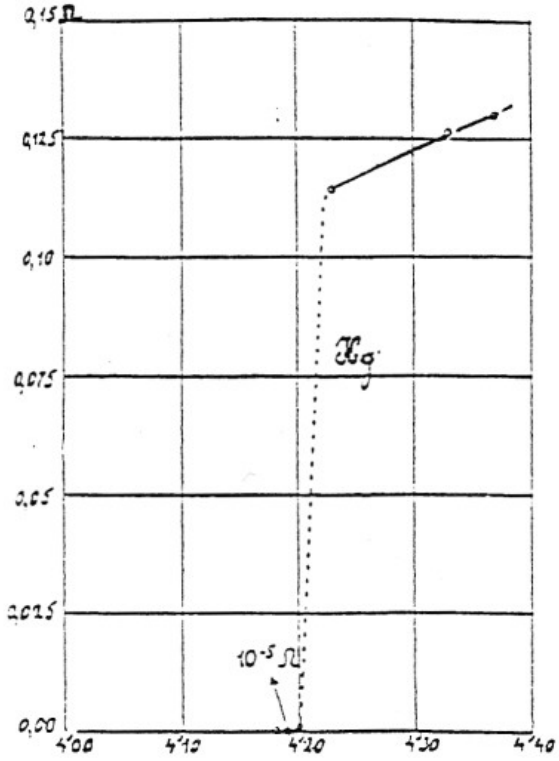

Figure 1.1: Resistivity of mercury at low temperatures.

as Bechgaard salts and heavy fermion materials, also exhibit the phenomenon of superconductivity. As the critical temperature is concerned, in this period, the highest value was about 23K, see Fig. 1.2, which was measured in Nb_3Ge.

High-temperature superconductors (HTSCs)

In 1986, a breakthrough discovery was made in the field of superconductivity. Alex Müller and Georg Bednorz, from the IBM research laboratory in Rüschlikon, Switzerland, discovered that the ceramic material $La_{2-x}Ba_xCuO_4$ (LBCO) becomes superconducting below a critical temperature of about 30K [9]. Their discovery was even more surprising, because contrarily to the previous known superconducting materials, which were metals, here the parent compound, La_2CuO_4 (LCO), is an antiferromagnetic insulator, and doping, which is introduced by re-

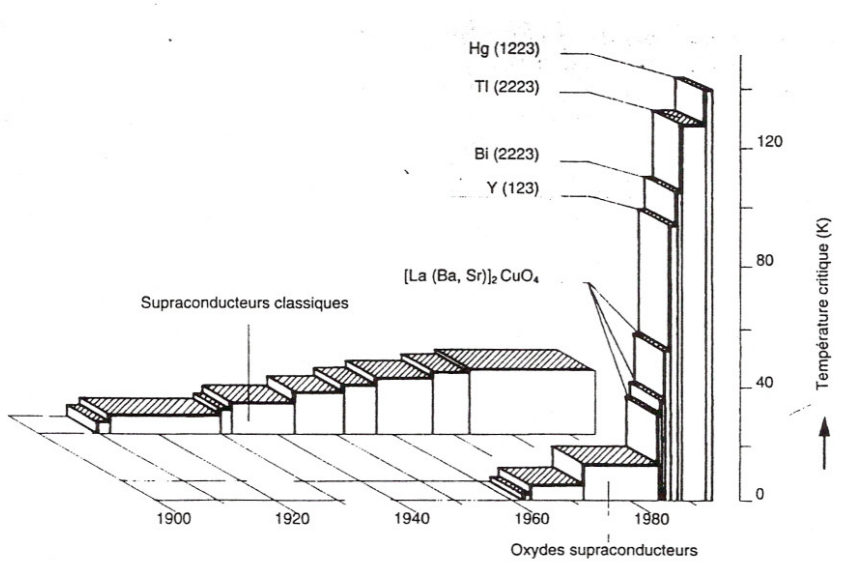

Figure 1.2: Evolution of the critical temperature for the transition to the superconducting state.

placing La with Ba, drives the system into a superconducting state. Shortly after, in 1987, Chu and Wu have found that by replacing lanthanum by yttrium, a new compound $YBa_2Cu_3O_{7-x}$ (YBCO) could be obtained. In this case, doping is realized by the excess of oxygen, and the critical temperature is much higher, $T_c \simeq 90K$. Since these discoveries, several materials exhibiting superconductivity at high-temperatures have been found. Their common feature is that they all consist of CuO_2 layers separated by a different buffer, called the "charge reservoir". Moreover, the number of CuO_2 layers in the unit cell seems to be related to the critical temperature. For instance, LBCO is a single-layer material with $T_c \simeq 30$K, YBCO consists of two CuO_2 layers and has $T_c \simeq 90$K, whereas the mercury based compound doped with thallium, which consists of three layers, has the highest critical temperature ever measured, $T_c \simeq 135$K [10]. In addition, the bismuth-based HTSC material, $Bi_2Sr_2Ca_{n-1}Cu_nO_{2n+4-\delta}$ (BiSCCO), where n is an integer, discovered in 1988, whose unit cell may consist of one, two or three CuO_2 planes, has the critical temperature increasing from 95K to 110K with the number of CuO_2 layers.

Although the LBCO compound has been the first HTSC material to be discovered, the most studied material in the three above-mentioned classes of HTSCs is $La_{2-x}Sr_xCuO_4$ (LSCO), which is obtained by replacing La^{3+} by Sr^{2+} ions. It

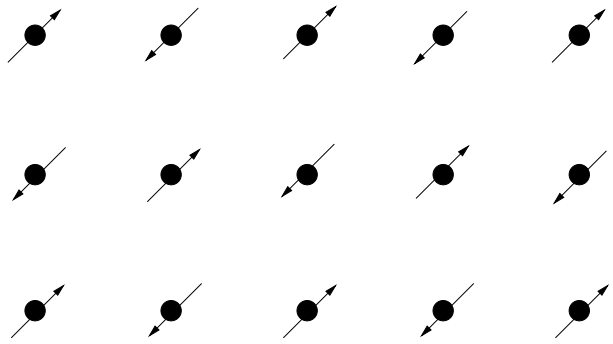

Figure 1.3: The AF (Néel) order of the effective copper spins below $T_N \simeq 325$K in the LCO compound.

has a simple structure which consists of single CuO_2 planes separated by insulating La(Sr)O buffers. In order to address the effect of the Sr dopant holes, it is inevitable, as a starting point, to thoroughly understand the physical properties of the undoped compound, LCO.

Chemical Structure of LCO

The electronic configurations of the atoms forming LCO are the following:

$$\begin{aligned} &\text{La} : [\text{Xe}](5d)(6s)^2 \\ &\text{Cu} : [\text{Ar}](3d)^{10}(4s) \\ &\text{O} : [\text{He}](2s)^2(2p)^4. \end{aligned}$$

Since the oxygen completes the p shell by accepting two electrons, its stable configuration is O^{2-}. Lanthanum becomes stable by losing three electrons, and thus its ionic state is La^{3+}. In order to ensure the charge neutrality of the compound, the ionic configuration of copper is Cu^{2+}. Consequently, the Cu atom loses the $4s$, and also one $3d$ electron, which creates an effective hole in the $3d$ shell. With such an electronic structure, one would naively expect that LCO has a half-filled conduction band, and thus is a good metal. However, LCO is an insulator, what shows the importance of the electron-electron correlations in this material. Because of these strong correlations, each effective hole is localized at a Cu site, giving rise to a completely filled the would-be conduction band. Therefore, LCO is a Mott insulator. Furthermore, the effective hole in the $3d$ orbital of the copper ion has mainly $d_{x^2-y^2}$ character and carries a spin $S = 1/2$, which is responsible for the magnetic properties of the compound. The single CuO_2 plane can be described, in a good approximation, as a two-dimensional square lattice formed by the coupled

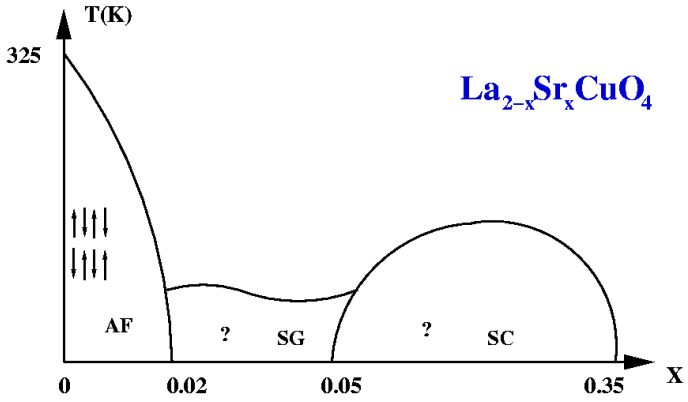

Figure 1.4: A sketch of the phase diagram (temperature versus Sr doping concentration) of the LSCO compound. At T=0 and $x \lesssim 0.02$ LSCO is in the AF state; for $0.02 \lesssim x \lesssim 0.05$ the compound is in the spin-glass (SG) phase. At the doping concentration $x \simeq 0.05$ a superconducting (SC) phase sets in, and persists up to $x \simeq 0.35$.

spins localized on the copper sites, Fig. 1.3. The interaction between the spins, mediated by oxygen ions, leads to their antiferromagnetic (AF) ordering below the critical temperature of $T_N \simeq 325K$. Above this critical temperature the spin ordering is short-ranged, and the spins are in the so-called paramagnetic phase characterized by a finite correlation length.

The Sr doping causes dramatic changes in the physical properties of the material. A sketch of the phase diagram (temperature versus doping concentration) of the LSCO compound is given in Fig. 1.4 (a more precise experimental phase diagram is shown in the next chapter, in Fig. 2.2). In this thesis, we concentrate on the magnetic properties of this compound in the undoped (Chapter 2) and lightly doped regimes (Chapters 3 and 4), before the material becomes a superconductor.

Models for HTSCs - Hubbard and $t-J$

The mechanism of high-temperature superconductivity is one of the most challenging unsolved problems in modern condensed matter theory. Several models have been proposed for describing this phenomenon, see Ref. [11, 12, 13] for a review on this issue. The usual starting point for describing the physics taking place in the CuO_2 planes of these compounds, which are believed to be responsible for the occurrence of the superconductivity, is the three-band Hubbard model. This model accounts for the hopping of the electrons localized on a $3d$ orbital of

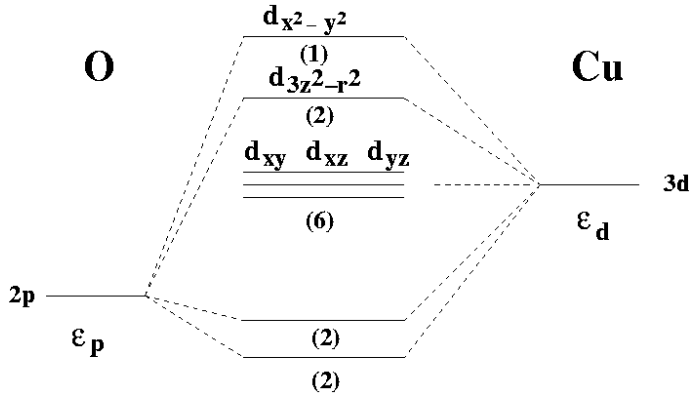

Figure 1.5: $3d$ orbital of Cu^{2+} ion and $2p_x$ and $2p_y$ orbitals of O^{2-} ions taken into account within the three-band Hubbard model (1.1). The numbers in parentheses denote the occupation of the different states in undoped compound.

the Cu^{2+} ion and the two O^{2-} orbitals, as well as the on-site Coulomb repulsion between them. The Hamiltonian of the model in the hole notation, i.e., with the ground state defined with all the orbitals in Fig. 1.5 occupied, reads

$$\begin{aligned} H_{3-band} &= -t_{pd}\sum_{\langle ij\rangle}(p_j^\dagger d_i + H.c.) - t_{pp}\sum_{\langle jj'\rangle}(p_j p_{j'} + H.c.) + \epsilon_d\sum_i n_i^d + \epsilon_p\sum_j n_j^p \\ &+ U_{dd}\sum_i n_{i\uparrow}^d n_{i\downarrow}^d + U_{pp}\sum_j n_{j\uparrow}^p n_{j\downarrow}^p + U_{dp}\sum_{\langle ij\rangle} n_i^d n_j^p. \end{aligned} \tag{1.1}$$

Here, p_j is a Fermi operator that annihilates the hole at the oxygen ion located at the site j, while d_i represents the annihilation operator for the hole at the copper ion i. The sum over $\langle ij\rangle$ refers to the nearest neighboring copper (i) and oxygen (j) sites. The hopping terms t_{pp} and t_{pd} represent the overlap of the corresponding orbitals, whereas the terms with the parameters ϵ_k and U_{kl} represent the energies of the orbitals and the on-site Coulomb repulsion, respectively. These parameters can be estimated from band-structure calculations [14], and their values in eV are given in the following table

$\epsilon_p - \epsilon_d$	t_{pd}	t_{pp}	U_d	U_p	U_{pd}
3.6	1.3	0.65	10.5	4	1.2

indicating that the physics taking place in the CuO_2 planes is described by the strong-coupling regime of the three-band Hubbard model (1.1).

In the limit of a strong on-site repulsion, and with one particle per site (half-filling), the three-band Hubbard model reduces to the two-dimensional Heisenberg

model,

$$H_H = J \sum_{\langle ij \rangle} \mathbf{S}_i \cdot \mathbf{S}_j, \tag{1.2}$$

where $\mathbf{S}_i$ is the spin-1/2 operator at the site i, $J > 0$ is the antiferromagnetic coupling constant, and the sum is over nearest-neighboring sites. The two-dimensional Heisenberg model (1.2) is commonly accepted for describing the physics taking place in the CuO_2 planes of the parent compounds of the HTSCs. The magnetic properties of La_2CuO_4, for instance, are effectively described in terms of the one-half spins localized on the Cu^{2+} ions, which form a square lattice within each CuO_2 layer, and interact antiferromagnetically with the coupling constant $J \simeq 1200$K, as will be discussed in more detail in Chapter 2. In addition, the spins exhibit 3D antiferromagnetic (Néel) order up to a temperature of $T_N \simeq 325$K, due to a weak coupling between the adjacent CuO_2 layers. Indeed, Chakravarty *et al.* [15] used the $O(3)$ nonlinear sigma model, which is a continuum theory describing the low-energy dynamics of the fluctuations in the Heisenberg model, for studying the problem. The correlation length and the Néel temperature obtained within this approach fitted extremely well the experiments [16].

The three-band Hubbard model is very complicated, especially when doping is taken into consideration, and it is thus desirable to reduce it to a simpler model. This important step has been achieved by Zhang and Rice [17], who have mapped the three-band Hubbard into the $t-J$ model, using the following arguments. A single hole introduced, for instance, by Sr doping, is mainly localized on the oxygen orbital, and forms a singlet on a CuO_4 plaquette with the hole localized on the $3d$ copper orbital. Therefore, the doping effectively introduces spinless holes into the lattice formed by one-half spins localized on the Cu^{2+} ions. These holes move through the lattice, and their motion frustrates the underlying antiferromagnetic background, eventually leading to a complete destruction of the Néel ground state. The Hamiltonian describing the dynamics of the holes is then given by the so-called $t-J$ model,

$$H_{t-J} = J \sum_{\langle ij \rangle} \mathbf{S}_i \cdot \mathbf{S}_j + \sum_{\langle ij \rangle, \sigma} (t_{ij} c^\dagger_{i\sigma} c_{j\sigma} + H.c.), \tag{1.3}$$

where $c^\dagger_{i\sigma}$ is a Fermi operator that creates an electron with spin σ at the site i, constrained to no double occupancy, $\mathbf{S}_i = (1/2) c_{i\sigma} \boldsymbol{\sigma}_{\sigma\sigma'} c_{i\sigma'}$ is the spin-1/2 operator at the site i, with $\boldsymbol{\sigma}$ being the Pauli matrices, and t_{ij} is the hopping between sites i and j. In the limit of large on-site Coulomb repulsion, the three-band Hubbard model then reduces to the $t-J$ model.

Another extensively studied model, besides the three-band Hubbard and the $t-J$ models, is the one-band Hubbard model

$$H_{1-band} = -t \sum_{\langle ij \rangle, \sigma} (c^\dagger_{i\sigma} c_{j\sigma} + c^\dagger_{j\sigma} c_{i\sigma}) + U \sum_i \left(n_{i\uparrow} - \frac{1}{2} \right) \left(n_{i\downarrow} - \frac{1}{2} \right), \tag{1.4}$$

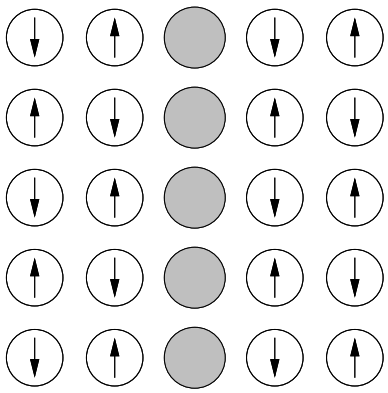

Figure 1.6: A sketch of vertical stripe state. Notice that the staggered magnetization changes phase by π across the stripe, which gives rise to the charge ordering wave vector twice the magnetic one.

where U is the on-site Coulomb repulsion and t represents the hopping. Here, the on-site Coulomb repulsion effectively represents the three bands, present in the HTSC materials, by taking into account the energy gap between the copper ($3d$) orbital and the oxygen ($2p$) orbitals.

Theoretical and experimental results: stripes versus phase separation

Although the complex behavior of the three-dimensional layered HTSC materials has been extremely simplified by adopting a description based on the Hubbard or the $t-J$ models, even within those simplified models, the nature of the ground-state of the system is a controversial issue. The usual starting point is to assume that the dopant holes introduced in the system are homogeneously distributed. However, mean-field studies performed within the Hubbard model proposed that the holes may form one-dimensional "rivers" of charge [18], the so-called "stripe" state, thus breaking the paradigm of homogeneously distributed holes in the ground-state of cuprates. For a review on stripe states in strongly correlated systems, see Ref. [19]. An important characteristic of the stripes is that they are believed to act as antiphase domain walls for the underlying antiferromagnetic order, i.e., across a stripe the staggered magnetization changes phase by π; an illustration of the vertical stripe order is shown in Fig. 1.6. This leads to essential changes in the magnetic structure, which can be detected by neutron scattering experiments. Indeed, in the antiferromagnetic phase, the magnetic periodicity is $(2a, 2a)$, where a is the lattice constant, and neutron scattering experiments observe then a peak at $(\pi/a, \pi/a)$, which is called the "commensurate"

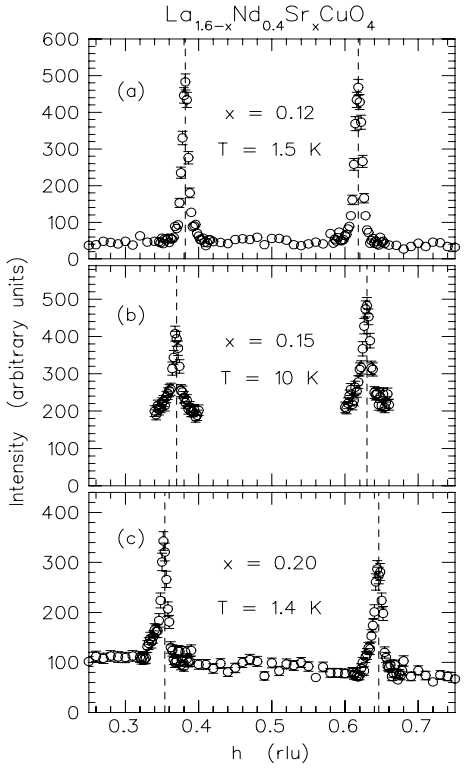

Figure 1.7: Scans of elastic neutron scattering peaks in $La_{1.6-x}Nd_{0.4}Sr_xCuO_4$ along the vector $\mathbf{Q} = (h, \frac{1}{2}, 0)$, with $h = \frac{1}{2} \pm \epsilon$, as reported in Ref. [20]. Note that the units are such that $\frac{2\pi}{a} = 1$, with a being the lattice constant. In these units, $\epsilon = \frac{a}{2L}$, where L is the stripe separation.

peak. In the presence of stripes separated by a distance L, which act as antiphase domain walls for the underlying antiferromagnetic order, the commensurate peak should split into two incommensurate peaks at $(\pi/a \pm \delta, \pi/a)$, with $\delta = \pi/L$. The stripe state should be characterized by an incommensurability not only in the magnetic, but also in the charge sector, where the corresponding ordering wave vector should have a periodicity which is twice the magnetic one, see Fig. 1.6. In fact, both the magnetic and the charge periodicity have been measured by neutron and Bragg scattering experiments, respectively. The experimental observation of incommensurate magnetic peaks in elastic neutron scattering by Tranquada *et al.* [21] have revealed that the incommensurate stripe state may indeed be realized in cuprates. In fact, they observed four static incommensurate magnetic peaks in

Nd-doped LSCO, $La_{2-x-y}Nd_ySr_xCuO_4$, for $x = 0.12$, 0.15, and 0.20, and $y = 0.4$, see Fig. 1.7, at the positions $(\pi/a \pm \delta, \pi/a)$ and $(\pi/a, \pi/a \pm \delta)$. In addition, the magnetic peaks are accompanied by Bragg peaks at the points $(\pm 2\delta, 0)$ and $(0, \pm 2\delta)$, suggesting that the charges form domain walls, across which the phase of the staggered magnetization changes by π. The co-doping of LSCO with Nd appears to be crucial for stabilizing the stripe state, due to a structural transition induced in the material by this rare-earth dopant. On the other hand, the co-doping usually reduces the critical temperature of the superconducting transition [21, 22], which indicates that stripes and superconductivity may be competing orders in cuprates. Although in the rare-earth co-doped compound static stripe order could be detected by *elastic* neutron scattering experiments, the observation of the incommensurate peaks in *inelastic* neutron scattering in superconducting LSCO samples at the same wave vectors as the ones in Nd-doped samples, put the stripe picture on a more solid footing [23].

The previously discussed theoretical and experimental findings stimulated further investigations of the stripe ground state within the Hubbard and $t-J$ models, mostly by employing different numerical techniques, such as density matrix renormalization group (DMRG) [24, 25, 26], quantum Monte Carlo [27, 28, 29, 30], and exact diagonalization [11]. However, the question whether the stripe phase is the ground state of these models is highly nontrivial. In fact, numerical calculations performed within the $t - J$ model by Emery *et al.* [31] have shown that, close to half-filling, the holes have a tendency to phase separate into hole-rich and hole-poor regions, instead of forming stripes, see Fig. 1.8. Their results can be understood on physical grounds, in the limit $t \to 0$ (close to half-filling). Indeed, when the kinetic energy is negligible, the energy of the system is minimized when the number of broken antiferromagnetic bonds is minimal, which is achieved by the phase separation. Naturally, this simple picture overestimates the role of the magnetic energy, and as such is only valid when $J \gg t$. When a finite kinetic energy of holes, corresponding to a finite overlap between the hole wave functions, is introduced, this simple picture seems to break down. Therefore, the question is whether the phase separation takes place only in the limit $J \gg t$ or it also occurs for a finite ratio J/t. On the other hand, DMRG calculations performed in the $t - J$ and the $t - J_z$ (Ising $t - J$) models [24, 25, 26, 32] indicate that the stripe ground state does occur in these models. These calculations also support the idea that the stripes compete with superconductivity, since the stripe state, in these calculations, has a vanishing density at the Fermi level, and it is thus insulating.

Problems with the conventional models

As we discussed above, the issue of the ground state in the Hubbard and $t - J$ models is controversial, and it is still an open problem. A more fundamental issue, however, concerns the sufficiency of these models for describing HTSCs. For instance, Hubbard and $t - J$ models take into account only the short-ranged

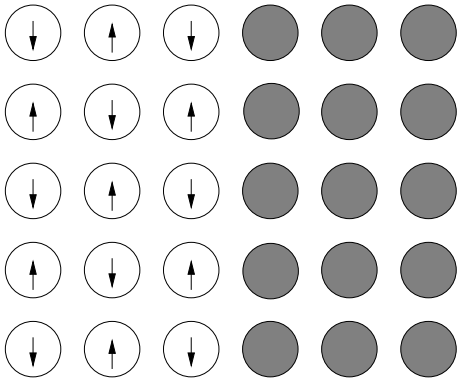

Figure 1.8: Phase separation of holes into hole-rich and hole-poor regions caused by a predominant AF interaction, $J \gg t$.

on-site interaction between holes, but the long-range Coulomb interaction, that may also play an important role in determining the ground state properties, is completely neglected. Furthermore, the next-nearest neighbor hopping terms are not included within these models. In fact, numerical calculations show that these terms can play a significant role in determining the ground state. For instance, when only the next-nearest neighbor hopping term, t', is introduced in the $t-J$ model, different many-body states, such as d-wave paired holes and spin-polarons, may be realized in the ground state of the model [24, 25, 26, 33]. In addition, when further nearest-neighbor hopping processes are included, a spin spiral state can occur in the ground state, as shown by Sushkov and Kotov [34]. In real materials, different anisotropies also play an important role in determining their physical properties. As we already mentioned, Nd co-doping of LSCO induces a structural transition in the material, which may help to stabilize the stripe state. Indeed, mean-field calculations within the anisotropic $t-J$ model have shown that a very small anisotropy in the hopping parameter, associated with the structural transition induced by co-doping, is enough to stabilize the stripe ground state [35].

Concerning the undoped compounds, which are commonly accepted to be described by the isotropic Heisenberg model, there are additional anisotropies, introduced by the spin-orbit coupling and the crystal structure, for instance, which are usually neglected in the theoretical studies of these materials. However, recent magnetic susceptibility measurements performed by Lavrov *et al.* [36] revealed that the magnetic susceptibility response in La_2CuO_4, as well as in LSCO with $x = 1\%$, 2%, 3%, and $x = 4\%$, is completely *anisotropic* up to temperatures as high as 400K, and exhibits a zero-temperature hierarchy, which is not characteristic for an easy-axis antiferromagnet. This raised a question about the role of these

anisotropies in describing the magnetic properties of this compound.

The role of the Dzyaloshinskii-Moriya and the pseudodipolar anisotropic interactions in La_2CuO_4 (Chapter 2)

In Chapter 2 of this thesis, we consider this problem starting with the complete microscopic spin Hamiltonian, which, besides the ordinary Heisenberg interaction, includes the Dzyaloshinskii-Moriya (DM) and the pseudodipolar (XY) anisotropic spin interactions. The mapping of this model into the corresponding continuum theory reveals that the effect of these anisotropies is to introduce gaps for the spin excitations, which are responsible for the magnetic ground-state properties of the compound, in particular, the staggered magnetization being oriented along the b orthorhombic axis and the weak ferromagnetic moment perpendicular to the CuO_2 planes (along the c orthorhombic axis). We then consider the effect of a magnetic field applied to the system. The presence of the DM interaction leads to an unexpected linear coupling of the magnetic field to the staggered magnetization. We then calculate the magnetic susceptibility and discuss our results in connection with recent measurements.

Spin-glass phase of $La_{2-x}Sr_xCuO_4$: problems with the stripe and the spiral pictures

When doping is introduced, the antiferromagnetic order is rapidly destroyed. For instance, in LSCO a Sr doping of only 2% is enough to completely suppress the long-range antiferromagnetic order in the ground state. Beyond this doping value, i.e., for $2\% < x < 5\%$, a spin-glass phase sets in, where the magnetic order is only short-ranged. In addition, two diagonal incommensurate elastic peaks have been observed in this phase [37, 38, 39, 40], and their interpretation in terms of stripes appeared to be rather natural, given that the doping dependence of the magnetic incommensurability in the spin-glass phase follows the same behavior as in the superconducting regime, see Fig. 1.9. However, the associated charge order has never been observed in the spin-glass phase, which raises the question of the validity of the stripe picture at such small doping concentration. Moreover, in the low doping regime, the effect of disorder is expected to dominate [41], and, as a result, to destabilize the stripes. Although the stripe scenario in the spin-glass phase cannot be completely excluded, it is quite improbable, and, consequently, several pictures based on the formation of an incommensurate magnetic ground state, with the charge being randomly distributed, have been proposed.

Klee and Muramatsu considered the $SO(3)$ nonlinear sigma model [42], which is obtained in the long-wavelength limit of the spin-fermion model, assuming that an incommensurate spin spiral is formed in the magnetic ground state of the system, such that the spins rotate in the CuO_2 planes. Within their approach, the spiral state becomes stable due to the presence of the dopants, but it is not

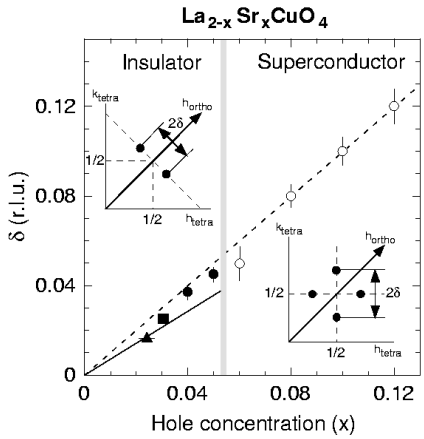

Figure 1.9: Doping dependence of the incommensurability in the spin-glass and the superconducting phase of $La_{2-x}Sr_xCuO_4$ as reported in Ref. [39]. Observe the rotation of 45° in the direction of the incommensurate peaks across the transition from the spin-glass to the superconducting phase.

clear how exactly the incommensurability depends on the doping concentration. Hasselmann *et al.* [43, 44] considered the spiral state within the $SO(3)$ nonlinear sigma model, which arises from the Heisenberg model solely. The effect of doping is introduced via an effective dipole field that minimally couples to the background magnetization current. Assuming that a fraction of the dipoles orders, they found that it is possible to stabilize the spiral ground state. Moreover, they obtained the linear doping dependence of the incommensurability under the condition that the ordered fraction of dipoles scales linearly with the doping concentration, what is a rather plausible assumption. Although this model can describe the linear scaling of the incommensurability with doping, the picture of spins spiralling within the CuO_2 planes is inconsistent with recent magnetic susceptibility measurements [36], which indicate that the total spin remains confined to the *bc* plane, as in the undoped compound. Similar problem occurs in the studies of Sushkov and Kotov [34, 45], based on an extended $t - J$ model, which includes the further nearest-neighbor hopping terms. In addition, within the latter model the Néel ground state is unstable already at an infinitesimal doping, which is in clear contrast with the observed threshold of $x = 2\%$.

A helicoidal phase as a possible solution of the problem (Chapter 3)

In order to resolve these two problems, in Chapter 3, we consider the role of the DM and XY interactions when the doping is included via an effective dipole field, which couples to the background magnetization current. We analyze the stability of the canted Néel state in the presence of the dopants and show that the robustness of this state stems from the DM and XY anisotropies. The coupling of the magnetization current to the effective dipoles causes a reduction of the spin gaps, which we calculated and showed to be consistent with recent Raman scattering experiments [46]. For higher doping, $2\% < x < 5\%$, we find that the ground state is unstable towards a helicoidal magnetic phase, in which the staggered part of the spin has a small component that rotates in the plane perpendicular to the b orthorhombic axis, and a dominant contribution which is along the b-axis, thus giving rise to a total staggered magnetization along the same axis. As a result, the weak ferromagnetic moment is perpendicular to the CuO_2 planes, and the total spin is confined to the bc-plane, in agreement with magnetic susceptibility experiments [36]. The new helicoidal ground state gives rise to the incommensurability observed in the spin-glass phase of LSCO. The incommensurate wave vector is related to the anisotropies and doping in a way which allows us to explain not only the linear doping dependence of the incommensurability observed by neutron scattering experiments, but also its deviation from linearity at the onset of the spin-glass phase. In addition, the behavior of the incommensurability in the presence of a magnetic field perpendicular to the CuO_2 planes is also discussed and a "smoking-gun" experiment which would allow to decide between the helicoidal and diagonal stripe scenarios for LSCO is proposed in Chapter 3.

Transport properties in lightly doped $La_{2-x}Sr_xCuO_4$ (Chapter 4)

Recently, transport properties have been investigated in high-quality, detwinned LSCO samples, and an anisotropy in the dc resistivity has been observed along the two orthorhombic axes in the CuO_2 plane [47]. The results of these experiments have been interpreted as a signature of stripe formation, since such an anisotropy is expected to occur within the stripe picture. However, as we discuss in Chapter 4, the anisotropy in the dc resistivity can also be explained within the helicoidal model in which the incommensurability appears in the spin sector only. Actually, for this analysis, as discussed in Chapter 4 in more detail, it is not important whether the spins rotate in the CuO_2 plane, as in the spiral ground state, or out of the plane, which is the case in the helicoidal state. In this chapter, we study the formation and the dynamics of topological defects associated with the spiral or helicoidal ground state within the $SO(3)$ nonlinear sigma model. We consider two types of topological defects, single vortices and vortex-antivortex pairs, and quantize the corresponding solutions by generalizing the semiclassical approach to a non-Abelian field theory. We analyze the dynamics of these defects, and show,

using the collective coordinate method, that the defect is coupled to a bath of harmonic oscillators, representing the magnetic excitations of the system. The resulting effective action for the defect indicates that its motion is damped due to the scattering by the magnons. We discuss the temperature dependence of the inverse mobility for both single-vortices and vortex-antivortex pairs. Actually, the model is quite general, and can be used to describe the dynamics of topological defects in other frustrated Heisenberg spin system with a noncollinear magnetic ground state, such as geometrically frustrated antiferromagnets on a triangular lattice and helimagnets, in which a competition between nearest-neighbor and further-neighbor interactions introduces the frustration in the system. Finally, at the end of Chapter 4, motivated by recent experiments by Ando *et al.* [47], we consider an application of the model to describe the transport properties in the spin-glass phase of LSCO, assuming that the charge carriers are attached to the vortices, and compare the calculated dc resistivity with experiments. We find a good agreement between our results and the experimental data by Ando *et al.* [47].

Chapter 2

Magnetic Properties of La_2CuO_4

This chapter is based on the following publications: M. B. Silva Neto, L. Benfatto, V. Juricic, and C. Morais Smith, Phys. Rev. B **73**, 045132 (2006) and L. Benfatto, M. B. Silva Neto, V. Juricic, and C. Morais Smith, Physica B (2006) (to be published).

The La_2Cu0_4 (LCO) compound is a Mott-Hubbard antiferromagnetic insulator with the Néel temperature of $T_N \simeq 325$K. It consists of weakly coupled two-dimensional CuO_2 layers, separated by the LaO buffers, see Fig. 2.1. By replacing La^{3+} with Sr^{2+} ions, holes are introduced into the CuO_2 layers. The properties of the doped compound, $La_{2-x}Sr_xCuO_4$ (LSCO), dramatically change, and it eventually becomes a superconductor when Sr concentration is $x_{SC} \simeq 0.055$, see Fig. 2.2. The CuO_2 layers are a common feature for the materials exhibiting high-temperature superconductivity. Actually, the physics taking place in the CuO_2 layers is widely believed to play a key role in the mechanism of superconductivity in these materials. Moreover, the study of the evolution of transport and magnetic properties with doping, starting with the undoped compound, might give an indication about the pairing mechanism in the superconducting state. It is well known that the antiferromagnetic correlations persist well after the Néel order has been destroyed and influence the dynamics of the holes introduced in the CuO_2 layers upon doping [48]. Thus, in order to address the dynamics of the dopant holes, it is necessary to understand first the magnetic properties of the undoped compound.

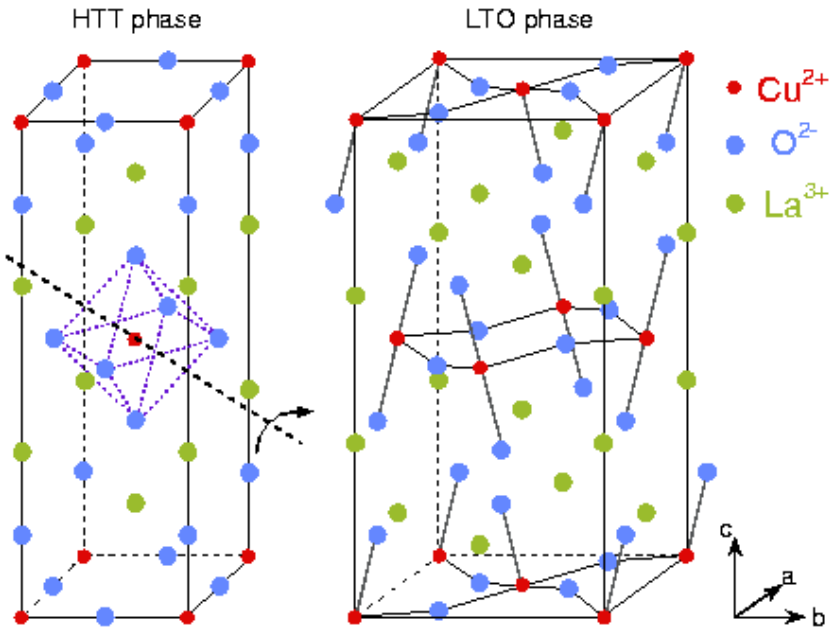

Figure 2.1: The crystal structure of La_2CuO_4 from Ref. [46]. Left panel: high-temperature tetragonal (HTT) phase. Right panel: low-temperature orthorhombic (LTO) phase occurring below $T_{T-O} \simeq 530$K.

2.1 The Microscopic Model

The interaction between the copper spins, mediated via the oxygen atoms (superexchange mechanism), is described by the Heisenberg Hamiltonian

$$H_H = J \sum_{\langle ij \rangle} \mathbf{S}_i \cdot \mathbf{S}_j. \tag{2.1}$$

Here, $\mathbf{S}_i$ is a spin-$\frac{1}{2}$ operator on a site i, the sum is over nearest-neighboring sites, and J is the antiferromagnetic (superexchange) coupling constant, which is $J \sim 125$meV in the LCO system. An approach based on the above *isotropic* Hamiltonian happened to be quite successful in describing the low-energy properties of the compound. In particular, the temperature dependence of the correlation length in the paramagnetic phase, i.e., after the long-range Néel order is destroyed, has been derived [15] and showed an excellent agreement with experiments [49]. As we will discuss in this thesis, nontrivial lattice effects, as well as the spin-orbit coupling, introduce anisotropic corrections to the above spin Hamiltonian, thus yielding a *completely* anisotropic behavior, in agreement with more recent

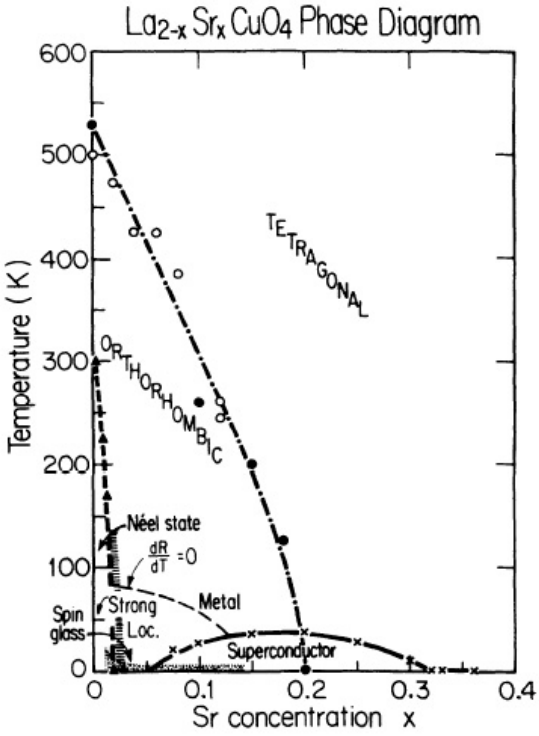

Figure 2.2: Phase diagram of $La_{2-x}Sr_xCuO_4$ from Ref. [16].

experiments [36].

The crystal structure of LCO is shown in Fig. 2.1. In the high-temperature tetragonal (HTT) phase the CuO_2 planes are flat. At the temperature $T_{T-O} \simeq$ 530K a structural transition to the low-temperature orthorhombic (LTO) phase occurs, see Fig. 2.2, which is caused by a staggered tilt of the CuO_6 octahedra, as shown in Fig. 2.1. The tilting angle is about 4°, and it is uniform in the plane determined by the tilting and the c-axis. As a consequence, two oxygen atoms in the base of the CuO_6 octahedron are below, whereas the two other oxygen atoms are above the plane made by Cu atoms, as shown in the right panel of Fig. 2.1. The vectors of the orthorhombic elementary cell are represented in the bottom of Fig. 2.1; the tetragonal ones are obtained from the orthorhombic vectors by a rotation of 45° in the CuO_2 plane. The lattice constants in the LTO phase are $a = 5.354$Å, $b = 5.401$Å, and $c = 13.153$Å.

Although the orthorhombicity resulting from the staggered tilting of the CuO_6

octahedra is small, $2(b-a)/(b+a) \simeq 0.8\%$, it is responsible for the presence of the anisotropic Dzyaloshinskii-Moriya (DM) and pseudodipolar (XY) interactions in the material, once the spin-orbit coupling is considered. These anisotropies, in turn, determine the b orthorhombic axis to be the easy-axis for the staggered magnetization [50], cause a weak ferromagnetic moment along the c-axis [51, 52], as well as a complete anisotropy of the magnetic susceptibilities along the LTO crystallographic axes [36]. The antisymmetric DM interaction results from the tilting of the CuO_6 octahedra, as well as the spin-orbit coupling on the Cu ion. Starting with a Hubbard-like Hamiltonian that incorporates the spin-orbit interaction, it may be shown (see App. A for details) that the DM interaction between the spins in the CuO_2 plane has the following form [53]

$$H_{DM} = \sum_{\langle ij \rangle} \mathbf{D}_{ij} \cdot (\mathbf{S}_i \times \mathbf{S}_j), \tag{2.2}$$

where the DM vector $\mathbf{D}_{ij}$ is defined on the Cu-O bond, and its pattern, depicted in Fig. 2.3, is a direct consequence of the tilting structure of the CuO_6 octahedra and the symmetry of the LCO crystal. In what follows, we adopt the LTO coordinate system shown in Fig. 2.3 for both lattice and spin degrees of freedom. Thus, the DM vectors on the ij and ik bonds are

$$\mathbf{D}_{ij} = (-d, d, 0)/\sqrt{2}, \qquad \mathbf{D}_{ik} = (d, d, 0)/\sqrt{2}, \tag{2.3}$$

respectively, with $d \sim 10^{-2}J$.

The pseudodipolar interaction arises from the superexchange processes, as shown in App. A. Another important contribution to this interaction, as pointed out by Shekhtman *et al.* in Ref. [54], results from the direct-exchange processes mediated by the spin-orbit interaction. For instance, the spin on the $3d_{x^2-y^2}$ orbital of the Cu ion situated at the site i can go to the $3d_{xy}$ orbital of the same ion using the spin-orbit coupling; then, from the $3d_{xy}$ orbital it can move further to the $3d_{x^2-y^2}$ orbital of the neighboring Cu ion by the direct-exchange process, and return to the original state via the $3d_{xy}$ orbital at the site i. This type of pseudodipolar interaction does not depend on the tilting angle, but only on the spin-orbit and the direct-exchange coupling constants. Taking into account both the superexchange and the direct exchange contributions, the pseudodipolar interaction reads

$$H_{XY} = \sum_{\langle ij \rangle} \mathbf{S}_i \cdot \overleftrightarrow{\Gamma}_{ij} \cdot \mathbf{S}_j, \tag{2.4}$$

with the matrix Γ defined on the bonds ij and ik as follows

$$\overleftrightarrow{\Gamma}_{ij} = \begin{pmatrix} \Gamma_1 & \Gamma_2 & 0 \\ \Gamma_2 & \Gamma_1 & 0 \\ 0 & 0 & \Gamma_3 \end{pmatrix}, \qquad \overleftrightarrow{\Gamma}_{ik} = \begin{pmatrix} \Gamma_1 & -\Gamma_2 & 0 \\ -\Gamma_2 & \Gamma_1 & 0 \\ 0 & 0 & \Gamma_3 \end{pmatrix}, \tag{2.5}$$

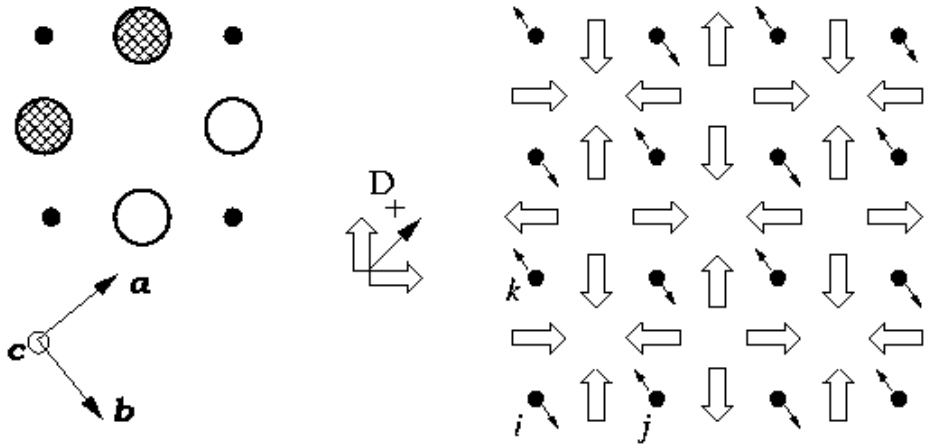

Figure 2.3: Left panel: the hatched circles represent the O^{2-} ions tilted above the CuO_2 plane; the empty ones are tilted below it; small black circles are Cu^{2+} ions; *bac* orthorhombic coordinate system. Right panel: Schematic arrangement of the staggered magnetization (small black arrows) and DM vectors (open arrows). Center: continuum definition of $\mathbf{D}_+$.

where $\Gamma_{1,2,3}$ are of order $10^{-4}J$, and $\Gamma_1 > \Gamma_3$. Let us point out here that the pseudodipolar interaction cannot be neglected in comparison with the DM interaction, even though the parameters Γ in Eq. (2.4) are two orders of magnitude smaller than the one determining the strength of the DM interaction, see Eq. (2.3). Indeed, the contributions of the DM and XY anisotropies to the magnetic ground state energy are of the order d^2/J and Γ, respectively, and therefore they both have to be included in the spin Hamiltonian [54, 55]. For describing the magnetic properties of the single CuO_2 layer we thus adopt a Hamiltonian that incorporates the Heisenberg Hamiltonian, Eq. (2.1), together with the DM and XY Hamiltonians, given by Eqs. (2.3) and (2.4),

$$H_S = J \sum_{\langle ij \rangle} \mathbf{S}_i \cdot \mathbf{S}_j + \sum_{\langle ij \rangle} \mathbf{D}_{ij} \cdot (\mathbf{S}_i \times \mathbf{S}_j) + \sum_{\langle ij \rangle} \mathbf{S}_i \cdot \overleftrightarrow{\Gamma}_{ij} \cdot \mathbf{S}_j. \tag{2.6}$$

In the following section, we derive a generalized nonlinear sigma model, which describes the long-wavelength properties of the microscopic spin Hamiltonian with the anisotropic DM and XY interactions, given by Eq. (2.6). In addition, we discuss the features arising from the presence of these anisotropies, with an emphasis on the completely anisotropic magnetic susceptibility.

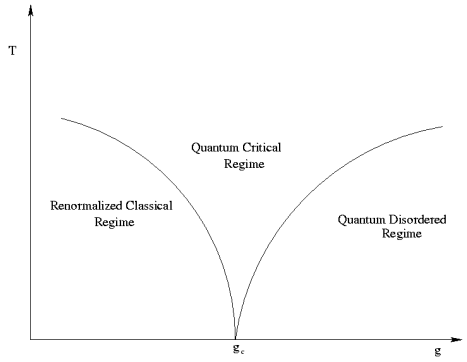

Figure 2.4: Phase diagram of the two-dimensional quantum nonlinear sigma model.

2.2 Generalized nonlinear sigma model

The usual starting point for describing the magnetic properties of the two-dimensional CuO_2 layers is the isotropic Heisenberg Hamiltonian (2.1). The quantum nonlinear sigma (QNLσ) model [56], which is the long-wavelength theory corresponding to the Hamiltonian (2.1) defined on the two-dimensional square-lattice, has been shown to correctly describe the magnetic properties of the LCO compound at high-temperatures, after the long-range antiferromagnetic order is destroyed [15, 57]. The QNLσ model is defined by the following Euclidean action ($\beta \equiv 1/T$, with T denoting the temperature, and we set $\hbar = 1$ and $k_B = 1$)

$$S_{QNL\sigma} = \frac{1}{2gc} \int_0^\beta d\tau \int d^2\mathbf{x} \{(\partial_\tau \mathbf{n})^2 + c^2 (\nabla \mathbf{n})^2\}, \tag{2.7}$$

where $\mathbf{n} \equiv \mathbf{n}(\tau, \mathbf{x})$ is the local staggered magnetization density, which obeys the local fixed-length constraint $\mathbf{n}^2 = 1$. Here, the coupling constant g is related to the spin-wave velocity, c, and the renormalized spin stiffness $\rho_s = c(1/Ng - \Lambda/4\pi)$, with Λ being the momentum cutoff, and $N = 3$ is the number of spin components [15, 57]. The phase diagram of the model at $T = 0$ consists of two regions separated by the quantum critical point at $g_c \sim 4\pi/\Lambda$. For $g < g_c$ the ground state is the antiferromagnetic one, which is $U(1)$ invariant, whereas in the region $g > g_c$ the full rotational symmetry of the ground state is restored, and the spins are in the so-called spin-liquid state. At finite temperatures, there are three regions in the phase diagram, as sketched in Fig. 2.4. Above the quantum critical point, in the quantum critical regime, the physics is controlled by the scale set only by the temperature. In the quantum disordered phase, separated by a crossover line from the quantum critical phase, spins have short-range correlations, with a correlation length that becomes temperature independent as $T \to 0$. Finally, the renormalized classical regime, which originates from the long-range Néel state at $T = 0$ when thermal

fluctuations are included, is characterized by a finite correlation length, which exponentially diverges as the system approaches zero temperature. It is widely believed that the physics of the Heisenberg model, which, in the large-S limit, maps into the QNLσ model (2.7), is described by the renormalized classical regime, with ρ_s and c taken as phenomenological parameters, fixed either by experiments or by numerical simulations. Indeed, the temperature dependence of the in-plane correlation length obtained from the continuum model (2.7) [15]

$$\frac{\xi_{2D}}{a} = C_\xi \exp\left(\frac{2\pi\rho_s}{T}\right)\left[1 + \mathcal{O}\left(\frac{T}{2\pi\rho_s}\right)\right], \tag{2.8}$$

with $C_\xi \simeq 0.5$, agrees extremely well with the experiments. Moreover, the $3D$ Néel transition temperature can be estimated from the same theory [15], if one takes into account the antiferromagnetic coupling between the neighboring CuO_2 layers, $J_\perp$, which is of the order $J_\perp/J \sim 10^{-5}$. Such a small perpendicular coupling has a negligible influence on the values of the parameters of the model, as well as on the in-plane magnetic correlations above T_N, but it drives the Néel temperature to a finite value, due to a large in-plane correlation length, $\xi_{2D} \sim 200a$, in the vicinity of the transition. At the mean-field level, the Néel temperature is determined by the interplay of the magnetic and the thermal energies

$$T_N \approx \mu_s^2 \left[\frac{\xi_{2D}(T_N)}{a}\right]^2 J_\perp, \tag{2.9}$$

where $\mu_s \simeq 0.5$ is the staggered magnetic moment in units of $g_S\mu_B$, with g_S being the gyromagnetic ratio of the electron and μ_B is the Bohr magneton. These parameters, when substituted in the above formula, yield a value for the Néel temperature of few hundred Kelvin, in agreement with experimentally measured $T_N \simeq 325$K.

Although the isotropic NLσ model is able to capture the magnetic properties of the LCO system in the paramagnetic phase, it is not sufficient for describing the compound at lower temperatures. In fact, at temperatures such that the anisotropic DM and XY interactions become important, the NLσ model needs to be modified, in a way to include these anisotropies. Recent measurements of the magnetic susceptibilities in the *detwinned*, i.e., macroscopically orthorhombic, LCO crystal along the three crystallographic axes by Lavrov *et al.* [36] indeed suggest that the magnetic state of LCO is different from a simple two-dimensional Heisenberg antiferromagnet, indicating that these anisotropies may play an important role in the material. Their experimental findings are shown in Fig. 2.5. As the susceptibility along the c-axis, χ_c, is concerned, we observe a sharp peak at T_N, which can be attributed to the ferromagnetic ordering of the small moments in adjacent CuO_2 layers, staggered below T_N due to the antiferromagnetic coupling between the neighboring layers. Indeed, such a behavior of the susceptibility χ_c had been previously observed, and a mean-field Ginzburg-Landau theory fitted

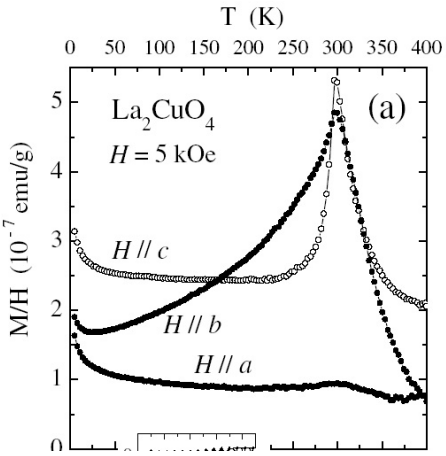

Figure 2.5: Magnetic susceptibility of detwinned single crystals of LCO measured in a magnetic field applied along one of the orthorhombic crystal axes (from Ref. [36]).

the data very well [52]. The surprising result of the experiments in Ref. [36] was that the in-plane susceptibilities, χ_a and χ_b, are anisotropic up to temperatures $T \sim 400$K, a feature that cannot be captured within the isotropic QNLσ model (2.7). Moreover, the zero-temperature hierarchy of the susceptibilities is not the one expected in a conventional easy-axis antiferromagnet, where the susceptibility along the easy-axis is the smallest one. In the LCO compound, the easy-axis is the b orthorhombic axis, and the smallest susceptibility is along the a-axis. In order to explain these unusual properties, we derive a generalized nonlinear sigma model starting with the microscopic Hamiltonian (2.6), which incorporates the anisotropic DM and XY interactions. We calculate the magnetic susceptibilities, and show that the above discussed features are captured qualitatively already at the mean-field level within this new theory.

2.2.1 Derivation of the generalized nonlinear sigma model

In this subsection, we derive the long-wavelength theory for the microscopic spin Hamiltonian (2.6). In order to achieve this goal, we will use the coherent state representation, $|\mathbf{N}\rangle$, for the spin operator $\hat{\mathbf{S}}$, which lie on a unit sphere, since $\mathbf{N}^2 = 1$, and thus span an infinitely dimensional Hilbert space. These states are convenient for constructing the path-integral representation of the partition function, because the expectation value of the spin operator acquires a very simple

form in this basis,

$$\langle \mathbf{N}|\hat{\mathbf{S}}|\mathbf{N}\rangle = S\mathbf{N}. \tag{2.10}$$

The coherent states have the minimal uncertainty for the spin to point in the $\mathbf{N}$ direction, and in that sense, they are the most similar to the classical spin. In fact, in the large-S limit, the state $|\mathbf{N}\rangle$ becomes the classical spin pointing in the direction $\mathbf{N}$. The coherent states are normalized

$$\langle \mathbf{N}|\mathbf{N}\rangle = 1, \tag{2.11}$$

but not orthogonal, $\langle \mathbf{N}|\mathbf{N}'\rangle \neq 0$, for $\mathbf{N} \neq \mathbf{N}'$, because the Hilbert space of the spin operator $\hat{\mathbf{S}}$ is $(2S+1)$-dimensional, obey the completeness relation

$$\int \frac{d\mathbf{N}}{2\pi} |\mathbf{N}\rangle\langle\mathbf{N}| = 1, \tag{2.12}$$

and thus form an overcomplete set.

The partition function, $\mathcal{Z}$, for the spin Hamiltonian (2.6) is

$$\mathcal{Z} = \mathrm{Tr}\ e^{-\beta H_S}. \tag{2.13}$$

By splitting the "time" interval β into a large number of small intervals, $\beta = M\Delta\tau$, and inserting $(M-1)$ completeness relations, the partition function reads

$$\mathcal{Z} = \lim_{M\to\infty} \prod_{m=0}^{M-1} \int \frac{d\mathbf{N}[m\Delta\tau]}{2\pi} \langle \mathbf{N}[(m+1)\Delta\tau]|e^{-\Delta\tau H_S}|\mathbf{N}[m\Delta\tau]\rangle, \tag{2.14}$$

with $\mathbf{N}(0) = \mathbf{N}(\beta)$. We can now evaluate the expectation value of each of the exponentials in the previous expression by expanding $|\mathbf{N}[\tau+\Delta\tau]\rangle$ in a power series of $\Delta\tau$ up to the linear term

$$|\mathbf{N}[\tau+\Delta\tau]\rangle = |\mathbf{N}[\tau]\rangle + \Delta\tau \frac{d}{d\tau}|\mathbf{N}[\tau]\rangle + \mathcal{O}\left((\Delta\tau)^2\right). \tag{2.15}$$

Using Eqs. (2.10) and (2.11), we obtain the expectation value

$$\langle \mathbf{N}[(m+1)\tau]|\exp(-\Delta\tau H_S)|\mathbf{N}[m\tau]\rangle = \exp\left[-\Delta\tau\left(\langle \mathbf{N}[\tau]|\frac{d}{d\tau}|\mathbf{N}[\tau]\rangle + H_S(S\mathbf{N})\right)\right]. \tag{2.16}$$

The preceding expression yields the path-integral form of the partition function (2.14)

$$\mathcal{Z} = \int \mathcal{D}\mathbf{N}(\mathbf{r},\tau)\ \delta(\mathbf{N}^2-1)\exp\left(-\mathcal{S}_B - \mathcal{S}_N\right), \tag{2.17}$$

where the Berry phase term is

$$\mathcal{S}_B = \int_0^\beta d\tau \langle \mathbf{N}[\tau]| \frac{d}{d\tau} |\mathbf{N}[\tau]\rangle. \tag{2.18}$$

The action $\mathcal{S}_N$ describes the classical dynamics of the spins governed by the Hamiltonian (2.6),

$$\mathcal{S}_N = \int_0^\beta d\tau H_S(S\mathbf{N}), \tag{2.19}$$

where $H_S(S\mathbf{N})$ is obtained by the substitution $\mathbf{S} \to S\mathbf{N}$ in the Hamiltonian (2.6), and the delta-function in the path integral explicitly accounts for the fixed-length constraint that the vector $\mathbf{N}$ obeys, $\mathbf{N}^2 = 1$.

We first construct the action (2.19) corresponding to the Hamiltonian (2.6) in which the spins are coupled to a uniform magnetic field $\mathbf{B}$

$$H_S[\mathbf{B}] = H_S - \mathbf{B} \cdot \sum_i \mathbf{S}_i. \tag{2.20}$$

Assuming that the spins order antiferomagnetically at least locally, within regions of few lattice spacings, we decompose the spin vector $\mathbf{N}(\mathbf{r}, \tau)$,

$$\mathbf{N}(\mathbf{r}_i, \tau) = \eta_i \mathbf{n}(\mathbf{r}_i, \tau) \sqrt{1 - \left(\frac{|\mathbf{L}(\mathbf{r}_i, \tau)|}{S} \right)^2} + \frac{1}{S} \mathbf{L}(\mathbf{r}_i, \tau), \tag{2.21}$$

where $\eta_i \equiv e^{i\mathbf{k}_{AF} \cdot \mathbf{r}_i}$ is the staggered factor, $\mathbf{k}_{AF} = (\pi/a, \pi/a)$ is the antiferromagnetic ordering wave vector, a is the lattice constant, and the continuous Néel field, $\mathbf{n}$, obeys the local fixed-length constraint

$$\mathbf{n}^2(\mathbf{r}, \tau) = 1. \tag{2.22}$$

The continuum field $\mathbf{L}$ represents the transverse spin canting, which is assumed to be small, $|\mathbf{L}/S| \ll 1$, because of the dominant antiferromagnetic ordering. The canting field is chosen to satisfy

$$\mathbf{n}(\mathbf{r}, \tau) \cdot \mathbf{L}(\mathbf{r}, \tau) = 0, \tag{2.23}$$

which, together with (2.22), implies that $\mathbf{N}^2 = 1$. The long-wavelength dynamics of the Néel field, $\mathbf{n}$, is determined by the effective action, which we will derive below.

The isotropic Heisenberg model

In this subsection, we derive the continuous action corresponding to the isotropic Heisenberg model (2.1). Although this is a standard textbook material, we present

it here for the sake of completeness. It is also useful for the reader interested in technical details, because the derivations of the actions corresponding to the DM and XY Hamiltonians, follow basically the same steps as the one for the Heisenberg model.

The action (2.19) corresponding to the Heisenberg Hamiltonian (2.1) reads

$$\mathcal{S}_N^H \equiv \int_0^\beta d\tau H_H(S\mathbf{N}) = JS^2 \int_0^\beta d\tau \sum_{\langle ij \rangle} \mathbf{N}_i \cdot \mathbf{N}_j,$$

with $\mathbf{N}_i \equiv \mathbf{N}(\mathbf{r}_i, \tau)$. By inserting the decomposition (2.21) of the spin vector $\mathbf{N}$ into the previous expression, expanding the square root, and keeping the terms quadratic in the uniform field $\mathbf{L}$, we obtain

$$\begin{aligned} H_H(\mathbf{n}, \mathbf{L}) &= JS^2 \sum_{\langle ij \rangle} \left\{ \eta_i \eta_j \mathbf{n}_i \cdot \mathbf{n}_j + \frac{1}{S^2} \left[\mathbf{L}_i \cdot \mathbf{L}_j - \frac{1}{2} \eta_i \eta_j \mathbf{n}_i \cdot \mathbf{n}_j (\mathbf{L}_i^2 + \mathbf{L}_j^2) \right] \right. \\ &+ \left. \frac{1}{S} \left[\eta_i \mathbf{n}_i \cdot \mathbf{L}_j + \eta_j \mathbf{n}_j \cdot \mathbf{L}_i \right] \right\}, \end{aligned} \tag{2.24}$$

with $\mathbf{n}_i \equiv \mathbf{n}(\mathbf{r}_i, \tau)$ and $\mathbf{L}_i \equiv \mathbf{L}(\mathbf{r}_i, \tau)$. We now use the gradient expansion of the field $\mathbf{n}$ on the underlying square lattice up to the second-derivative terms

$$\mathbf{n}_j = \mathbf{n}_i - r_{ij}^l \partial_l \mathbf{n}_i + \frac{1}{2} r_{ij}^l r_{ij}^m \partial_l \partial_m \mathbf{n}_i, \tag{2.25}$$

where $\mathbf{r}_{ij} \equiv \mathbf{r}_i - \mathbf{r}_j$, and the sum over the repeated indices is assumed, to obtain

$$\begin{aligned} H_H(\mathbf{n}, \mathbf{L}) &= JS^2 \sum_{\langle ij \rangle} \left\{ \eta_i \eta_j + \frac{1}{2} \eta_i \eta_j r_{ij}^l r_{ij}^m \, \mathbf{n}_i \cdot \partial_l \partial_m \mathbf{n}_i \right. \\ &+ \left. \frac{1}{S^2} \left[\mathbf{L}_i \cdot \mathbf{L}_j - \frac{1}{2} \eta_i \eta_j \left(\mathbf{L}_i^2 + \mathbf{L}_j^2 \right) \right] \right\}. \end{aligned} \tag{2.26}$$

The terms odd in the staggered factors η_i are absent, because they may be rewritten as total derivatives, yielding only trivial surface terms in the continuum action. The first term on the right-hand side in Eq. (2.26) is the classical energy of the Néel ground state, and can be discarded. In order to take the continuum limit, it is convenient to write the sum over the nearest-neighboring sites in the following way

$$\sum_{\langle ij \rangle} = \frac{1}{2} \sum_{pq} \left(\sum_{\delta_p = \pm 1} + \sum_{\delta_q = \pm 1} \right), \tag{2.27}$$

where (p, q) are the coordinates of the site i on the lattice, i.e., $\mathbf{r}_i = a(p\mathbf{e}_x + q\mathbf{e}_y)$, with $\mathbf{e}_x, \mathbf{e}_y$ being the unity vectors in the lattice directions x and y, respectively,

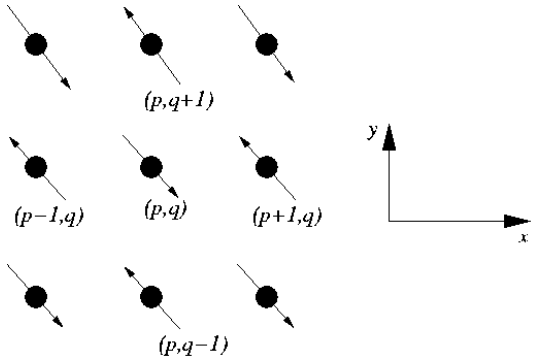

Figure 2.6: Left panel: the Néel order in the CuO_2 plane. Right panel: tetragonal xy coordinate system.

and $p, q \in \mathbb{Z}$. Here, $(p+\delta_p, q)$ and $(p, q+\delta_q)$ with $\delta_p, \delta_q = \pm 1$ are the coordinates of the four nearest-neighboring sites j of the site i, see Fig. 2.6. The second term in Eq. (2.26) then acquires the form

$$\begin{aligned} & \sum_{\langle ij \rangle} \eta_i \eta_j r_{ij}^l r_{ij}^m \, \mathbf{n}_i \partial_l \partial_m \mathbf{n}_i \\ = \; & \frac{1}{2} a^2 \sum_{pq} \left\{ \sum_{\delta_p = \pm 1} \eta_{pq} \eta_{(p+\delta_p)q} \delta_p^2 \mathbf{n}_{pq} \partial_x^2 \mathbf{n}_{pq} + \sum_{\delta_q = \pm 1} \eta_{pq} \eta_{p(q+\delta_q)} \delta_q^2 \mathbf{n}_{pq} \partial_y^2 \mathbf{n}_{pq} \right\}, \end{aligned} \tag{2.28}$$

where we used that $r^l_{(p+\delta_p)q} = a\delta_{lx}\mathrm{sign}\delta_p$, and an analogous formula for $r^l_{p(q+\delta_q)}$. The above form of the sum over the nearest-neighboring sites enables us to take the continuum limit by the substitution

$$a^2 \sum_{pq} \to \int d^2\mathbf{r}, \tag{2.29}$$

yielding

$$\sum_{\langle ij \rangle} \eta_i \eta_j r_{ij}^l r_{ij}^m \, \mathbf{n}_i \cdot \partial_l \partial_m \mathbf{n}_i \to \int d^2\mathbf{r} (\nabla \mathbf{n})^2, \tag{2.30}$$

where a partial integration was performed after taking the continuum limit to obtain the term on the right-hand side. Similarly, the continuum limit for the

third term on the right-hand side in Eq. (2.26) reads

$$\sum_{\langle ij\rangle}\left[\mathbf{L}_i\cdot\mathbf{L}_j-\eta_i\eta_j\mathbf{L}_i^2\right]=2\sum_{\langle ij\rangle}\mathbf{L}_i\cdot\mathbf{L}_j=\sum_{pq}\left\{\sum_{\delta_p=\pm1}\mathbf{L}_{(p+\delta_p)q}\cdot\mathbf{L}_{pq}\right.$$
$$\left.+\sum_{\delta_q=\pm1}\mathbf{L}_{p(q+\delta_q)}\cdot\mathbf{L}_{pq}\right\}=4\sum_{pq}\mathbf{L}_i^2\rightarrow\frac{4}{a^2}\int d^2\mathbf{r}\;\mathbf{L}^2, \tag{2.31}$$

yielding, together with Eq. (2.30), the continuum form of the Heisenberg Hamiltonian (2.26)

$$H_H(\mathbf{n},\mathbf{L})=\frac{1}{2}JS^2\int d^2\mathbf{r}\left[(\nabla\mathbf{n})^2+\frac{8}{a^2S^2}\mathbf{L}^2\right]. \tag{2.32}$$

The Dzyaloshiskii-Moriya interaction

We now derive the action (2.19) corresponding to the DM Hamiltonian (2.2)

$$\mathcal{S}_N^{DM}=\int_0^\beta d\tau H_{DM}(S\mathbf{N})=S^2\int_0^\beta d\tau\sum_{\langle ij\rangle}\mathbf{D}_{ij}\cdot(\mathbf{N}_i\times\mathbf{N}_j) \tag{2.33}$$

By using the decomposition (2.21), after expanding the square-root, and keeping only the terms quadratic in the fields $\mathbf{n}$ and $\mathbf{L}$, the DM Hamiltonian reads

$$H_{DM}(\mathbf{n},\mathbf{L})=S^2\epsilon_{\alpha\beta\gamma}\sum_{\langle ij\rangle}D_{ij}^\alpha\{\eta_i\eta_j n_i^\beta n_j^\gamma+\frac{1}{S}[\eta_i n_i^\beta L_j^\gamma+\eta_j n_j^\gamma L_i^\beta]+\frac{1}{S^2}L_i^\beta L_j^\gamma\}. \tag{2.34}$$

The gradient expansion (2.25) for the fields $\mathbf{n}$ and $\mathbf{L}$ yields

$$H_{DM}(\mathbf{n},\mathbf{L})=S^2\epsilon_{\alpha\beta\gamma}\sum_{\langle ij\rangle}D_{ij}^\alpha\{-\eta_i\eta_j r_{ij}^l n_i^\beta\partial_l n_i^\gamma-\frac{1}{2}\eta_i\eta_j r_{ij}^l r_{ij}^m\partial_l n_i^\beta\partial_m n_i^\gamma$$
$$+\frac{1}{S}[\eta_i n_i^\beta L_i^\gamma+\eta_j n_j^\gamma L_j^\beta]\}, \tag{2.35}$$

where we neglected the terms containing the gradient of the uniform spin component. In order to find the continuum limit, we transform the sum over the

nearest-neighboring sites using Eq. (2.27)

$$\begin{aligned} H_{DM}(\mathbf{n},\mathbf{L}) &= \frac{1}{2}S^2\sum_{pq}\Bigg\{\sum_{\delta_p=\pm1}\epsilon_{\alpha\beta\gamma}D^{\alpha}_{(p+\delta_p)q}[-\eta_{pq}\eta_{(p+\delta_p)q}r^{l}_{(p+\delta_p)q}n^{\beta}_{pq}\partial_l n^{\gamma}_{pq} \\ &- \frac{1}{2}\eta_{pq}\eta_{(p+\delta_p)q}r^{l}_{(p+\delta_p)q}r^{m}_{(p+\delta_p)q}\partial_l n^{\beta}_{pq}\partial_m n^{\gamma}_{pq}] \\ &+ \frac{1}{S}(\eta_{pq}n^{\beta}_{pq}L^{\gamma}_{pq}+\eta_{(p+\delta_p)q}n^{\gamma}_{(p+\delta_p)q}L^{\beta}_{(p+\delta_p)q}) \\ &+ \sum_{\delta_q=\pm1}[(p+\delta_p,q)\rightarrow(p,q+\delta_q)]\Bigg\}, \end{aligned} \tag{2.36}$$

where the terms in the second sum on the right-hand side defined on the site $p(q+\delta_q)$ are obtained by the substitution $(p+\delta_p,q)\rightarrow(p,q+\delta_q)$ from the terms defined on the site $(p+\delta_p)q$ appearing in the first sum. The DM vector $\mathbf{D}_{ij}$ has a staggered pattern, and its form in the tetragonal xy-coordinate system is

$$\mathbf{D}_{(p+\delta_p)q}=\eta_{pq}(0,d,0)\equiv\eta_{pq}\mathbf{D}^{(x)} \qquad \mathbf{D}_{p(q+\delta_q)}=\eta_{pq}(d,0,0)\equiv\eta_{pq}\mathbf{D}^{(y)}, \tag{2.37}$$

which implies that the only nontrivial contribution to the above Hamiltonian is given by

$$H_{DM}(\mathbf{n},\mathbf{L})=2Sd\sum_{pq}\left\{[\epsilon_{y\beta\gamma}+\epsilon_{x\beta\gamma}]n^{\beta}_{pq}L^{\gamma}_{pq}\right\}=4S\sum_{pq}\mathbf{D}_{+}\cdot(\mathbf{n}_{pq}\times\mathbf{L}_{pq}), \tag{2.38}$$

with the thermodynamic DM vector $\mathbf{D}_+$ defined as $\mathbf{D}_+\equiv(\mathbf{D}^{(x)}+\mathbf{D}^{(y)})/2$, see also Fig. 2.3. The continuum limit of the DM Hamiltonian then reads

$$H_{DM}(\mathbf{n},\mathbf{L})=\frac{4S}{a^2}\int d^2\mathbf{r}\ \mathbf{D}_{+}\cdot(\mathbf{n}\times\mathbf{L}). \tag{2.39}$$

It is worthwhile mentioning that if the DM vector $\mathbf{D}_{ij}$ had been a constant, $\mathbf{D}_{ij}\equiv\mathbf{D}$, it would have been coupled to the total magnetization current,

$$H^{const}_{DM}\sim\int d^2\mathbf{r}\ \mathbf{D}\cdot\sum_{\mu=x,y}(\mathbf{n}\times\partial_\mu\mathbf{n}),$$

as can be shown from Eq. (2.36), leading to the frustration of the antiferromagnetic ground state. In fact, the effective dipole fields that represent the doping introduced in the system couple to the magnetization current in the same way, giving rise to the instability of the Néel state, and affecting other magnetic properties of the compound, as it will be discussed in the following chapter of this thesis. It is also worth pointing out here that a complete class of DM helimagnets, such as $K_2V_3O_8$ and $Ba_2CuGe_2O_7$, can be described by the above model with constant DM vectors [58].

Pseudodipolar interaction

Let us now consider the effective Hamiltonian arising from the presence of the pseudodipolar interaction (2.4)

$$\mathcal{S}_N^{XY}(S\mathbf{N}) = \int_0^\beta d\tau H_{XY}(S\mathbf{N}) = S^2 \int_0^\beta \sum_{\langle ij \rangle} \mathbf{N}_i \cdot \overleftrightarrow{\Gamma}_{ij} \cdot \mathbf{N}_j, \tag{2.40}$$

with the matrix Γ given by Eq. (2.5). The construction of the long-wavelength action follows the same steps as for the Heisenberg and the DM Hamiltonians. We use the decomposition (2.21), expand the square root, keep the terms quadratic in the $\mathbf{n}$ field only, because $|\mathbf{L}/S| \ll 1$ and the pseudodipolar interaction is small in comparison with the superexchange, $\Gamma^{\alpha\beta} \ll J$. Then, by applying the gradient expansion to the field $\mathbf{n}$, we obtain

$$H_{XY} = S^2 \sum_{\langle ij \rangle} \eta_i \eta_j \Gamma_{ij}^{\alpha\beta} \{ n_i^\alpha n_j^\beta + \frac{1}{2} r_{ij}^l r_{ij}^m n_i^\alpha \partial_l \partial_m n_i^\beta \}.$$

The above sum can be transformed using Eq. (2.27), and the continuum Hamiltonian reads

$$H_{XY}(\mathbf{n}, \mathbf{L}) = -\frac{2S^2}{a^2} \int d^2\mathbf{r}\ \Gamma^{\alpha\beta} n^\alpha n^\beta + \frac{S^2}{2} \int d^2\mathbf{r}\ \Gamma_\mu^{\alpha\beta} \partial_\mu n^\alpha \partial_\mu n^\beta, \tag{2.41}$$

with the matrix Γ defined as $\Gamma \equiv (1/2)(\Gamma_{ij} + \Gamma_{ik}) = \mathrm{diag}(\Gamma_1, \Gamma_1, \Gamma_3)$, which follows from Eq. (2.5), $\Gamma_x \equiv \Gamma_{ij}$, and $\Gamma_y \equiv \Gamma_{ik}$. Noting that $\Gamma_1 \mathbf{n}^2$ only introduces an energy shift and neglecting the second term in Eq. (2.41), which is a small correction to the spin stiffness, because $\Gamma^{\alpha\beta} \ll J$, the XY Hamiltonian can be further simplified to

$$H_{XY}(\mathbf{n}, \mathbf{L}) = \frac{2S^2}{a^2} \int d^2\mathbf{r}\ \Gamma_c n_c^2, \tag{2.42}$$

with $\Gamma_c \equiv \Gamma_1 - \Gamma_3 > 0$ [53]. Therefore, the pseudodipolar interaction introduces a gap for the spin excitations along the c-axis, confining the local staggered magnetization to the ab-plane.

The only remaining term in the action (2.19) is the Zeeman term, which describes coupling of the total spin to the external magnetic field, Eq. (2.20). The continuum limit for this term can be trivially obtained

$$\mathcal{S}_N^{\mathbf{B}}(\mathbf{n}, \mathbf{L}) = -\frac{1}{a^2} \int_0^\beta d\tau \int d^2\mathbf{r}\ \mathbf{B} \cdot \mathbf{L}, \tag{2.43}$$

and the total action $\mathcal{S}_N(\mathbf{n},\mathbf{L})$ reads

$$\begin{aligned}\mathcal{S}_N(\mathbf{n},\mathbf{L}) &= \frac{1}{2}\int_0^\beta d\tau \int d^2\mathbf{r}\left\{JS^2\left[(\nabla\mathbf{n})^2+\frac{8}{a^2S^2}\mathbf{L}^2\right]\right.\\ &+ \left.\frac{8S}{a^2}\left[\mathbf{L}\cdot(\mathbf{D}_+\times\mathbf{n})\right]+\frac{4S^2}{a^2}\Gamma_c n_c^2-\frac{2}{a^2}\mathbf{B}\cdot\mathbf{L}\right\}. \qquad (2.44)\end{aligned}$$

In order to complete the path-integral expression for the partition function, Eq. (2.17), we need to express the Berry phase (2.18) in terms of the fields $\mathbf{n}$ and $\mathbf{L}$, which can be evaluated by using the explicit form of the spin coherent states (see Refs. [**?** 59] for details). In the case of an antiferromagnet, for the smooth configurations of the local staggered magnetization $\mathbf{n}(\mathbf{r},\tau)$, the Berry phase action reads

$$\mathcal{S}_B(\mathbf{n},\mathbf{L}) = -\frac{i}{a^2}\int_0^\beta d\tau\int d^2\mathbf{r}\;\mathbf{L}\cdot(\mathbf{n}\times\partial_\tau\mathbf{n})\,. \qquad (2.45)$$

In order to obtain the effective action for the staggered magnetization solely, we have to integrate out the uniform component of the total spin in the action $\mathcal{S}_N+\mathcal{S}_B$. Since this action is quadratic in the field $\mathbf{L}$, we can integrate out the uniform component using its equation of motion $\frac{\delta}{\delta\mathbf{L}}(\mathcal{S}_N+\mathcal{S}_B)=0$ and the constraint $\mathbf{n}\cdot\mathbf{L}=0$, yielding

$$\mathbf{L} = \frac{i}{8J}(\mathbf{n}\times\partial_\tau\mathbf{n})+\frac{S}{2J}(\mathbf{n}\times\mathbf{D}_+)+\frac{1}{8J}[\mathbf{B}-(\mathbf{n}\cdot\mathbf{B})\mathbf{n}]. \qquad (2.46)$$

Inserting the above expression into the actions (2.44) and (2.45), we obtain the generalized quantum nonlinear sigma model describing the long-wavelength dynamics of the spins with the microscopic Hamiltonian (2.20) [60, 61]

$$\begin{aligned}\mathcal{S}_{QNL\sigma}[\mathbf{B}] &= \frac{1}{2\tilde{g}c}\int_0^\beta d\tau\int d^2\mathbf{r}\left\{(\partial_\tau\mathbf{n}+i\mathbf{n}\times\mathbf{B})^2+c^2(\nabla\mathbf{n})^2+m_a^2n_a^2+m_c^2n_c^2\right.\\ &+ \left.8S\mathbf{n}\cdot(\mathbf{B}\times\mathbf{D}_+)\right\}, \qquad (2.47)\end{aligned}$$

with the local staggered magnetization obeying the fixed-length constraint $\mathbf{n}^2=1$. Here, $\tilde{g}=2\sqrt{2}a/S$ is the bare coupling constant, $c=2\sqrt{2}JSa$ is the spin-wave velocity, and the bare spin gaps for the excitations along a and c orthorhombic directions are defined as $m_a^2=16S^2|\mathbf{D}_+|^2$ and $m_c^2=64JS^2\Gamma_c$, respectively. The last term in the preceding action represents the coupling between the staggered magnetization and the DM vector, which is responsible for the anisotropic magnetic susceptibility response observed in the LCO compound, as it will be shown in the following section.

Let us now comment on the ground state properties following from the generalized nonlinear sigma model (2.47). Without the external magnetic field, the

action (2.47) reduces to

$$\mathcal{S}^0_{QNL\sigma} = \frac{1}{2\tilde{g}c}\int_0^\beta d\tau \int d^2\mathbf{r}\left\{(\partial_\tau \mathbf{n})^2 + c^2(\nabla \mathbf{n})^2 + m_a^2 n_a^2 + m_c^2 n_c^2\right\}. \qquad (2.48)$$

As an immediate consequence of the above form of the action, the staggered magnetization in the ground state orients along the b-orthorhombic direction, $\langle \mathbf{n}\rangle = \sigma_0 \mathbf{e}_b$, as observed experimentally [50], since the orientation in the a and the c direction would cost an energy m_a^2 and m_c^2, respectively. Moreover, the uniform spin component in the ground state is related to the staggered one, $\langle \mathbf{L}\rangle = (S/2J)(\langle \mathbf{n}\rangle \times \mathbf{D}_+)$, see Eq. (2.46), giving rise to a weak ferromagnetic moment along the c orthorhombic axis, since the vector $\mathbf{D}_+$ is oriented along the a-axis, see Fig. 2.3. Therefore, the spins in the ground state of the LCO compound are antiferromagntically ordered in the CuO_2 planes with the staggered moment along the orthorhombic b axis, and canted out of the plane with the weak ferromagnetic moment proportional to the strength of the DM interaction. Finally, when the antiferromagnetic coupling between the neighboring CuO_2 planes is included, the staggered ordering of the weak ferromagnetic moment, $\langle \mathbf{L}\rangle$, in the adjacent CuO_2 planes, arises as a consequence of the staggered pattern of the $\mathbf{D}_+$ vectors along the c-axis.

2.3 Magnetic Susceptibilities in La_2CuO_4

In this section we calculate the magnetic susceptibilities when the magnetic field is applied along the orthorhombic crystallographic axes using the nonlinear sigma model (2.47) [62]. The zero-field magnetic susceptibility for the field B_α applied along one of the orthorhombic axis $\alpha = a, b, c$ is defined as

$$\chi_\alpha = \frac{1}{\beta V}\frac{\partial^2}{\partial B_\alpha^2}\ln \mathcal{Z}[\mathbf{B}]|_{\mathbf{B}=0}, \qquad (2.49)$$

where $\mathcal{Z}[\mathbf{B}]$ is the Euclidean partition function for the field $\mathbf{n}$ with the action (2.47)

$$\mathcal{Z}[\mathbf{B}] = \int \mathcal{D}\mathbf{n}\ \delta(\mathbf{n}^2 - 1)\ e^{-\mathcal{S}_{QNL\sigma}[\mathbf{B}]}. \qquad (2.50)$$

Using the previous partition function and expanding the local staggered magnetization about its ground state value, $\langle \mathbf{n}\rangle \equiv \boldsymbol{\sigma}_0 = \sigma_0 \mathbf{e}_b$, we obtain the zero-field magnetic susceptibilities χ_α (see App. B for details)

$$\begin{aligned}
\chi_a &= \chi_a^u + \frac{\sigma_0^2}{\tilde{g}c},\\
\chi_b &= \chi_b^u + \frac{4D_+^2}{\tilde{g}c}G_c(0,0),\\
\chi_c &= \chi_c^u + \frac{\sigma_0^2}{\tilde{g}c} + \frac{4D_+^2}{\tilde{g}c}G_b(0,0),
\end{aligned} \qquad (2.51)$$

where $G_\alpha^{-1}(\mathbf{k},\omega_n) = c^2\mathbf{k}^2 + \omega_n^2 + M_\alpha^2$ is the inverse propagator for the magnetic mode α, with the gap M_α, $\omega_n \equiv 2\pi n/\beta$ is the bosonic Matsubara frequency, and $\mathbf{k}$ is the momentum. The uniform susceptibility contribution to the above total magnetic susceptibilities, arising from the nonlinear sigma model without the last term in the action (2.47), reads

$$\chi_\alpha^u = \frac{1}{\beta V}\sum_{\mathbf{q}} \left\{ G_\beta(\mathbf{q}) + G_\gamma(\mathbf{q}) - 4\omega_n^2\, G_\beta(\mathbf{q})\, G_\gamma(\mathbf{q}) \right\}, \tag{2.52}$$

with $\mathbf{q} \equiv \{\mathbf{k},\omega_n\}$, V is the volume of the system, and $(\alpha\beta\gamma) \equiv (abc)$ and its permutations. It is important to emphasize that the form of the susceptibilities, given by Eqs. (2.51), is exact, within the linear response theory, and independent of the fact that the Néel field, $\mathbf{n}$, obeys the fixed-length constraint, $\mathbf{n}^2 = 1$, and thus also valid when this constraint is relaxed, which, indeed, will be the case in the Néel phase. In order to account for this more general situation, we formally included the propagator of the b-mode in the expressions for the susceptibilities, given by Eqs. (2.51), although the longitudinal mode is not an independent degree of freedom in the description based on the nonlinear sigma model, but related to the transverse modes via the constraint, $n_b^2 = 1 - n_a^2 - n_c^2$.

Let us now turn to the evaluation of the temperature dependence of the susceptibilities χ_α, which, according to Eqs. (2.51), reduces to the calculation of the temperature dependence of the ground state staggered magnetization $\sigma_0(T)$ and the gaps $M_\alpha(T)$. Here, we evaluate these thermodynamic quantities at the mean-field level, and show that the resulting susceptibilities capture the qualitative features observed experimentally in Ref. [36] already in this approximation. We first consider the paramagnetic phase, where $\sigma_0 = 0$, by the standard large-N expansion [57], applied to the generalized QNLσ model (2.47). To proceed with the large-N expansion, we first rescale the N-component field $\mathbf{n}$, $\mathbf{n} \to \sqrt{N}\mathbf{n}$, and then represent the new constraint, $\mathbf{n}^2 = N$, obeyed by the N-component field, as an exponential by introducing the Lagrange multiplier λ. The resulting partition function reads

$$\mathcal{Z}_N = \int \mathcal{D}\mathbf{n}\mathcal{D}\lambda\ \exp\left\{ -N\left[\mathcal{S}^0_{QNL\sigma} + \frac{c}{2\tilde{g}}\int_0^\beta d\tau \int d^2\mathbf{r}\ i\lambda\left(\mathbf{n}^2 - 1\right)\right]\right\}, \tag{2.53}$$

where $\mathcal{S}^0_{QNL\sigma}$ is given by Eq. (2.48). In the limit $N \to \infty$, the main contribution to the above partition function comes from the saddle point solution for the Lagrange multiplier

$$\langle i\lambda\rangle \equiv \xi^{-2}, \tag{2.54}$$

with ξ being the correlation length, determined by the averaged constraint equation

$$1 = \frac{N}{2}(I_a + I_c), \tag{2.55}$$

where

$$I_\alpha = \frac{1}{\beta V}\tilde{g}c\sum_{\mathbf{k},\omega_n} G_\alpha(\mathbf{k},\omega_n) = \frac{\tilde{g}T}{2\pi c}\ln\left\{\frac{\sinh\left(c\Lambda/2T\right)}{\sinh\left(M_\alpha/2T\right)}\right\}. \tag{2.56}$$

The gap equations in the large-N limit follow from the action defining the partition function (2.53) and the saddle point solution (2.54)

$$M_b^2 \equiv c^2\xi^{-2}, \qquad M_a^2 = D_+^2 + c^2\xi^{-2}, \qquad M_c^2 = \Gamma_c + c^2\xi^{-2}, \tag{2.57}$$

in units of J, i.e., we set $J = 1$. Consequently, the finite values of the transverse gaps, M_a and M_c, cause the Néel temperature of the 2D system, T_N^{2D}, defined implicitly as

$$1 = \frac{N}{2}\left[I_a(\xi\to\infty) + I_c(\xi\to\infty)\right]$$

to be finite, because the finite values of the spin gaps completely break the rotational symmetry of the NLσ action (2.48), and the only remaining symmetry is the discrete Ising-like symmetry, $\mathbf{n}\to-\mathbf{n}$. Let us point out that the finite transverse gaps drive the 2D transition temperature to a finite value, whereas in the LCO compound the CuO_2 layers are coupled, and this coupling causes the 3D Néel temperature to be finite. The interlayer coupling can be included in the present model [61], but the qualitative physical picture, captured already by the single-layer model (2.47), remains the same.

In the Néel phase, it is essential to adopt a different treatment of the fixed-length constraint. Because of the importance of the longitudinal fluctuations in the ordered phase, we make the constraint locally soft by introducing a potential of the form $(u_0/2)(\mathbf{n}^2-1)^2$ in the action (2.48). Therefore, we use the so-called $O(N)$ linear sigma model

$$\mathcal{S}_{QL\sigma} = \frac{1}{2\tilde{g}c}\int_0^\beta d\tau\int d^2\mathbf{r}\left\{(\partial_\tau\mathbf{n})^2 + c^2(\nabla\mathbf{n})^2 + m_a^2n_a^2 + m_c^2n_c^2 + \frac{u_0}{2}(\mathbf{n}^2-1)^2\right\} \tag{2.58}$$

for describing the dynamics of the magnetic fluctuations below T_N, which in the limit $u_0\to\infty$ gives the fixed-length constraint, $\mathbf{n}^2 = 1$. In fact, in the ordered phase, the mass of the longitudinal mode is zero, in all orders of the $1/N$ perturbative expansion of the nonlinear sigma model, giving rise to an infinite susceptibility χ_c in the Néel phase, see Eqs. (2.51).

The ground state of the model (2.58) at zero-temperature is given by $\langle n_\alpha\rangle \equiv \sigma_{0\alpha} = \delta_{\alpha b}$. In order to find the temperature dependence of the gaps in the model, we expand the action about the ground state and integrate out the fluctuations. We thus write

$$\mathbf{n} = \boldsymbol{\sigma}_0 + \boldsymbol{\varphi}, \tag{2.59}$$

with $\boldsymbol{\varphi} = \boldsymbol{\varphi}_\parallel + \boldsymbol{\varphi}_\perp$, $\boldsymbol{\varphi}_\parallel \equiv (\boldsymbol{\varphi}\cdot\boldsymbol{\sigma}_0)/|\boldsymbol{\sigma}_0|$, representing the fluctuations about the ground state $\boldsymbol{\sigma}_0$, which yields the effective action

$$\begin{aligned}\mathcal{S}^{eff}_{QL\sigma} &= \beta V \frac{u_0}{4\tilde{g}c}\left[(\boldsymbol{\sigma}_0^2)^2 - 2\boldsymbol{\sigma}_0^2\right] + \frac{1}{2\tilde{g}c}\int_0^\beta d\tau \int d^2\mathbf{r}\left\{(\partial_\tau\boldsymbol{\varphi})^2 + (\nabla\boldsymbol{\varphi})^2\right. \\ &+ \left.\mu_\parallel^2\boldsymbol{\varphi}_\parallel^2 + \mu_{\perp\alpha}^2\varphi_{\perp\alpha}^2 + 2u_0(\boldsymbol{\sigma}_0\cdot\boldsymbol{\varphi}_\parallel)\boldsymbol{\varphi}^2 + \frac{u_0}{2}\left(\boldsymbol{\varphi}^2\right)^2\right\}, \qquad (2.60)\end{aligned}$$

with the bare masses

$$\mu_\parallel^2 = u_0\left[3\boldsymbol{\sigma}_0^2 - 1\right], \qquad \mu_{\perp\alpha} = m_\alpha + u_0\left[\boldsymbol{\sigma}_0^2 - 1\right], \quad \alpha = a, c. \qquad (2.61)$$

After integrating out the fluctuations, $\boldsymbol{\varphi}$, the one-loop effective action acquires the form [63]

$$\begin{aligned}\mathcal{S}^{1-loop}_{QL\sigma} &= \beta V\frac{u_0}{4\tilde{g}c}\left[(\boldsymbol{\sigma}_0^2)^2 - 2\boldsymbol{\sigma}_0^2\right] - \frac{1}{2}\mathrm{Tr}\ln G_\parallel - \frac{1}{2}(N-1)\mathrm{Tr}\ln G_\perp \\ &+ \frac{u_0}{4}\left[3(\mathrm{Tr}G_\parallel)^2 + 2(N-1)\mathrm{Tr}G_\parallel\mathrm{Tr}G_\perp + (N^2-1)(\mathrm{Tr}G_\perp)^2\right] \\ &+ \frac{1}{2}\mathrm{Tr}(\Delta_\parallel^{-1}G_\parallel - 1) + \frac{1}{2}(N-1)\mathrm{Tr}[\Delta_\perp^{-1}G_\perp - (N-1)], \qquad (2.62)\end{aligned}$$

where $G^{-1}_{\parallel/\perp} \equiv c^2\mathbf{k}^2 + \omega_n^2 + M^2_{\parallel/\perp}$ is the renormalized propagator of the fluctuations $\boldsymbol{\varphi}_{\parallel/\perp}$, $\Delta^{-1}_{\parallel/\perp} \equiv c^2\mathbf{k}^2 + \omega_n^2 + \mu^2_{\parallel/\perp}$ is the bare propagator of the modes $\boldsymbol{\varphi}_{\parallel/\perp}$, and the trace is over the momenta and the Matsubara frequencies, $\mathrm{Tr} \equiv \tilde{g}c\sum_{\mathbf{k},\omega_n}$. The gap equations are obtained from the previous one-loop effective action as $\delta S^{1-loop}_{QL\sigma}/\delta G_{\parallel/\perp} = 0$, and read

$$\begin{aligned}M_\parallel^2 &= \mu_\parallel^2 + u_0[3\mathrm{Tr}G_\parallel + (N-1)\mathrm{Tr}G_\perp] \\ M_\perp^2 &= \mu_\perp^2 + u_0[\mathrm{Tr}G_\parallel + (N+1)\mathrm{Tr}G_\perp], \qquad (2.63)\end{aligned}$$

with the bare masses given by Eq. (2.61), whereas the ground-state staggered magnetization is determined by $\delta S^{1-loop}_{QL\sigma}/\delta\boldsymbol{\sigma}_0 = 0$, yielding

$$\sigma_0^2 = 1 - 3\mathrm{Tr}G_\parallel - (N-1)\mathrm{Tr}G_\perp, \qquad (2.64)$$

where $\sigma_0 \equiv |\boldsymbol{\sigma}_0|$. In the large-N limit, the gap equations, as well as the equation determining the staggered magnetization, acquire a simpler form

$$\sigma_0 = 1 - \frac{N}{2}(I_a + I_c), \quad M_b^2 = 2u_0\sigma_0, \quad M_a = m_a, \quad M_c = m_c, \qquad (2.65)$$

where I_α is defined by Eq. (2.56). Observe that only the longitudinal mass M_b depends on the new energy scale $u_0 \equiv (\gamma J)^2$, which will be set by comparison with experiments. Therefore, the only difference between the descriptions based on the hard and the soft constraint is the physics of the longitudinal fluctuations. Namely,

while the nonlinear sigma model gives a gapless longitudinal mode in all orders of the $1/N$ expansion [64], in the $O(N)$ linear sigma model, this mode is gapped in the Néel phase, $T < T_N$, with the gap proportional to the staggered magnetization, as given by Eq. (2.65). On the other hand, in the paramagnetic phase, $T > T_N$, the longitudinal mass is equal to the square of the inverse correlation length, Eq. (2.57). Consequently, M_b vanishes on both the ordered and the paramagnetic side of the Néel transition, where the soft and hard versions of the constraint are expected to describe the same critical behavior.

In order to evaluate the susceptibilities χ_α, given by Eq. (2.51), and compare them with experiments, we first have to fix the large-N parameters of the model. We calculate the correlation length, given by Eqs. (2.55) and (2.57), using (in units such that $a = 1$) $\rho_s = 0.1J$, $c = 1.3J$, $J = 100$meV, and compare it with the experimental data from Ref. [16]. The values of the in-plane and out-of-plane spin gaps, $M_a(T = 0) \equiv D_+ = 2.5$meV and $M_c(T = 0) \equiv \sqrt{\Gamma}_c = 5.0$meV, are determined from neutron scattering experiments [65]. The resulting inverse correlation length compared with ξ^{-1} from Ref. [16] is shown in the inset (a) of Fig. 2.7. Let us point out that this result is obtained in the large-N limit. When the

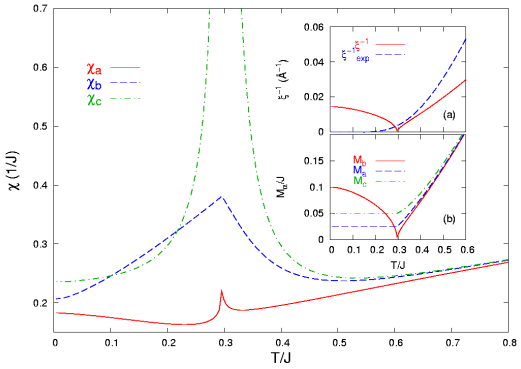

Figure 2.7: Temperature dependence of the magnetic susceptibilities χ_a, χ_b and χ_c from Eq. (2.51). Insets: (a) temperature dependence of the inverse correlation length and (b) masses $M_{a,b,c}$.

$1/N$ corrections are included, the Néel temperature will be reduced, which leads to larger and more realistic values of the parameters ρ_s, c, and J. Nevertheless, using the above values of the parameters, we may calculate the staggered moment from Eq. (2.65), $\sigma_0(T = 0) \approx 0.46$, yielding an effective moment of the Cu^{2+} spins, $\mu = g_S S \sigma_0 \mu_B \approx 0.46\mu_B$, where $g_S = 2$ is the gyromagnetic ratio for the electron, and μ_B is the Bohr magneton, which is in good agreement with experimentally measured value $\mu \sim 0.5\mu_B$ [50]. The resulting spin-gaps M_α, $\alpha = a, b, c$, are shown in the inset (b) of Fig. 2.7 for $\gamma = 0.15$, determined from the value of the

susceptibility χ_c at $T = 0$.

We will now discuss the features of the susceptibilities, given by Eq. (2.51), and show that the observed unusual behavior follows from these expressions, already at the mean-field (large-N) level, see Fig. 2.7. At large temperatures, $T \gg T_N$, all the three susceptibilities exhibit linear dependence on the temperature, as expected from the isotropic nonlinear sigma model [57]. When $\mathbf{B} \parallel a$ the source term for the $\mathbf{n}$ field is equal to zero, $\mathbf{n} \cdot (\mathbf{B} \times \mathbf{D}_+) = 0$, since $\mathbf{D}_+ \parallel a$, and thus the susceptibility χ_a has only the usual uniform contribution. The uniform susceptibility contains terms I_α, which are regular for the transverse modes gapped by the DM and XY interactions. On the other hand, the term I_b diverges logarithmically, as $T \to T_N$, since the longitudinal mass vanishes at the Néel transition, $M_b(T \to T_N) \to 0$. This appears as a small hump in the resulting susceptibility χ_a, as shown in Fig. 2.7, and it is, indeed, an artifact of the two-dimensionality of the model, as well as of the large-N limit. The coupling between the CuO_2 planes or the nonzero anomalous dimension η of the longitudinal propagator regularizes this divergence and, consequently, wipes out the hump in the susceptibility χ_a.

We now consider the susceptibilities χ_b and χ_c. When $\mathbf{B} \parallel b$ or $\mathbf{B} \parallel c$, the source term for the $\mathbf{n}$ field is nonvanishing, and gives rise to the terms D_+^2/M_c^2 and D_+^2/M_b^2 in the susceptibilities χ_b and χ_c, respectively, Eq. (2.51), which are absent in the isotropic nonlinear sigma model. These terms are responsible for the observed unusual features of the susceptibilities, as will be discussed in the following. In the vicinity of the Néel transition, when $T \to T_N$, the leading contribution to the susceptibility χ_c comes from the term D_+^2/M_b^2, since the longitudinal mass $M_b(T \to T_N) \to 0$. Thus, the susceptibility χ_c diverges at the transition, and the divergence is associated with the ferromagnetic ordering of the canted moments [51, 52]. In order to correctly reproduce the behavior of the susceptibility χ_c in the Néel phase, it is essential to relax the constraint $\mathbf{n}^2 = 1$. Namely, the nonlinear sigma model always gives gapless longitudinal mass, which leads to a diverging susceptibility χ_c in the Néel phase. Instead, in the description based on the softened version of the constraint, the longitudinal mass diverges *only* at the transition temperature, giving rise to a finite value of the susceptibility χ_c below T_N. Finally, the susceptibility χ_b exhibits a well pronounced peak at the transition temperature, instead of being divergent. This is a consequence of the term $\chi_c^{DM} \equiv D_+^2/\tilde{g}cM_c^2$, which does not diverge at T_N. Namely, according to Eq. (2.57), $M_c \to \sqrt{\Gamma}_c$, as $T \to T_N^+$, which is finite, and at the transition the value of the term χ_c^{DM} is solely determined by the ratio of the DM and XY gaps, $\chi_c^{DM} = D_+^2/\tilde{g}c\Gamma_c$. The main contribution to the susceptibility, as $T \to T_N^+$, comes from the DM term, $\chi_b^{DM} = (D_+^2/\tilde{g}c)/(\Gamma_c + c^2\xi^{-2})$, because $\xi^{-1}(T \to T_N^+) \to 0$, resulting in an increasing susceptibility as the system approaches the ordered phase. On the other hand, the out-of-plane gap, M_c, is constant in the Néel phase, and the susceptibility increses as a consequence of the increasing uniform contribution, χ_b^u, as the system approaches the transition from the ordered phase.

Let us discuss how the unusual zero-temperature hierarchy of the susceptibilities observed experimentally follows from the calculated susceptibilities given by Eq. (2.51). An ordinary easy-axis antiferromagnet, with the different in-plane and out-of-plane transverse gaps, $M_a < M_c$, exhibits the following zero-temperature hierarchy of the susceptibilities, $\chi_b^u < \chi_a^u < \chi_c^u$, i.e., the lowest susceptibility is the one along the easy-axis, and the transverse susceptibility with the smaller gap has a smaller value. This results is, indeed, obtained after dropping the terms proportional to D_+^2 in the expressions for the susceptibilities χ_b and χ_c. However, the magnetic field couples linearly to the staggered magnetization due to the presence of the DM interaction, which gives rise to the terms proportional to D_+^2 in χ_b and χ_c, leading to the following zero-temperature susceptibilities

$$\chi_a \approx \frac{\sigma_0^2}{\tilde{g}c}, \qquad \chi_b = \frac{1}{\tilde{g}c}\frac{M_a^2}{M_c^2}, \qquad \chi_c \approx \chi_a + \frac{1}{\tilde{g}c}\frac{M_a^2}{M_b^2}. \tag{2.66}$$

As a result, the hierarchy of the zero-temperature susceptibilities is different than one expected for an ordinary easy-axis antiferromagnet, rendering the LCO system an example of the unconventional easy-axis antiferromagnet. In particular, $\chi_c(0)/\chi_a(0) > 1$ always, but the ratio $\chi_b(0)/\chi_a(0)$ depends, in general, on the values of the transverse masses. For our choice of parameters, the ratio $\chi_b(0)/\chi_a(0) \sim 1.1$, is in good agreement with the experiments [36].

Chapter 3

Magnetism in Lightly Doped $La_{2-x}Sr_xCuO_4$

This chapter is based on the following publication: V. Juricic, M. B. Silva Neto, and C. Morais Smith, Phys. Rev. Lett. **96**, 077004 (2006).

In this chapter, we consider the magnetic properties of the LCO compound doped with Sr ions within the framework of a dipolar frustration model for a canted antiferromagnet [66]. Our starting point is the generalized nonlinear sigma model that incorporates both DM and XY interactions, and describes the magnetism in the undoped compound, as we discussed in the previous chapter. The holes introduced in the system via the doping are represented by an effective dipolar field that couples to the background magnetization current. As we will show, this interaction leads to a reduction of the magnon gaps, as well as of the spin stiffness. We will discuss these effects in connection with recent Raman and magnetic susceptibility measurements. We also address the ground state properties in the spin-glass phase, and demonstrate that formation of an incommensurate spin helicoid, which breaks the translational symmetry only in the spin, but not in the charge sector, is consistent with the neutron scattering, Raman and magnetic susceptibility experiments in the compound.

3.1 Introduction

The doping of the LCO compound with Sr tremendously influences the magnetic properties of the compound. The Néel temperature rapidly decreases upon doping, and the long-ranged antiferromagnetic order is completely destroyed at the Sr

concentration of $x_{AF} \simeq 2\%$, where the so-called spin-glass phase sets in. For $x_{AF} < x < x_{SC} \simeq 0.055$, in the spin-glass phase, static incommensurate magnetic correlations are observed in neutron scattering, demonstrating the importance of the spin correlations in a regime where the long-range antiferromagnetic order has been destroyed.

In order to understand the influence of the holes on the antiferromagnetic background, we adopt an approach based on a picture of isolated holes that interact with the well defined antiferromagnetic moments observed experimentally in $La_{2-x}Sr_xCuO_4$ (LSCO), for small x [67, 68]. Moreover, transport experiments suggest that, at low temperatures, holes are well localized with the localization length of a few lattice constants [69]. Therefore, it is first necessary to understand the properties of a single hole in the presence of the antiferromagnetic background, and then to proceed by including the many-body effects. The $t-J$ model, given by Eq. (1.3), which takes into account both the Heisenberg interaction between spins and the hopping of the holes in the square lattice formed by spins, has been argued [70, 17] to capture the essential low-energy physics of a doped Mott-Hubbard insulator. At half filling, when no holes are present in the system, the $t-J$ model reduces to the Heisenberg model, which, with modifications that include anisotropic interactions, as discussed in the previous chapter, describes the physics of the undoped compound. The single-hole properties within the framework of the $t-J$ model are rather well understood [71]. When holes are added into the system, their motion frustrates the antiferromagnetic background, which can be illustrated by considering a toy model, with a single hole in a background of Ising spins that interact with the coupling constant J_z [72]. A single hole at the site i is equivalent to a spin-singlet at the same site. As the hole moves, it leaves a trail of flipped spins, which obviously frustrates the antiferromagnetic ground-state, as shown in Fig. 3.1. Retracing the original path returns spins to their original position, and thus recovers the antiferromagnetic ground state. When a finite, but small transverse coupling, $J_\perp$, is included, a spin-polaron is formed in the magnetic ground state, since the hole is found at the free-particle band edge compensating the energy cost of the ferromagnetic region around the hole.

In the limit $t \gg J$ of the $t-J$ model, Shraiman and Siggia showed that the picture of a band-narrowing effect is more appropriate than the polaron formation. Namely, the holes moving in the antiferromagnetic background form a narrow quasiparticle band, with a width that scales with J, whose minima lie at the wave vectors[1] $\mathbf{k} = (\pm\pi/2, \pm\pi/2)$ in the reduced Brillouin zone. The states located around these wave vectors form four degenerate half-pockets due to Pauli exclusion principle (holes are fermions and cannot have identical momentum quantum numbers). The description based on two full pockets (valleys) at wave-vectors $(\pi/2, \pm\pi/2)$ is obtained when the two half-pockets at the opposite zone face cen-

[1] In this chapter, we use the units such that the Planck constant $\hbar = 1$, the lattice constant $a = 1$, the antiferromagnetic superexchange $J = 1$, and the Boltzman constant $k_B = 1$.

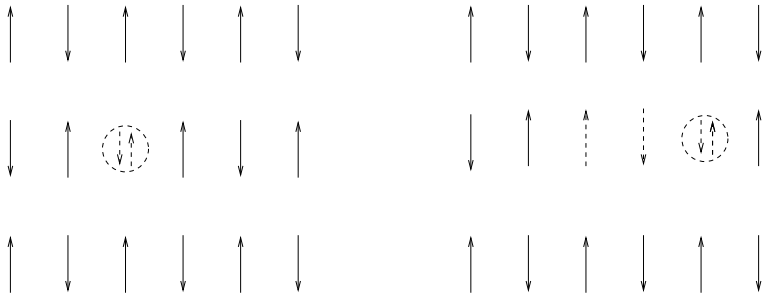

Figure 3.1: A string of overturned spins created by a hole that moved two sites to the right.

ters are shifted by the antiferromagnetic wave-vector (π, π), see Fig. 3.2. A very

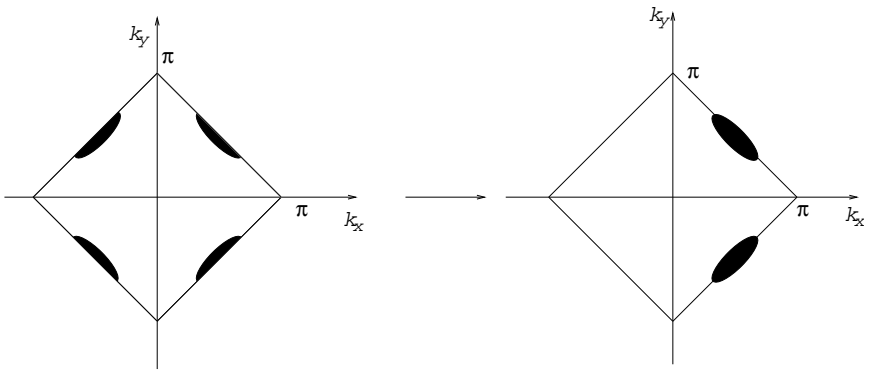

Figure 3.2: Left: Four half-pockets in reduced magnetic Brillouin zone. Right: Two full pockets obtained by shifting two half-pockets by the antiferromagnetic wave vector (π, π).

important property of the hole wave-function is that it involves a long-range dipolar distortion of the antiferromagnetic background, which eventually leads to a rearrangement of the spins in the magnetic ground-state. Using a semiclassical approach, Shraiman and Siggia in Ref. [71] have shown that a dipolar momentum $\mathbf{P}_\mu$, which is a vector in both the lattice and the spin space, can be attributed to the hole states. The Fourier transform of the dipolar moment is defined in terms

of a two-component spinor, Ψ, associated with the vacancies,

$$\mathbf{P}_\mu(\mathbf{q}) \equiv \sum_{\mathbf{k}} \sin k_\mu \bar{\Psi}_{\mathbf{k}-\mathbf{q}/2} \boldsymbol{\sigma} \Psi_{\mathbf{k}+\mathbf{q}/2}, \tag{3.1}$$

where $\boldsymbol{\sigma}$ are Pauli matrices, and the pseudospin of the holes originates from the two-sublattice structure of the antiferromagnetic background. The effective description of the holes by the dipolar field is obtained by coarse-graining, and as such it is valid at length scales much larger than the distance between holes, $l \gg k_F^{-1} \sim x^{-1/2}$, with $k_F = \sqrt{\pi x}$ being the Fermi momentum of the holes. The dipolar field, $\mathbf{P}_\mu$, defined above, is coupled to the magnetization current of the antiferromagnetic background, $\mathbf{j}_\mu \equiv \mathbf{n} \times \partial_\mu \mathbf{n}$, where $\mathbf{n}$ is the local staggered magnetization. In the Hamiltonian description of the long-wavelength fluctuations, the interaction has the following form

$$\mathcal{H}_{int} = -2\lambda \int d^2\mathbf{r} \mathbf{P}_\mu \cdot (\mathbf{n} \times \partial_\mu \mathbf{n}), \tag{3.2}$$

with $\lambda \equiv \tilde{\lambda}/T$ being the dipolar coupling constant, $\tilde{\lambda} \sim 1$ [71]. The coupling of the dipolar field, $\mathbf{P}_\mu$, to the magnetization current, $\mathbf{j}_\mu$, introduces a dipolar frustration in the system. Let us consider the effect of the dipolar frustration on the antiferromagnetic background in the classical limit of the nonlinear sigma model. In that case, the Hamiltonian of the system is given by

$$\mathcal{H}^{cl} = \frac{1}{2}\rho_s \int d^2\mathbf{r} \, (\partial_\mu \mathbf{n})^2 - 2\lambda \int d^2\mathbf{r} \, \mathbf{P}_\mu \cdot \mathbf{n} \times \partial_\mu \mathbf{n}, \tag{3.3}$$

with ρ_s being the spin stiffness. Note that, because of the constraint $\mathbf{n}^2 = 1$, the first term in the above Hamiltonian can be written as $(\partial_\mu \mathbf{n})^2 = (\mathbf{n} \times \partial_\mu \mathbf{n})^2 \equiv \mathbf{j}_\mu^2$, which enables us to express the Hamiltonian in terms of the magnetization current and the dipolar field

$$\mathcal{H}^{cl} = \frac{1}{2}\rho_s \int d^2\mathbf{r} \, \left(\mathbf{j}_\mu - 2\frac{\lambda}{\rho_s}\mathbf{P}_\mu\right)^2 - \frac{2\lambda^2}{\rho_s} \int d^2\mathbf{r} \, \mathbf{P}_\mu^2. \tag{3.4}$$

The equation of motion for the current obtained from the previous Hamiltonian

$$\mathbf{j}_\mu = 2\frac{\lambda}{\rho_s}\mathbf{P}_\mu, \tag{3.5}$$

shows that when the dipoles order, $\langle \mathbf{P}_\mu \rangle \neq 0$, the current $\langle \mathbf{j}_\mu \rangle = \langle \mathbf{n} \times \partial_\mu \mathbf{n} \rangle \neq 0$, and the spins thus rearrange to form a spatially nonuniform ground state. Let us be more specific on this point, and assume that the dipoles acquire a non-zero expectation value along the c-axis, i.e., perpendicular to the CuO_2 plane, in the spin space and along the b-axis in the lattice space, $\langle \mathbf{P}_\mu \rangle = (0, 0, P_0)\delta_{\mu b}$. Then,

Eq. (3.5) possesses a spin spiral solution, $\mathbf{n} = (\cos(Q_\mu r_\mu), \sin(Q_\mu r_\mu), 0)$, with the incommensurate wave vector $Q_\mu = Q\delta_{\mu b}$, that rotates in the plane perpendicular to the vector $\langle \mathbf{P}_\mu \rangle$, with $Q \sim P_0$. Moreover, the previous equation can be used to relate the inverse spiral pitch, Q, with the hole concentration. Assuming that the number of the ordered dipoles scales with doping, $P_0 \sim x$, and recalling that $Q \sim P_0$, the incommensurability is proportional to the hole concentration, $Q \sim x$. When quantum fluctuations are included in the model, the spin stiffness becomes negative, as shown by Shraiman and Siggia in Ref. [73], signaling the instability of the Néel state towards a spiral phase, for any finite doping.

The problem of the stability of the spiral ground state in the two-dimensional $t-J$ model has been extensively discussed, see, for example, Refs. [74, 75, 76, 77]. Auerbach and Larson have shown in Ref. [74], within a mean-field theory applied at low doping and zero temperature, that a spiral state is unstable against local enhancement of the spiral pitch, which is signaled by a negative compressibility. Mori and Hamada addressed the problem in Ref. [75] within an extended $t-J$ model, which includes the next-nearest-neighbor hopping, using the classical spin approximation. The outcome of their study is that the spiral state is unstable due to density fluctuations. On the other hand, the analysis performed in Ref. [76], based on the random-phase approximation (RPA), suggests that the spiral state is stable in the $t-J$ model. A complete analysis of the magnetic phases in the one-band Hubbard model at low doping, within the spin-density-wave formalism, has been performed in Ref. [77]. It has been shown that, depending on the strength of the interaction between holes, three different solutions of the Hubbard model are possible, at low doping. For a small interaction, the spins are antiferromagnetically ordered, whereas, for a sufficiently strong coupling, phase separation takes place. The most interesting situation occurs in the intermediate region of the interaction strength, where an incommensurate spiral state is stable. This state is different from the spiral state formed in the CuO_2 plane, as proposed by Shraiman and Siggia, and which is, indeed, a solution of the one-band Hubbard model at the mean-field level. The new incommensurate state has small components that rotate in a plane perpendicular to the CuO_2 plane, with a dominant in-plane antiferromagnetic component, as well as an in-plane incommensurate wave vector.

The issue of the stability of the spiral ground state has been recently reconsidered by Sushkov and Kotov in Refs. [34, 78] within an extended $t-J$ model,

$$\begin{aligned} H_{t-t'-t''-J} &= -t \sum_{\langle ij \rangle \sigma} c^\dagger_{i\sigma} c_{j\sigma} + H.c. - t' \sum_{\langle ij_1 \rangle \sigma} c^\dagger_{i\sigma} c_{j_1\sigma} + H.c. \\ &- t'' \sum_{\langle ij_2 \rangle \sigma} c^\dagger_{i\sigma} c_{j_2\sigma} + H.c. + J \sum_{\langle ij \rangle \sigma} \left(\mathbf{S}_i \cdot \mathbf{S}_j - \frac{1}{4} n_i n_j \right), \end{aligned} \quad (3.6)$$

where the operator $c^\dagger_{i\sigma}$ creates an electron with spin σ at site i of the two-dimensional square lattice, and is constrained to no double occupancy, the spin

operator is $\mathbf{S}_i \equiv (1/2)c^{\dagger}_{i\alpha}\boldsymbol{\sigma}_{\alpha\beta}c_{i\beta}$, and the density operator is $n_i \equiv \sum_{\sigma} c^{\dagger}_{i\sigma}c_{i\sigma}$. The above Hamiltonian is an extended version of the $t-J$ model, obtained by including hopping of the holes to the diagonal next nearest-neighbor sites $\langle ij_1\rangle$ with the hopping parameter t', and the next nearest-neighbor sites $\langle ij_2\rangle$ with the hopping parameter t''. The stability of the Néel ground state has been considered using the RPA approach, parametrically justified in the low doping regime. It has been shown that the antiferromagnetically ordered phase is unstable towards a spiral ground state, for infinitesimally small doping, due to the interaction of the spin-waves with the propagating holes. As the spiral state is concerned, it is unstable in the pure $t-J$ model ($t' = t'' = 0$) towards a local enhancement of the spiral pitch. Namely, in the semiclassical approximation, the spiral state has vanishing spin stiffness, and it is basically unstable. When the further hopping processes are included, within the extended $t-J$ model, given by Eq. (3.6), the horizontal/vertical spiral state becomes stabilized due to the quantum spin fluctuations, as shown in Refs. [34, 78]. Moreover, they argued that incommensurate magnetic correlations and superconductivity coexist within the model, as experimentally observed in the superconducting underdoped regime, $0.055 < x < 0.125$ [23]. However, the picture of the spin spiral with randomly distributed charges in the superconducting phase, is inconsistent with the observed charge peaks that accompany the incommensurate magnetic peaks. Since the periodicity of the charge peaks is twice the periodicity of the magnetic ones, these features are interpreted in terms of horizontal/vertical charge stripes, which act as antiphase domain walls for the underlying magnetic order [18]. When the system is insulating, the diagonal spiral state has a lower energy than the horizontal/vertical one due to the localization of the hole near the Sr ion [45]. Because of the presence of the kinetic (Fermi motion) energy, the horizontal/vertical spiral is energetically more favorable than the diagonal one in the superconducting state. On the other hand, in the insulating state, since the hole is trapped by the Sr ion, and thus localized, the kinetic energy does not contribute to the total energy, leading to the diagonal spiral ground state. Therefore, the jump of 45° in the direction of the incommensurability across the insulator-metal transition, which has been observed experimentally [39], can be explained using the spiral solution of the extended $t-J$ model (3.6).

Despite being able to qualitatively explain the neutron scattering data in the spin-glass and superconducting phases of LSCO, the above spiral pictures have two major problems. First, the collinear antiferromagnetic state is unstable towards a spiral formation already at infinitesimal doping, $x \neq 0$, which is in a clear contrast with the experimentally observed instability that sets in at the doping level $x = 2\%$. The second problem is related to the spiralling of the spins within the CuO_2 planes. Specifically, a featureless magnetic susceptibility measured along the a orthorhombic axis indicates that the spins remain confined to the bc plane throughout the spin-glass phase. In the following, by considering both the DM and XY anisotropies, we show that the robustness of the Néel state stems

from the presence of these anisotropies, which yield a finite critical concentration, $x_{AF} \simeq 2\%$, for the transition to the spin-glass phase. At the critical doping, a new helicoidal ground state sets in, with the small transverse components of the staggered magnetization rotating in the ac plane, accompanied by a small precession of the weak-ferromagnetic moment around the c-axis. On the other hand, the space integrated sublattice magnetization and weak-ferromagnetic moment are oriented along the b- and c-axis, respectively, thus giving rise to a total spin confined to the bc plane, in agreement with the results of magnetic susceptibility experiments [36].

3.2 Dipolar Frustration Model for a Canted Antiferromagnet

In this section, we consider the long-wave length fluctuations of the staggered ordered parameter, when the dopant holes are added into the LCO system, introducing frustration in the Néel state. As discussed in the previous chapter of this thesis, the anisotropic DM and XY interactions play a very important role in determining the magnetic properties of the undoped compound. Since the same anisotropies may be important when the system is doped as well, we adopt the generalized linear sigma model (2.58), as a starting point for our studies. The presence of static magnetic correlations within the spin-glass phase of LSCO allows us to use a Hamiltonian description of the low-energy fluctuations of the local staggered magnetization. The dynamics of the undoped compound is thus governed by the following classical Hamiltonian, corresponding to the action of the linear sigma model, given by (2.58),

$$\mathcal{H}_M = \frac{1}{2t}\int d^2\mathbf{x}\left\{(\nabla\mathbf{n})^2 + \frac{m_a^2}{2}n_a^2 + \frac{m_c^2}{2}n_c^2 + \frac{u_0}{2}(\mathbf{n}^2-1)^2\right\}, \tag{3.7}$$

where $t^{-1} \equiv \rho_s/T$ is the renormalized classical spin stiffness, with $\rho_s = S^2$. Here, we use the linear sigma model, obtained from the nonlinear sigma model by softening of the fixed-length constraint, $\mathbf{n}^2 = 1$, because we consider the dynamics of the magnetic fluctuations in the Néel phase. The bare masses m_a and m_c of the fluctuations along the a and c orthorhombic axis are related to the DM and XY anisotropies, respectively, whereas the longitudinal mode acquires a finite mass, $m_b^2 \sim u_0\sigma_0$, related to the coupling constant u_0 and to the ground-state staggered magnetization, σ_0, see Eq. (2.65), by the mechanism of spontaneous symmetry breaking.

The description of the effect of a small number of holes on the Néel state is based on the property of the hole wave-function to introduce a long-range dipolar frustration of the magnetic ground-state. In order to capture this feature, we characterize the dopant holes, in a coarse-grained description, by the dipole field,

$\mathbf{P}_\mu$, given by Eq. (3.1), which, as shown by Shraiman and Siggia [71, 73], couples to the background magnetization current as

$$\mathcal{H}_{int} = -2\lambda \int d^2\mathbf{r}\ \mathbf{P}_\mu \cdot (\mathbf{n} \times \partial_\mu \mathbf{n}). \tag{3.8}$$

Here, $\lambda \equiv \tilde{\lambda}/T$ is the dipolar coupling constant, $\tilde{\lambda} \sim 1$, and the field P^α_μ is a vector in both lattice and spin spaces. The above mathematical form belongs to a class known as *Lifshitz invariants*, which play an important role in stabilizing long-period spatially modulated structures with fixed sense of rotation of the staggered magnetization in systems like $Ba_2CuGe_2O_7$ and $K_2V_3O_8$, which are DM helimagnets, where the DM vector is constant in the bonds [58].

The dynamics of the dipolar field is described by the following classical Hamiltonian that allows for spatially nonuniform configurations of the dipoles, as well as for an interaction between the dipoles,

$$\mathcal{H}_D = \frac{1}{2\kappa} \int d^2\mathbf{x} \left\{ (\nabla \mathbf{P}_\mu)^2 + \mu^2_{\alpha\mu} (P^\alpha_\mu)^2 + \frac{v}{4} (\mathbf{P}^2_\mu)^2 \right\}. \tag{3.9}$$

Here, $\kappa = \tilde{\kappa} T$, with $\tilde{\kappa}$ being the dipole stiffness, $\mu_{\alpha\mu}$ is the bare mass of the dipole field, P^α_μ, which, in microscopic terms, is related to the energy cost of populating the μth valley of the vacancy Fermi surface with spin polarization α, and v is the coupling constant of the quartic interaction for the dipoles [79].

The total Hamiltonian of the effective theory that describes the low-energy magnetic fluctuations in the doped compound

$$\mathcal{H}_T = \mathcal{H}_M + \mathcal{H}_D + \mathcal{H}_{int} \tag{3.10}$$

thus contains the Hamiltonian (3.7), describing the dynamics of the free magnons, the Hamiltonian (3.9) for the free dipoles, and the dipole-magnetization interaction, Eq. (3.8). We first consider the effect of the magnons on the self-energy of the dipolar fields, arising from the dipole-magnetization current interaction, at the one-loop level of the perturbative expansion. The bare propagator for the magnon field, obtained from the Hamiltonian (3.7), reads

$$G^{\alpha\beta}_M(\mathbf{k}) \equiv \langle n_\alpha(-\mathbf{k}) n_\beta(\mathbf{k}) \rangle = \frac{t}{k^2 + m^2_\alpha/2} \delta_{\alpha\beta}, \tag{3.11}$$

whereas the propagator for the dipole field, with the bare Hamiltonian given by (3.9), has the form

$$G^{\alpha\beta}_{D,\mu\nu}(\mathbf{k}) \equiv \langle P^\alpha_\mu(-\mathbf{k}) P^\beta_\nu(\mathbf{k}) \rangle = \frac{\kappa}{k^2 + \mu^2_{\alpha\mu}} \delta_{\alpha\beta}\delta_{\mu\nu}. \tag{3.12}$$

In order to calculate the corrections to the dipole and the magnon propagator, it is convenient to rewrite the interaction Hamiltonian in the Fourier space. By

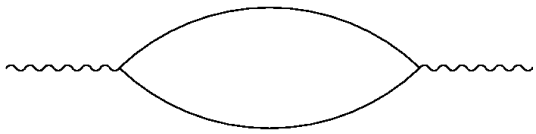

Figure 3.3: The magnon-bubble diagram for the self-energy of the dipoles in one-loop approximation, given by Eq. (3.15). Free dipole propagator, given by Eq. (3.12), is represented by wiggly line, whereas the full line represents free magnon propagator (3.11). The vertex is defined by Eq. (3.13).

performing a Fourier transform on the fields in the Hamiltonian (3.8), we obtain

$$\mathcal{H}_{int} = -i\lambda\epsilon_{\alpha\beta\gamma}\int\frac{d^2\mathbf{k}}{(2\pi)^2}\int\frac{d^2\mathbf{q}}{(2\pi)^2}\ (2k+q)_\mu P^\alpha_\mu(-\mathbf{q})n_\beta(-\mathbf{k})n_\gamma(\mathbf{k}+\mathbf{q}). \quad (3.13)$$

The dipole-magnetization current interaction yields the one-loop correction to the dipole propagator,

$$\mathcal{G}_D = G_D\sum_{n=0}^{\infty}(\Sigma_D G_D)^n = G_D(1-\Sigma_D G_D)^{-1}, \quad (3.14)$$

with the one-loop self-energy, $\Sigma^{\alpha\beta}_{\mu\nu}$, given by the magnon-bubble diagram, see Fig. 3.3

$$\Sigma^{\alpha\beta}_{D,\mu\nu}(\mathbf{q}) = (t\lambda)^2\epsilon_{\alpha\gamma\delta}\epsilon_{\beta\gamma\delta}\int\frac{d^2\mathbf{k}}{(2\pi)^2}\frac{(2k-q)_\mu(2k-q)_\nu}{[k^2+m^2_\gamma/2][(\mathbf{k}-\mathbf{q})^2+m^2_\delta/2]}. \quad (3.15)$$

The Fermi wave-vector $k_F = \sqrt{\pi x}$ provides the cutoff in the momentum integrals, because the coarse-grained description employed here is valid on length scales much larger than the distance between holes, $l \gg k_F^{-1} \sim x^{-1/2}$ [71, 79]. This result allows us to calculate the dipole mass renormalization, which is the correction to the dipole self-energy at zero momentum, using the one-loop dipole correlation function (3.14). The self-energy (3.15), at zero momentum, is regular, because of the finite magnon gaps, and diagonal in both the spin and lattice spaces,

$$\Sigma^{\alpha\beta}_{D,\mu\nu}(0) = 4(t\lambda)^2\delta_{\mu\nu}\delta_{\alpha\beta}\int\frac{d^2\mathbf{k}}{(2\pi)^2}\frac{k_\mu k_\mu}{(k^2+m^2_\gamma/2)(k^2+m^2_\delta/2)}, \qquad \alpha,\beta\neq\gamma\neq\delta. \quad (3.16)$$

Here, we used the following formula,

$$\int\frac{d^2\mathbf{k}}{(2\pi)^2}k_\mu k_\nu F(k) = \frac{1}{2}\delta_{\mu\nu}\int\frac{d^2\mathbf{k}}{(2\pi)^2}k^2F(k) = \delta_{\mu\nu}\int\frac{d^2\mathbf{k}}{(2\pi)^2}k_\mu k_\mu F(k), \quad (3.17)$$

with $F(k)$ being a function of the wave-vector modulus, k, only. Then, the renormalized mass is readily obtained from the one-loop correlation function, given by (3.14), at zero momentum,

$$\mathcal{M}^2_{\alpha\mu} = \mu^2_{\alpha\mu} - 8\kappa(t\lambda)^2 \int \frac{d^2\mathbf{k}}{(2\pi)^2} \frac{k_\mu k_\mu}{(k^2 + m^2_\gamma/2)(k^2 + m^2_\delta/2)}, \qquad \alpha \neq \gamma \neq \delta. \quad (3.18)$$

Straightforward calculation of the previous integral yields

$$\mathcal{M}^2_{\alpha\mu} = \mu^2_{\alpha\mu} - \frac{\kappa}{\pi}(t\lambda)^2 \frac{1}{m^2_\delta - m^2_\gamma} \left\{ m^2_\delta \ln\left(1 + \frac{k^2_F}{m^2_\delta}\right) - m^2_\gamma \ln\left(1 + \frac{k^2_F}{m^2_\gamma}\right) \right\}. \quad (3.19)$$

Since the integrand in Eq. (3.18) is positive, the dipole mass becomes reduced, which is a consequence of the antisymmetric form of the dipolar interaction, Eq. (3.8), involving one spatial derivative of the magnon field. Another consequence of this interaction concerns the anisotropy of the renormalized dipole masses. Indeed, even when the bare masses are isotropic in the spin space, $\mu_{\alpha\mu} \equiv \mu_\mu$, the renormalized ones, given by (3.19), may be anisotropic due to the dipolar interaction, Eq. (3.8), which involves different magnon modes. Moreover, an instability towards a phase in which the dipoles order may occur at the point where the mass of one of the dipole fields vanishes. In particular, if the mass $\mathcal{M}_{\alpha\mu}$ vanishes, the dipolar field acquires a nonzero expectation value in the direction μ and α in the lattice and the spin space, respectively, $\langle P^\alpha_\mu \rangle \neq 0$, because of the quartic interaction present in the dipole Hamiltonian (3.9). Furthermore, when the bare DM and XY masses are zero, $m_a = m_c = 0$, the dipoles order for an infinitesimal doping, because the momentum integral in Eq. (3.18) logarithmically diverges, leading to an instability of the Néel ground state. Finally, assuming that the bare dipole masses are isotropic in the spin space, $\mu_{\alpha\mu} \equiv \mu_\mu$, we conclude from the form of the renormalized masses, Eq. (3.25), and the hierarchy of the bare magnon masses, $m_a < m_c \ll m_b$, that the dipole mass, $\mathcal{M}_{\alpha\mu}$, with the spin component along the b orthorhombic axis becomes negative first. The DM and XY magnon modes with the bare masses m_a and m_c, respectively, are the lightest ones in the system, and thus according to Eq. (3.18), the reduction of the dipole mass, $\mathcal{M}_{\alpha\mu}$, with the spin component along the b orthorhombic axis, $\mathcal{M}_{b\mu}$, is larger than for the other dipole masses, $\mathcal{M}_{a\mu}$ and $\mathcal{M}_{c\mu}$. Consequently, the mass of the dipole field P^b_μ, $\mathcal{M}_{b\mu}$, becomes negative first, and thus the dipole field acquires a nonzero expectation value along the b orthorhombic axis in the spin space.

As the lattice part is concerned, it is evident from Eq. (3.19) that, if the bare dipole masses are isotropic, the renormalized ones have the same property, which is due to the fact that the one-loop correction of the dipole self-energy involves only magnons. Therefore, hierarchy of the dipole masses in the lattice space is preserved, and the smaller one vanishes first. Unfortunately, we could not find the mechanism that would give rise to such an anisotropy of the bare masses in the lattice space, and therefore, within our model, the bare dipole masses are isotropic

in the lattice space as well, $\mu_{\gamma\mu} \equiv \mu$. In order to determine the lattice space direction in which the dipole field acquires a nonzero expectation value, we thus use comparison with experiments, as will be discussed in Sec. 3.4 in more detail.

3.3 Canted Néel State

In this section, we consider the effect of the doping on the canted Néel state in the low doping regime, i.e., when the dipolar field has vanishing expectation value, $\langle \mathbf{P}_\mu \rangle = 0$, whereas both the Néel order parameter and the weak ferromagnetic moment are nonzero, $\langle \mathbf{n} \rangle \neq 0$ and $\langle \mathbf{L} \rangle \sim \langle \mathbf{n} \rangle \times \mathbf{D}_+ \neq 0$, respectively. The fluctuating dipoles, because of their coupling to the magnetization current, give rise to the correction to the magnon propagator, which we calculate here in the one-loop approximation. After resumming the contributions arising from the one-loop self-energy, the one-loop magnon propagator reads

$$\mathcal{G}^M = G^M \sum_{n=0}^{\infty} (\Sigma^M G^M)^n = G^M (1 - \Sigma^M G^M)^{-1}. \tag{3.20}$$

Here, the one-loop self-energy contains one dipole and one magnon propagator in the corresponding loop, see Fig. 3.4, and has the form

$$\Sigma^M_{\alpha\beta}(\mathbf{q}) = \kappa t \lambda^2 \epsilon_{\alpha\gamma\delta}\epsilon_{\beta\gamma\delta} \int \frac{d^2\mathbf{k}}{(2\pi)^2} \frac{(k+q)_\mu (k+q)_\mu}{(k^2 + m_\gamma^2/2)[(\mathbf{k}-\mathbf{q})^2 + \mu^2_{\delta\mu}]} \equiv \Sigma^M_\alpha(\mathbf{q})\delta_{\alpha\beta}, \tag{3.21}$$

with

$$\Sigma^M_\alpha(\mathbf{q}) \equiv \kappa t \lambda^2 \epsilon_{\alpha\gamma\delta}\epsilon_{\alpha\gamma\delta} \int \frac{d^2\mathbf{k}}{(2\pi)^2} \frac{(\mathbf{k}+\mathbf{q})^2}{(k^2 + m_\gamma^2/2)[(\mathbf{k}-\mathbf{q})^2 + \mu^2]}, \tag{3.22}$$

where we used that the bare dipole masses are isotropic in both lattice and spin spaces. The above self energy, as well as Eq. (3.20), then yield the magnon propagator in the one-loop approximation

$$\mathcal{G}^M_{\alpha\beta}(\mathbf{q}) = \frac{t\delta_{\alpha\beta}}{q^2 + m_\alpha^2/2 - t\Sigma^M_\alpha(\mathbf{q})}, \tag{3.23}$$

with Σ^M given by Eq. (3.22).

This self-energy determines the one-loop corrections to the magnon mass and stiffness, which are obtained by expanding the self-energy in a power-law series, up to the second order in momentum,

$$\Sigma^M_\alpha(\mathbf{q}) = \Sigma_\alpha(0) + \frac{1}{2} q_\mu q_\nu \frac{\partial^2 \Sigma_\alpha(\mathbf{q})}{\partial q_\mu \partial q_\nu}|_{\mathbf{q}=0} + \mathcal{O}(q^3). \tag{3.24}$$

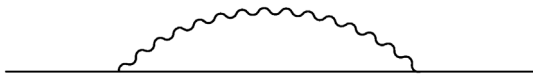

Figure 3.4: The one-loop self-energy of the magnons, given by Eq. (3.22).

The first term in this expansion gives the correction to the magnon mass due to its interaction with the dipoles

$$M_\alpha^2 = m_\alpha^2 - 2\kappa(t\lambda)^2\epsilon_{\alpha\beta\gamma}\epsilon_{\alpha\beta\gamma}\int \frac{d^2\mathbf{k}}{(2\pi)^2}\frac{k^2}{(k^2+m_\beta^2/2)(k^2+\mu^2)}. \tag{3.25}$$

Straightforward evaluation of the previous integral gives for the mass reduction of the magnon mode α

$$M_\alpha^2 = m_\alpha^2 - \frac{1}{4\pi}\kappa(t\lambda)^2\epsilon_{\alpha\beta\gamma}\epsilon_{\alpha\beta\gamma}\frac{1}{\mu^2-m_\beta^2/2}\left\{\mu^2\ln\left(1+\frac{k_F^2}{\mu^2}\right)-\frac{m_\beta^2}{2}\ln\left(1+\frac{2k_F^2}{m_\beta^2}\right)\right\}. \tag{3.26}$$

The quadratic term in momentum in the expansion (3.24) of the magnon self-energy leads to a reduction of the spin stiffness,

$$\tilde{\rho}_{s\mu\nu} = \rho_s\delta_{\mu\nu} - \delta_{\mu\nu}\kappa(t\lambda)^2\epsilon_{\alpha\beta\gamma}\epsilon_{\alpha\beta\gamma}\int\frac{d^2\mathbf{k}}{(2\pi)^2}\frac{(k^2)^2+\mu^4}{(k^2+m_\beta^2/2)(k^2+\mu^2)^3}, \tag{3.27}$$

which can be expressed in the form (see App. C for the details)

$$\begin{aligned}\tilde{\rho}_{s\mu\nu} &= \rho_s\delta_{\mu\nu} - \delta_{\mu\nu}\kappa(t\lambda)^2\epsilon_{\alpha\beta\gamma}\epsilon_{\alpha\beta\gamma}\left\{\frac{1}{4\pi}\frac{\mu^4+m_\beta^4/4}{(\mu^2-m_\beta^2/2)^3}\left[\ln\left(1+\frac{2k_F^2}{m_\beta^2}\right)\right.\right.\\ &- \left.\left.\ln\left(1+\frac{k_F^2}{\mu^2}\right)\right] - \frac{1}{4\pi}\frac{k_F^2(k_F^2m_\beta^2/2+\mu^2k_F^2+\mu^4)}{(\mu^2-m_\beta^2/2)^2(\mu^2+k_F^2)^2}\right\}.\end{aligned} \tag{3.28}$$

It is now evident, from Eqs. (3.25) and (3.27), that, within the dipolar frustration model for a canted antiferromagnet, given by Hamiltonian (3.10), the dipole interaction (3.8), gives rise to a reduction of the magnon masses and the stiffness, which eventually leads to the instability of the antiferromagnetic ground state. On the other hand, the DM and XY anisotropies give robustness to the Néel state, namely, the vanishing of one of the transverse magnon modes occurs only at a finite doping concentration, because these interactions gap the transversal magnon modes, $m_a \neq 0$ and $m_c \neq 0$. The evolution of the DM gap with doping has recently been measured in Raman scattering experiments by Gozar *et al.* [80], see Fig. 3.5. Their results show that the DM gap decreases with doping and vanishes at the

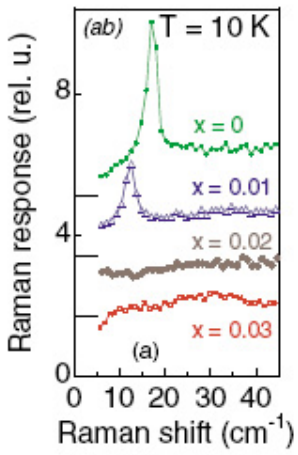

Figure 3.5: Doping dependence of the DM gap in the detwinned LSCO single crystal measured by Raman spectroscopy at $T = 10$K, as reported in Ref. [80].

doping level, $x = x_{AF} \simeq 2\%$, when the spin-glass phase sets in. Inside the antiferromagnetic phase, the only available experimental point is at doping concentration of $x = 1\%$, and the measured reduction of the DM gap is about 26%. This result suggests that the DM gap is strongly affected by the presence of the dopant holes, and its reduction cannot be explained simply from the linear decrease of the tilting angle of the CuO_6 octahedra with doping, which is known to happen in the LTO phase of the LSCO compound. The DM gap scales linearly with the tilting angle of the oxygen octahedra, $D_+ \sim x$, and, consequently, a decrease of the tilting angle results in a reduction of the DM magnon gap that is linear with doping. Therefore, the expected reduction of the DM gap arising from this mechanism is of the order of a few percent, much smaller than the observed decrease of 26%. The reduction of the DM gap, within our model, in the one-loop approximation, is self-consistently determined by Eqs. (3.19) and (3.26), and is a consequence of the frustration mechanism, provided by the coupling of the effective dipole field to the magnetization current, as described by the Hamiltonian (3.8). Therefore, in order to find the doping dependence of the gaps in the system, we have to solve self-consistently this set of gap equations. Instead of analyzing the full self-consistent set of equations, we adopt here a different approach, which allows us to obtain some analytical results, namely, in first approximation, we consider this system of the gap equations as being uncoupled. Then, using the bare value of the parameters of the model, $\tilde{\kappa} \sim 1.1$, $\tilde{\lambda} \sim 1$, $t \sim 1/S^2$, $m_a \sim 2.5 \cdot 10^{-2}$, $m_c \sim 5 \cdot 10^{-2}$, and $\mu \sim 1$ [79], we determine the doping dependence of the DM gap, as given by Eq. (3.26), and the result we show in Fig. 3.6. We obtain a reduction of the DM

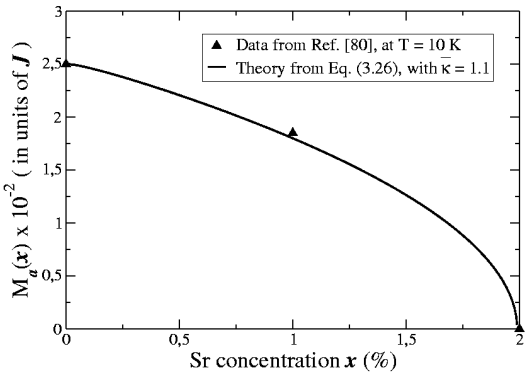

Figure 3.6: Doping dependence of the DM gap as given by Eq. (3.26) using the bare parameters of the model. Experimental data from Ref. [80] taken at $T = 10$ K.

gap at the doping concentration $x = 1\%$ of about 27%, in good agreement with the experiments. Moreover, the vanishing of the DM gap determines the critical concentration at which the transition to the spin-glass phase takes place. This critical concentration is calculated numerically, by using the bare parameters of the model, as a solution of the equation $M_a(x_{AF}^{th}) = 0$, with $M_a(x)$ given by Eq. (3.26) (recall that $k_F = \sqrt{\pi x}$), and the obtained value, $x_{AF}^{th} \simeq 2\%$, is in agreement with experiments [80].

Let us now discuss our results in connection with recent magnetic susceptibility experiments [36]. The only effect of doping, within our model, is the reduction of the magnon masses and spin stiffness, as given by Eqs. (3.25) and (3.27), respectively. Therefore, we expect the qualitative features of the magnetic susceptibilities in the antiferromagnetic phase of LSCO to remain the same as in the undoped compound, see Fig. 2.5. The only difference that we expect to appear is the shift of the peak in the susceptibilities χ_b and χ_c towards lower temperatures, as a consequence of the reduction of both the magnon masses and the spin stiffness, which, in turn, gives rise to a decrease in the Néel temperature. These features have indeed been experimentally observed, see Fig. 3.7. Furthermore, the unusual zero-temperature hierarchy of the susceptibilities, $\chi_a < \chi_c < \chi_b$ is preserved in the antiferromagnetic region of the doped compound, once the van Vleck anisotropic contribution to χ_c, which is of the order of $(1 - 1.5) \times 10^{-7}$emu/g, is substracted

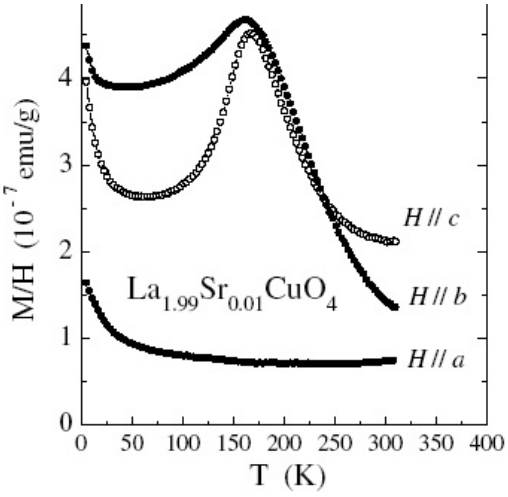

Figure 3.7: Temperature dependence of the magnetic susceptibilities in $La_{2-x}Sr_xCuO_4$ for the Sr concentration $x = 1\%$, as presented in Ref. [36].

[36]

$$\chi_a \approx \frac{\sigma_0^2}{t}, \qquad \chi_b = \frac{1}{t}\frac{D_+^2}{M_c^2(x)}, \qquad \chi_c \approx \chi_a + \frac{1}{t}\frac{D_+^2}{M_b^2(x)}, \tag{3.29}$$

where σ_0 measures the Cu^{2+} effective moment [62].

3.4 Helicoidal phase in $La_{2-x}Sr_xCuO_4$

In this section, we study the magnetic properties of the LSCO compound in the doping region where the dipoles acquire a nonzero expectation value, $\mathbf{P}_\mu \neq 0$, and, as we show below, an instability of the antiferromagnetic phase towards a helicoidal magnetic state occurs. The form of the dipole self-energy, Eq. (3.19) and the discussion following it, lead us to conclude that the dipoles order along the b orthorhombic axis in the spin space, as a consequence of the hierarchy of the magnon masses, $m_a < m_c \ll m_b$. As the lattice part is concerned, our model is isotropic, and as such, cannot determine the lattice direction in which the dipoles order. In order to fix the lattice direction of the dipole field, we recall that the direction of the incommensurate wave vector is directly related to the lattice part of the dipole field. Neutron scattering experiments in the doping region $2\% < x < 5\%$ show two diagonal incommensurate peaks oriented along the b orthorhombic axis,

thus suggesting that the dipoles order along this lattice direction. Therefore, at the point of the instability of the antiferromagnetic phase, the dipole field acquires a nonzero expectation value along the b direction in both the spin and lattice spaces (recall that we use the orthorhombic *bac* coordinate system),

$$\langle \mathbf{P}_\mu \rangle = (P_0, 0, 0)\delta_{\mu b}, \tag{3.30}$$

leading eventually to a new nonuniform configuration of the staggered magnetization in the ground state of the system.

In order to obtain the form of the nonuniform configuration, we have to solve the corresponding equations of motion arising from the Hamiltonian of the model, given by Eq. (3.10). It can be readily shown that for the dipole field, given by Eq. (3.30), the magnetic Hamiltonian reduces to

$$\mathcal{V} \equiv \frac{1}{2t} \int d^2\mathbf{r} \left[(\nabla \mathbf{n})^2 - 2\tilde{P}_0 n_a \partial_b n_c + \frac{m_a^2}{2} n_a^2 + \frac{m_c^2}{2} n_c^2 \right], \tag{3.31}$$

The corresponding equations of motion for the fields n_a and n_c read

$$\begin{aligned} &\nabla^2 n_a + \tilde{P}_0 \partial_b n_c - \frac{m_a^2}{2} n_a = 0, \\ &\nabla^2 n_c - \tilde{P}_0 \partial_b n_c - \frac{m_c^2}{2} n_c = 0, \end{aligned} \tag{3.32}$$

with $\tilde{P}_0 \equiv -4\lambda t P_0 = -4\tilde{\lambda}\rho_s P_0$, and the component n_b determined by the fixed-length constraint, $n_b^2 = 1 - n_a^2 - n_c^2$. The spatially periodic solution of the above equations of motion has the form

$$n_a(\mathbf{r}) = \sigma_a \sin(\mathbf{Q}\cdot\mathbf{r}), \qquad n_c(\mathbf{r}) = \sigma_c \cos(\mathbf{Q}\cdot\mathbf{r}), \tag{3.33}$$

with the incommensurability directed along the b orthorhombic axis, $Q_\mu = Q\delta_{\mu b}$. By substituting Eq. (3.33) into Eq. (3.32), we obtain a system of linear equations for σ_a and σ_c, whose consistency condition determines the incommensurability,

$$2Q^2 = \tilde{P}_0^2 - \frac{m_a^2}{2} - \frac{m_c^2}{2} + \sqrt{\left(\tilde{P}_0^2 - \frac{m_a^2}{2} - \frac{m_c^2}{2}\right)^2 - m_a^2 m_c^2}, \tag{3.34}$$

which yields

$$\sigma_c = -\sigma_a \frac{Q^2 + m_a^2/2}{\tilde{P}_0 Q}. \tag{3.35}$$

The sign in front of the square-root in Eq. (3.34) is determined from the condition that the incommensurability in the gapless system appears when the dipoles order. Therefore, the staggered order parameter, given by Eq. (3.33) is helicoidal, and

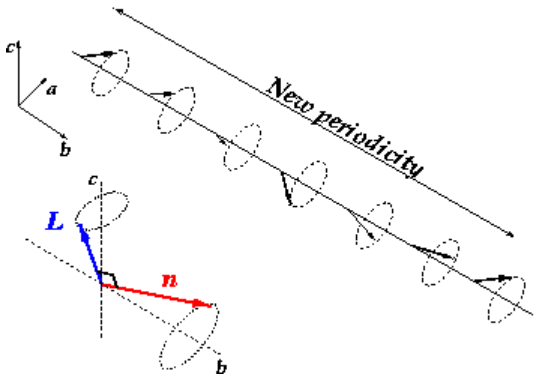

Figure 3.8: Helicoidal configuration of the staggered magnetization formed above the critical doping $x_{AF} \simeq 2\%$. Notice that the longitudinal component is the largest, whereas the transverse ones are much smaller and describe an ellipse in the ac plane.

its transverse components, n_a and n_c, rotate in the plane perpendicular to the b orthorhombic axis, as shown in Fig. 3.8. Such a magnetic texture arises as a result of the competition between the anisotropies, m_a and m_c, which favor the staggered magnetization along the b-axis, and $\langle \mathbf{P}_\mu \rangle$, which supports a rotation of the staggered order parameter in the ac plane. The usual assumption at this point is that the expectation value of the dipole field scales linearly with doping, $\langle \mathbf{P}_\mu \rangle \sim x$, and is thus small in the regime of low doping. As a result, the staggered part of the helicoidal spin configuration has small components in the ac plane, as shown in Fig. 3.8. The obtained helicoidal spin configuration is in agreement with the result of Chubukov and Musaelian [77], who indeed found a similar ground-state configuration in the one-band Hubbard model, using the spin-density-wave formalism.

We can now compare our results with neutron scattering experiments [39]. The helicoidal spin configuration is incommensurate, with the incommensurability vector along the b axis, $Q_\mu = Q\delta_{\mu b}$. The incommensurability corresponds to the inverse helix pitch, and manifests as two incommensurate peaks in the b direction, seen by neutron scattering at the wave vectors $\mathbf{k} = (\pi, \pi) \pm \mathbf{Q}$ inside the spin-glass phase. Furthermore, neutron scattering experiments reveal that, inside the spin-glass phase, the incommensurability scales linearly with doping, with a deviation from such a behavior at the doping concentration $x \sim 2.4\%$, see Fig. 4.1. We can qualitatively explain this behavior within our model, using Eq. (3.34) with the renormalized magnon gaps, and assuming that the expectation value of the dipole field scales linearly with doping, $P_0 \sim x$. We then obtain that $Q^2 \sim x^2 - M_c^2/2$,

because the DM gap vanishes at x_{AF}, $M_a(x > x_{AF}) = 0$. It is now clear that, at the onset of the spin-glass phase, the incommensurability deviates from the linear behavior, because of a small, but finite value of the XY gap. For higher doping, we expect the XY gap to decrease further, and eventually to vanish. At this point, the linear doping dependence of the incommensurability will then be recovered. A measurement of the doping dependence of the XY gap by Raman scattering, for instance, could test our theory to show whether the vanishing of the XY gap coincides with the onset of the linear behavior of the incommensurability with the doping.

Besides establishing the relationship between neutron and Raman scattering experiments, our theory allows still for another new theoretical prediction concerning the influence of a perpendicular magnetic field on the behavior of the incommensurability. Calculations of the dependence of the XY gap on a perpendicular magnetic field show that the XY gap softens at low fields [81], see Fig. 3.9. This analysis has been performed for the LCO compound, in the framework of the

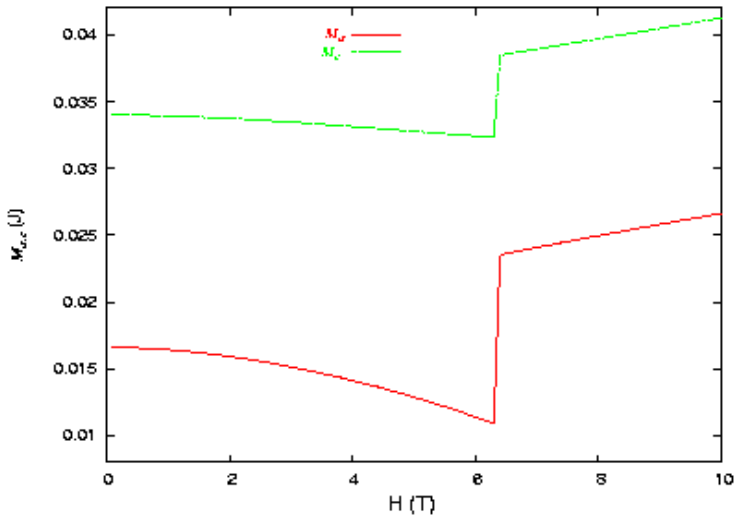

Figure 3.9: Magnetic-field dependence of the XY gap (upper curve) and the DM gap (lower curve) from Ref. [81]. Notice that the XY gap softens at low fields, before the spin-flop transition takes place.

generalized nonlinear sigma model, given by Eq. (2.47), but the result that the XY gap in the perpendicular magnetic field is reduced remains valid for the model (3.10) describing the doped compound, because, within our model, the dipoles do not couple to the magnetic field. Even if that were the case, the effect of the

dipole-magnetic field coupling would be small, because of the low magnetic fields considered, and thus the primary effect would be the reduction of the gap by the doping. The secondary effect would be the softening of the gap by the magnetic field, and then the dipole-magnetic field interaction would eventually affect the value of the gap. As we discussed above, the incommensurability is related to the XY gap and the doping as $Q^2 \sim x^2 - M_c^2/2$, and thus the softening of the XY gap in the perpendicular magnetic field causes a shift in the incommensurability towards a larger value than without the magnetic field, and its doping dependence therefore reapproaches the linear behavior. On the other hand, the expected behavior of the incommensurability in the case of stripe formation is completely different. In the stripe picture, when a perpendicular magnetic field is applied to the system, the intensity of the incommensurate peaks enhances, but the value of the incommensurability remains unchanged, as experiments by Lake *et al.* indicate [82]. Therefore, a measurement of the doping dependence of the incommensurability by neutron scattering in the presence of a magnetic field applied perpendicularly to the CuO_2 planes, is the "smoking-gun" experiment for discriminating between the scenario based on the formation of a helicoid and the diagonal stripe picture. However, a high precision measurement of the incommensurability is required, because the softening of the gap is very small.

Let us now discuss the consequences of our findings from the point of view of the magnetic susceptibility. The uniform spin component,

$$\mathbf{L}(\mathbf{r}) = \frac{1}{2}(\mathbf{n} \times \mathbf{D}_+) = D_+(-\sigma_c \sin(\mathbf{Q} \cdot \mathbf{r}), 0, n_b) \tag{3.36}$$

has a small spatially modulated component along the b-axis, and a constant component perpendicular to the CuO_2 planes. Therefore, the total space integrated magnetization,

$$\mathbf{M} = \frac{1}{V} \int d^2\mathbf{r} \langle \mathbf{L}(\mathbf{r}) \rangle = \left(0, 0, \frac{n_b D_+}{2}\right) \tag{3.37}$$

is along the c-axis, as in the undoped compound, indicating that, on average, the spins in the lightly doped compound remain confined to the bc plane. Since the magnetic susceptibility is obtained from the total magnetization, $\mathbf{M}$, the magnetic susceptibility response of the system will be qualitatively the same as in the undoped compound, yielding, in particular, a featureless susceptibility in the a direction, χ_a. These findings are, indeed, consistent with susceptibility measurements performed in lightly doped LSCO by Lavrov *et al.* [36], which show that the susceptibility χ_a, is featureless and has a constant magnitude of about 1×10^{-7}emu/g, at moderate temperatures, $T \sim 100 - 300$K, signaling that the Cu^{2+} spins are confined to the bc plane.

Finally, we provide an estimate for the critical concentration, x_{AF}^{th}, at which the instability to the helicoidal phase takes place, from the vanishing of the dipole

mass $\mathcal{M}_{bb}$, at zero temperature, when the one-loop correction due to the dipole-magnetization current interaction is included. As we discussed in the beginning of this section, the dipoles order in the b direction in both the lattice and the spin spaces, which is a consequence of the vanishing mass, $\mathcal{M}_{bb}$, at the transition point. In order to calculate the one-loop correction to the dipole mass at $T = 0$, let us recall that the one-loop self-energy contains a magnon-bubble, see Fig. 3.3, which, at zero temperature, includes the quantum propagators for the magnon fields. These propagators are obtained from the generalized quantum nonlinear sigma model (2.48), and read

$$\langle P^{\alpha}_{\mu}(-\omega_n, -\mathbf{k}) P^{\beta}_{\nu}(\omega_n, \mathbf{k})\rangle = \frac{\tilde{g}c}{\omega_n^2 + c^2k^2 + M_{\alpha}^2}\, \delta_{\mu\nu}\delta_{\alpha\beta}. \tag{3.38}$$

The one-loop dipole propagator has the form (3.14), with the self-energy that includes quantum fluctuations of the magnon fields ($\alpha, \beta \neq \gamma \neq \delta$)

$$\begin{aligned} \Sigma^{\alpha\beta}_{D,\mu\nu}(\omega, \mathbf{q}) &= 2(\tilde{g}c\tilde{\lambda})^2\delta_{\alpha\beta}\int_{-\infty}^{\infty}\frac{d\omega}{2\pi}\int\frac{d^2\mathbf{k}}{(2\pi)^2}\frac{(2k-q)_{\mu}(2k-q)_{\nu}}{(\omega^2 + c^2k^2 + M_{\gamma}^2/2)} \\ &\times \frac{1}{(\omega^2 + c^2(\mathbf{k}-\mathbf{q})^2 + M_{\delta}^2/2)}. \end{aligned} \tag{3.39}$$

Here, since we consider the zero-temperature case, the Matsubara frequency becomes a continuous variable, and the finite temperature sum, $T\sum_{\omega_n}$, becomes now the integral over this continuous variable, $\int_{-\infty}^{\infty}\frac{d\omega}{2\pi}$. We also take into account the mass renormalization for the magnon fields by considering the renormalized masses in the corresponding propagators. Using Eq. (3.14), the mass correction acquires the form

$$\mathcal{M}_{\alpha\nu} = \mu^2 - 8\tilde{\kappa}(\tilde{g}c\tilde{\lambda})^2\int_{-\infty}^{\infty}\frac{d\omega}{2\pi}\int\frac{d^2\mathbf{k}}{(2\pi)^2}\frac{k_{\nu}k_{\nu}}{[\omega^2 + c^2k^2 + M_{\beta}^2/2][\omega^2 + c^2k^2 + M_{\gamma}^2/2]}, \tag{3.40}$$

with $\alpha \neq \beta \neq \gamma$. The previous one-loop mass correction, using Eq. (3.17) and after integrating over the angular variable, acquires the form

$$\begin{aligned} \Delta\mathcal{M}^2_{\alpha\nu} &\equiv \mu^2 - \mathcal{M}^2_{\alpha\nu} = 2\tilde{\kappa}(2\tilde{g}c\tilde{\lambda})^2\frac{1}{m_{\gamma}^2 - m_{\beta}^2}\int_0^{\infty}\frac{d\omega}{2\pi}\int_0^{k_F}\frac{dk\,k}{2\pi} \\ &\times k^2\left(\frac{1}{\omega^2 + c^2k^2 + M_{\beta}^2} - \frac{1}{\omega^2 + c^2k^2 + M_{\gamma}^2}\right). \end{aligned} \tag{3.41}$$

The integral over the Matsubara frequencies can be readily performed, yielding

$$\Delta\mathcal{M}^2_{\alpha\nu} = \tilde{\kappa}(\tilde{g}c\tilde{\lambda})^2\frac{1}{\pi(M_{\gamma}^2 - M_{\beta}^2)}\left[I(M_{\beta}) - I(M_{\gamma})\right], \tag{3.42}$$

with the function $I(M)$ defined as

$$I(M) = \int_0^{k_F} dk\, k \frac{k^2}{\sqrt{c^2k^2 + M^2}}. \tag{3.43}$$

Straightforward calculations yield the function $I(M)$,

$$I(M) = \frac{1}{3c^4}\left\{(c^2k_F^2 - 2M^2)\sqrt{c^2k_F^2 + M^2} + 2M^3\right\}. \tag{3.44}$$

Using Eqs. (3.42) and (3.44), we can now estimate the critical concentration, x_{AF}^{th} at which the instability towards the helicoidal phase takes place. In the case of the dipole mass $\mathcal{M}_{bb}$, Eq. (3.42) reads

$$\Delta\mathcal{M}_{bb}^2 = \tilde{\kappa}(\tilde{g}c\tilde{\lambda})^2 \frac{1}{\pi(M_c^2 - M_a^2)}\left[I(M_a) - I(M_c)\right], \tag{3.45}$$

with the function $I(M)$ given by Eq. (3.44). At the transition to the helicoidal phase, the DM gap vanishes, as we discussed in Sec. 3.3, and thus the previous mass equation acquires the form

$$\mu^2 = \tilde{\kappa}(\tilde{g}c\tilde{\lambda})^2 \frac{1}{\pi M_c^2}\left[I(0) - I(M_c)\right], \tag{3.46}$$

which, using Eq. (3.44), can be rewritten as

$$\mu^2 = \tilde{\kappa}\left(\frac{\tilde{g}\tilde{\lambda}}{c}\right)^2 \frac{M_c}{3\pi}\left(\frac{ck_F}{M_c}\right)^3 \left\{1 - \sqrt{1 + \left(\frac{M_c}{ck_F}\right)^2}\left[1 - 2\left(\frac{M_c}{ck_F}\right)^2\right] - 2\left(\frac{M_c}{ck_F}\right)^3\right\}. \tag{3.47}$$

In order to estimate the critical concentration, x_{AF}^{th}, we use the bare value for the XY mass at the critical point, $M_c \sim 5 \times 10^{-2}$, the spin-wave velocity $c = 2S\sqrt{2}$, and for lightly doped LSCO, $x \sim 0.01$, we have $ck_F/M_c \sim 5$, with $k_F = \sqrt{\pi x}$. Thus, in Eq. (3.47), we can consider M_c/ck_F as a small parameter, and expand the right-hand side of this equation in a power series of it, which yields

$$\mu^2 = \tilde{\kappa}\left(\frac{\tilde{g}\tilde{\lambda}}{c}\right)^2 \frac{ck_F}{2\pi}\left[1 + \mathcal{O}\left(\frac{M_c}{ck_F}\right)\right]. \tag{3.48}$$

Finally, the critical concentration is readily obtained from the previous equation,

$$x_{AF}^{th} = \pi\left(\frac{2\mu^2\rho_s^2}{c\tilde{\kappa}\tilde{\lambda}^2}\right)^2. \tag{3.49}$$

Using the known values for the parameters of the model, $\tilde{\kappa} \sim 1.1$, $\tilde{\lambda} \sim 1$, $\rho_s = c/\tilde{g} \sim S^2$, and $\mu \sim 1$ [79], we find $x_{AF}^{th} \sim 2.1\%$, in agreement with experiments. Moreover, this critical concentration is also consistent with the value obtained from the vanishing of the DM gap, indicating that our approach, in which we treat the coupled one-loop mass equations for the dipole and the magnon fields as being decoupled, captures the essential physics taking place in the system.

Chapter 4

Topological Defects in Frustrated Heisenberg Spin Systems

This chapter is based on the following publications: V. Juricic, L. Benfatto, A. O. Caldeira, and C. Morais Smith, Phys. Rev. Lett. **92**, 137202 (2004) and V. Juricic, L. Benfatto, A. O. Caldeira, and C. Morais Smith, Phys. Rev. B **71**, 064421 (2005).

In the previous chapter of this thesis, we showed that the Néel state is unstable towards the formation of a noncollinear helicoidal ground state described by Eq. (3.33). For describing the spin fluctuations around this noncollinear ground state, it is necessary to introduce a new, more complex, order parameter that takes into account the noncollinearity of the ground state, as we show below. The first step towards this goal is to count the number of degrees of freedom associated with the fluctuations around the new ground state. The form of the helicoidal state, given by Eq. (3.33) implies that the corresponding fluctuations are described by the vectors $\mathbf{n}_1 \sim (\sigma_a, 0, 0)$, $\mathbf{n}_2 \sim (0, 0, \sigma_c)$, and the vector $\mathbf{n}_3 \equiv \mathbf{n}_1 \times \mathbf{n}_2$, linearly independent of the previous two. Hence, there are three independent degrees of freedom associated with the spin fluctuations around the helicoidal ground state, described by a set of orthonormal vectors, $\mathbf{n}_k$, with $k = 1, 2, 3$, and $n_k^a n_q^a = \delta_{kq}$, which can also be viewed as elements of the rotational group in three dimensions, $SO(3)$. Thus, the order parameter space in the case of a noncollinear spin configuration is isomorphic to the group of rotations in the three-dimensional space. In this chapter, we will study the dynamics of topological defects that may be formed in the spin system described by the $SO(3)$ order parameter, and which

appear to be vortex-like. We consider the microscopic spin dynamics governed by the Heisenberg Hamiltonian, since we do not expect the DM (which vanishes at the onset of the spin-glass phase) and XY anisotropies to be relevant for the physics of the topological defects. The main role of these anisotropies, as we discussed in the previous chapter, is to determine the ground state properties in the spin-glass phase, which result from the competition of these anisotropic interactions with the frustration introduced by the doping. Although our study of the vortex dynamics has been motivated by a specific physical system, namely, the spin-glass phase of LSCO, the analysis performed in this chapter is valid for any two-dimensional frustrated Heisenberg spin system displaying a noncollinear ordered ground state.

4.1 Introduction

Two-dimensional frustrated Heisenberg spin systems with noncollinear or canted order have attracted much attention recently. Noncollinear order arises due to frustration, which may originate from different sources. The most common kind of frustration is realized in antiferromagnets on a two-dimensional (or three-dimensional stacked) triangular lattice. Prototypes of these geometrically frustrated magnets are pyrochlores [83, 84, 85]. A second source of frustration may be a competition between nearest-neighbor and further-neighbor exchange interactions between spins. Typical examples are helimagnets, where a magnetic spiral is formed along a certain direction of the lattice [83]. A third kind of frustration may occur by chemical doping of a magnetically ordered system. In this case, the spin-current of the itinerant doped charges couples to the local magnetic moment of the magnetic host, leading to the formation of a noncollinear magnetic state. This situation may be realized in lightly doped cuprate superconductors [71, 73, 86, 87, 88, 89, 90, 43, 44, 66].

The main characteristic of the noncollinear state is that the spin configuration must be described by a set of three orthonormal vectors or, alternatively, by a rotational matrix which defines the orientation of this set with respect to some fixed reference frame. As a consequence, the order-parameter space is isomorphic to the three-dimensional rotational group $SO(3)$, and in the low-temperature phase, when the rotational symmetry is fully broken, three spin-wave modes are present in the system, instead of two, as in the nonfrustrated case. Moreover, topological defects may arise in the system, associated with the chiral degeneracy of the spiral, which can rotate clockwise or counterclockwise. Because the order parameter space has a nontrivial first homotopy group, $\pi_1[SO(3)] = \mathbb{Z}_2$, the topological excitations are vortex-like. On the other hand, skyrmions are not present, because the second homotopy group of the $SO(3)$ is trivial, $\pi_2[SO(3)] = 0$ [91].

A convenient field-theoretical description of frustrated Heisenberg systems in the long-wavelength limit is provided by the $SO(3)$ nonlinear sigma (NLσ) model [91, 92, 42, 93, 94, 95, 96]. Its critical behavior in two dimensions has been

extensively investigated, both in the absence and in the presence of topological excitations. Studies in the former case have revealed a dynamical enhancement of the symmetry from $O(3) \otimes O(2)$ to $O(4)$ under renormalization group flow in $d = 2 + \epsilon$, which means that in the critical region all the three spin-wave modes have the same velocity [92, 95, 96]. When topological excitations are included, a complex finite-temperature behavior is found [97]. Numerical studies, as well as analysis involving entropy and free energy arguments, indicate the occurrence of a transition driven by vortex-antivortex pairs unbinding at a finite temperature T_v [98, 99, 100, 101]. In contrast to the XY case, here vortices and spin-waves are coupled already in the harmonic approximation, and anharmonic spin-wave interactions yield a finite correlation length for arbitrarily low temperatures [95, 96, 102]. Therefore, the transition mediated by vortices is rather a crossover than a true Kosterlitz-Thouless transition [103]. Free vortices start to proliferate at the temperature T_v, similarly as vortices in the XY model do above the Kosterlitz-Thouless transition temperature.

In this chapter, we study the physical properties of frustrated Heisenberg spin system, which are sensitive to the dynamics of the above-mentioned topological defects. The approach we use has been employed to describe the dynamics of excitations in a very broad class of one- or two-dimensional systems [104, 105, 106, 107, 108, 109]. The central idea is the application of the collective-coordinate method [110] to quantize a nontrivial static solution of the classical equation of motion of the field-theoretical model in question. In our case, we find that single vortex-like excitations or vortex-antivortex pairs are the localized static solution of the $SO(3)$ NLσ model. A proper description of the quantum levels associated with these solutions is provided, on the semiclassical level, by a theory in which the topological excitation is represented by a single quantum mechanical variable coupled to a bath of quantum harmonic oscillators, which are the fluctuations about the classical solution itself. Thus, the resulting effective model represents a particle (the topological defect) scattered by the linearized excitations of the system. The latter can be integrated out using the standard system-plus-reservoir approach [104, 105] leading to a dissipative equation of motion for the topological excitation. As a consequence, any physical property of these systems that depends on the motion of the topological excitations may be expressed in terms of transport coefficients - such as mobility and diffusion - of these damped defects. Since we do neglect any interaction between the defects, our results are only valid for a diluted gas of topological excitations.

This chapter is organized as follows. Starting from the $SO(3)$ NLσ model, we derive in Sec. 4.2 the quantum Hamiltonian describing the dynamics of the topological defect coupled to a bath of magnetic excitations. In Sec. 4.3 the equation governing the evolution of the reduced density matrix for the topological defect is obtained and the influence functional, which describes the effect of the magnon bath on the dynamics of the vortices, is evaluated. Section 4.4 is devoted to the

derivation of the effective action for the defect after the magnons have been integrated out, and in Sec. 4.5 the inverse mobility is calculated. In Sec. 4.6, we apply these results to the description of the transport properties in the spin-glass phase of LSCO.

4.2 The Model

In the spiral state the spin configuration $\mathbf{S}$ at each site $\mathbf{r}$ is described by means of a dreibein order parameter $n_k^a \in SO(3)$ with $k = 1, 2, 3$ and $n_k^a n_q^a = \delta_{kq}$ [92], so that

$$\frac{\mathbf{S}}{S} = \mathbf{n} = \mathbf{n}_1 \cos(\mathbf{k}_s \cdot \mathbf{r}) - \mathbf{n}_2 \sin(\mathbf{k}_s \cdot \mathbf{r}), \tag{4.1}$$

where $S = |\mathbf{S}|$ and the wave vector $\mathbf{k}_s = (\pi/a, \pi/a) + \mathbf{Q}$, with a denoting the lattice constant. Here, $\mathbf{Q} = (2\pi/m_x a, 2\pi/m_y a)$ measures the *incommensurate* spin correlations . Indeed, the magnetic structure factor corresponding to the spin modulation (4.1) has two peaks at $\mathbf{k}_s$ and $-\mathbf{k}_s$ (equivalent to $(\pi/a, \pi/a) - \mathbf{Q}$), as represented in Fig. 4.1 in the case of $m_x = -m_y$. The resulting spin order for $\mathbf{n}_1$ and $\mathbf{n}_2$ rotating within the CuO_2 plane is represented in Fig. 4.2, where $m_x = -m_y = 20$. Observe that the periodicity of the spin texture is $(m_x a, m_y a)$ for even values of m_x, m_y, and twice it for odd values.

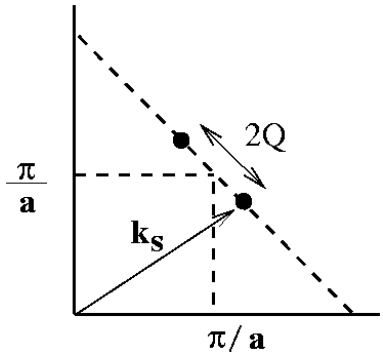

Figure 4.1: Incommensurate magnetic response for the spiral spin modulation (4.1). The magnetic structure factor corresponding to the spiral order with the wave vector $\mathbf{k}_s$ exhibits two peaks at the points $(\pi/a, \pi/a) \pm \mathbf{Q}$ marked by a circle in the figure. In this case $\mathbf{Q}$ has finite components in both the x and y directions, and the distance between the peaks is twice the modulus of $\mathbf{Q}$.

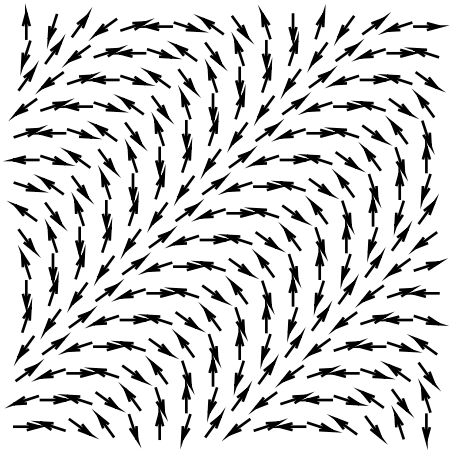

Figure 4.2: Spin background corresponding to Eq. (4.1) and to the case depicted in Fig. 4.1. Here a value of $\mathbf{Q} = (2\pi/20a, -2\pi/20a)$ has been chosen.

As discussed in Refs. [92, 42, 93, 94], a proper continuum field theory for the spiral state is provided by the $SO(3)$ quantum NLσ model,

$$\mathcal{S} = \int dt d^2\mathbf{x} [\varkappa_k (\partial_t \mathbf{n}_k)^2 - p_{k\alpha} (\partial_\alpha \mathbf{n}_k)^2]. \tag{4.2}$$

Here, the index α stands for the spatial coordinates and summation over repeated indices is understood. The spatial anisotropy of the spin stiffness $p_{k\alpha}$ depends on the components Q_α of the incommensurate wave vector. Since at the fixed point all the spin-wave velocities are equal [92, 95, 96], we will consider the case $\varkappa_k \equiv \varkappa$, $p_{k\alpha} \equiv p_\alpha$ and choose a system of coordinates parallel ($x_\parallel$) and perpendicular ($x_\perp$) to the spiral axis, respectively,

$$\mathcal{S} = \varkappa \int dt dx_\perp dx_\parallel [(\partial_t \mathbf{n}_k)^2 - c_\perp^2 (\partial_\perp \mathbf{n}_k)^2 - c_\parallel^2 (\partial_\parallel \mathbf{n}_k)^2], \tag{4.3}$$

where $c_\perp \equiv \sqrt{p_\perp/\varkappa}$ and $c_\parallel \equiv \sqrt{p_\parallel/\varkappa}$ are the spin wave velocities perpendicular and parallel to the spiral axis. Observe that, because of the isotropy of the spin stiffness in the spin space, the properties of the magnetic excitations do not depend on the plane in which the spins rotate in the magnetic ground state. Even though for the moment we will keep our derivation on general grounds, in the last section of this chapter we will specify the values of the parameters $\varkappa$ and c for the case of LSCO, and the results obtained in this section will be applied to the description of the transport properties in this compound.

Given the action (4.3) as our starting model, our first aim is to analyze whether the equations of motion admit topologically nontrivial solutions. For that purpose, it is convenient to introduce an equivalent representation of the n_k^a order parameter through an element $g \in SU(2)$ as

$$n_k^a = \frac{1}{2}\mathrm{Tr}[\sigma^a g \sigma^k g^{-1}], \tag{4.4}$$

where σ^a are Pauli matrices, and to introduce the fields

$$A_\mu^a = \frac{1}{2i}\mathrm{Tr}[\sigma^a g^{-1}\partial_\mu g], \tag{4.5}$$

which are related to the first derivatives of the order parameter through $\partial_\mu n_k^a = 2\epsilon_{ijk}A_\mu^i n_j^a$ [102]. Here, $\partial_\mu \equiv (\partial_t, \nabla)$ and $\epsilon_{123} = \epsilon^{123} = 1$. Using that $(\partial_\mu \mathbf{n})^2 = 8\mathbf{A}_\mu^2$ (no summation over index μ is imposed here), the action (4.3) reads

$$\mathcal{S} = 8\varkappa \int dt dx_\parallel dx_\perp \left(\mathbf{A}_0^2 - c_\perp^2 \mathbf{A}_\perp^2 - c_\parallel^2 \mathbf{A}_\parallel^2\right). \tag{4.6}$$

The above action may be mapped into an isotropic form by introducing the coordinates $\mathbf{r} = (x, y)$ with

$$x = \sqrt{\frac{c_\parallel}{c_\perp}}x_\perp, \qquad y = \sqrt{\frac{c_\perp}{c_\parallel}}x_\parallel.$$

We then find

$$\mathcal{S} = \mathcal{N}\int dt d^2\mathbf{r}\mathbf{A}_\mu^2 \equiv \mathcal{N}\int dt d^2\mathbf{r}\left(\mathbf{A}_0^2 - c^2\mathbf{A}_\alpha^2\right) \tag{4.7}$$

with the isotropic spin-wave velocity $c = \sqrt{c_\parallel c_\perp}$ and the constant $\mathcal{N} = 8\varkappa$. The most generic expression for the element g is given by

$$g[\boldsymbol{\alpha}] = \exp\left(\frac{i}{2}\boldsymbol{\alpha}(\mathbf{r}, t)\cdot\boldsymbol{\sigma}\right), \tag{4.8}$$

and the corresponding Lagrangian obtained from the action (4.7) reads

$$L_0 = \frac{1}{4}\mathcal{N}\int d^2\mathbf{r}(\partial_\mu\boldsymbol{\alpha})^2, \tag{4.9}$$

with $\partial_\mu A\partial_\mu B \equiv \partial_t A\partial_t B - c^2\nabla A\nabla B$. By making the ansatz [97] $\boldsymbol{\alpha}(\mathbf{r}, t) = \mathbf{m}\Psi(\mathbf{r}, t)$, where $\mathbf{m}$ is a constant unit vector and Ψ a scalar function, the Lagrangian (4.9) reduces to

$$L_0 = \frac{1}{4}\mathcal{N}\int d^2\mathbf{r}(\partial_\mu\Psi)^2. \tag{4.10}$$

The equation of motion for the field Ψ,

$$\partial_t^2 \Psi - c^2 \nabla^2 \Psi = 0, \tag{4.11}$$

possesses static topologically nontrivial solutions in the form of a single-vortex defect at $\mathbf{R} = (X, Y)$,

$$\Psi_{1v} = \arctan\left(\frac{x - X}{y - Y}\right), \tag{4.12}$$

and a vortex-antivortex pair

$$\begin{aligned} \Psi_{2v} &= \arctan\left(\frac{x - X_1}{y - Y_1}\right) - \arctan\left(\frac{x - X_2}{y - Y_2}\right) \\ &= \arctan\left\{\frac{[\mathbf{d} \times (\mathbf{r} - \mathbf{R})]_z}{[(\mathbf{r} - \mathbf{R})^2 - d^2/4]}\right\}, \end{aligned} \tag{4.13}$$

where now $\mathbf{R} = (\mathbf{R}_1 + \mathbf{R}_2)/2$ is the center of mass and $\mathbf{d} = \mathbf{R}_2 - \mathbf{R}_1$ the relative coordinate of the defect pair. If in Eqs. (4.12) and (4.13) the role of x and y coordinates is interchanged, one only changes the vorticity. Without loss of generality, we may assume the unity vector to be in the z-direction, $\mathbf{m} = \mathbf{e}_z$. Thus, the $\mathbf{n}_k$ fields which define the spin configuration according to Eq. (4.1), are given by $\mathbf{n}_1 = (\cos\Psi, -\sin\Psi, 0), \mathbf{n}_2 = (\sin\Psi, \cos\Psi, 0), \mathbf{n}_3 = (0, 0, 1)$. The spin patterns corresponding to a single vortex (Ψ_{1v} from Eq. (4.12)) or to a vortex-antivortex pair (Ψ_{2v} from Eq. (4.13)) are represented in Fig. 4.3 and Fig. 4.4, respectively.

The main difference between the two possible static solutions (4.12) and (4.13) is their energy. As shown in App. D, the energy of a single-vortex diverges with the logarithm of the system size ℓ, $E[\Psi_{1v}] \propto \ln \ell$. On the other hand, the vortex-antivortex pairs have finite energy, depending on the distance d between defects, $E[\Psi_{2v}] \propto \ln d$. A similar situation is realized in the standard XY model, where indeed the presence of single defects below the Kosterlitz-Thouless transition is not energetically favorable in the thermodynamic limit [103]. However, in the case of the model (4.3), which possesses asymptotic freedom, the correlation length ξ is finite at any finite temperature [95, 96, 102], so that the logarithmic divergence of the single-vortex energy should be understood up to the length scale ξ, $E[\Psi_{1v}] \propto \ln \xi$. In addition, the energy of the vortex-antivortex pair should be bounded below at distances of the order of few lattice spacings, which is the intrinsic cutoff of the theory. Because the procedure that we describe in the following does not depend on the exact form of the static solution, we will refer to a static topological defect solution Ψ_v specifying only at the end of the calculations the differences between the cases (4.12) and (4.13).

Following a procedure analogous to the one described in Ref. [110] to quantize the kink solution of the scalar field theory, we analyze now the effect of the fluctuations around the static topologically nontrivial configuration, which is a

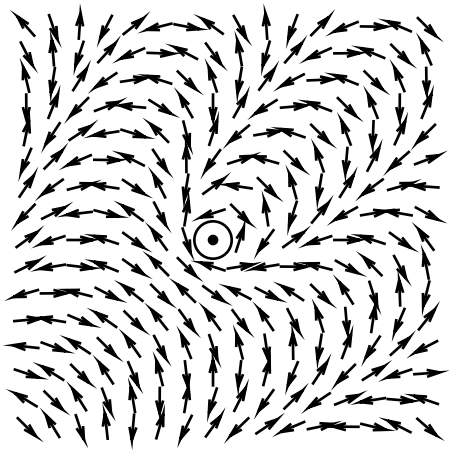

Figure 4.3: Spin background corresponding to the one-vortex solution of Eq. (4.12). The center of the vortex is marked by the circle. The spiral incommensurability $\mathbf{Q}$ is the same used in Fig. 4.2.

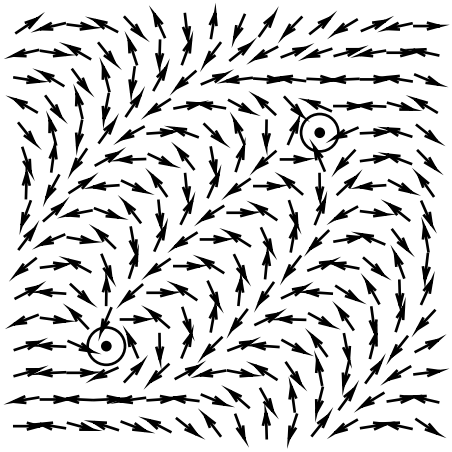

Figure 4.4: Spin background corresponding to the vortex-antivortex solution of Eq. (4.13). The centers of the vortices are marked by a circle. The spiral incommensurability $\mathbf{Q}$ is the same used in Fig. 4.2.

saddle point of the action that corresponds to the Lagrangian (4.10). In order to reach this aim, we write the generic field $g \in SU(2)$ of Eq. (4.8) in the form of a product of the field g_s corresponding to a static solution $\mathbf{m}\Psi_v(\mathbf{r})$ and the field g_ε

corresponding to the fluctuations around it,

$$g(\mathbf{r},t) = g_s\left[\Psi_v(\mathbf{r})\right] g_\varepsilon\left[\boldsymbol{\varepsilon}(\mathbf{r},t)\right], \tag{4.14}$$

where

$$g_\varepsilon[\boldsymbol{\varepsilon}] = \exp\left(\frac{i}{2}\boldsymbol{\varepsilon}\cdot\boldsymbol{\sigma}\right).$$

Observe that the description of the fluctuations via Eq. (4.14) differs from the standard approach used for a scalar field theory [110], and it is related to the symmetry properties of the order parameter. Indeed, since the full g has to be an element of the $SU(2)$ group, and both $g_s, g \in SU(2)$, then the fluctuations g_ε around g_s have to belong to $SU(2)$ as well. If instead, we had used the expansion $\boldsymbol{\alpha} = \mathbf{m}\Psi_v + \boldsymbol{\varepsilon}$, the equations of motion for the $\boldsymbol{\varepsilon}$ field would have been independent of the static solution Ψ_v, leading to a failure of the semiclassical expansion. Using Eqs. (4.5) and (4.14), we can express the action (4.7) in terms of the fields Ψ_v and $\boldsymbol{\varepsilon}$. Retaining only terms up to second order in $\boldsymbol{\varepsilon}$, we find (see App. E for details)

$$\begin{aligned} A_\mu^a &= \frac{1}{2}m^a\partial_\mu\Psi_v\left(1-\frac{\bar{\varepsilon}^2+\varepsilon_z^2}{2}\right)+\frac{1}{4}\varepsilon^a\varepsilon^b m^b\partial_\mu\Psi_v \\ &+ \frac{1}{2}\epsilon^{abc}\varepsilon^b m^c\partial_\mu\Psi_v+\frac{1}{2}\partial_\mu\varepsilon^a+\frac{1}{4}\epsilon^{abc}\varepsilon^b\partial_\mu\varepsilon^c, \end{aligned}$$

where $\bar{\varepsilon}^2 = \varepsilon_x^2 + \varepsilon_y^2$. The corresponding Lagrangian then reads (App. E)

$$L = L_0 + \mathcal{N}\int d^2\mathbf{r}\mathcal{L}_1 \tag{4.15}$$

with L_0 given by Eq. (4.10) and

$$\begin{aligned} \mathcal{L}_1[\Psi_v] &= \frac{1}{4}(\partial_\mu\boldsymbol{\varepsilon})^2+\frac{1}{2}(\mathbf{m}\cdot\partial_\mu\boldsymbol{\varepsilon})\partial_\mu\Psi_v \\ &+ \frac{1}{4}\epsilon^{abc}\partial_\mu\varepsilon^a\varepsilon^b m^c\partial_\mu\Psi_v = \\ &= \frac{1}{4}(\partial_\mu\bar{\varepsilon})^2+\frac{1}{4}\bar{\varepsilon}^2(\partial_\mu\theta)^2+\frac{1}{4}(\partial_\mu\varepsilon^z)^2 \\ &+ \frac{1}{2}\partial_\mu\varepsilon^z\partial_\mu\Psi_v-\frac{1}{4}\bar{\varepsilon}^2\partial_\mu\Psi_v\partial_\mu\theta. \end{aligned} \tag{4.16}$$

Here, we used the fact that $\mathbf{m} = \mathbf{e}_z$ and introduced polar coordinates $\boldsymbol{\varepsilon} = (\bar{\varepsilon}\cos\theta, \bar{\varepsilon}\sin\theta, \varepsilon_z)$. Since the Lagrangian $\mathcal{L}_1$ is evaluated at the vortex-like solution Ψ_v of Eq. (4.11), the equations of motion for the fluctuations around the topological defect also depend on Ψ_v

$$\bar{\varepsilon}: \quad (\partial_t^2 - c^2\nabla^2)\bar{\varepsilon} - \bar{\varepsilon}(\partial_\mu\theta)^2 - c^2\bar{\varepsilon}\nabla\Psi_v\nabla\theta = 0, \tag{4.17}$$

$$\theta: \qquad \partial_\mu(\bar{\varepsilon}^2\partial_\mu\theta) + \frac{c^2}{2}\nabla(\bar{\varepsilon}^2\nabla\Psi_v) = 0, \tag{4.18}$$

$$\varepsilon_z : \qquad (\partial_t^2 - c^2\nabla^2)\varepsilon^z = 0. \tag{4.19}$$

Eq. (4.18) admits the solution $\theta = \Psi_v/2$, whereas Eq. (4.19) indicates that the field ε_z is free. By using these two conditions, we can rewrite the total Lagrangian L in Eq. (4.15) as

$$L = \frac{\mathcal{N}}{4}\int d^2\mathbf{r}\left[(\partial_\mu\Psi_v)^2 + (\partial_\mu\bar{\varepsilon})^2 - \frac{1}{4}\bar{\varepsilon}^2(\partial_\mu\Psi_v)^2\right], \tag{4.20}$$

and the equation of motion (4.17) as

$$\left[\partial_t^2 - c^2\nabla^2 - \frac{1}{4}(\nabla\Psi_v)^2\right]\bar{\varepsilon} = 0.$$

Since the field Ψ_v in the previous equation does not depend on time, we decompose the field $\bar{\varepsilon}$ into its time- and space-dependent parts

$$\bar{\varepsilon}(\mathbf{r},t) = \sum_{nm} q_{nm}(t)\eta_{nm}(\mathbf{r}), \tag{4.21}$$

and identify the normal modes η_{nm} with the eigenfunctions of the operator

$$c^2\left[\nabla^2 + V(\mathbf{r})\right]\eta_{nm} = -\omega_{nm}^2\eta_{nm}. \tag{4.22}$$

This equation has the typical form of a Klein-Gordon-like equation for a particle scattered by a potential $V(\mathbf{r}) = (\nabla\Psi_v)^2/4$. The two indices n and m refer, respectively, to the radial and angular part of the wave function. By using a standard approach to scattering problems in two dimensions one may express the wave functions η_{nm} in terms of the eigenfunctions of the free problem ($V = 0$), corrected by a phase shift δ_m due to the scattering by the potential $V(\mathbf{r})$ [111],

$$\eta_{nm} = \frac{1}{2}\sqrt{\frac{k_{nm}}{2\ell}}e^{im\vartheta}\left[H_{|m|}^{(1)}(k_{nm}r) + e^{-2i\delta_m}H_{|m|}^{(2)}(k_{nm}r)\right]. \tag{4.23}$$

Here, $H_{|m|}^{(1,2)}$ are Hankel functions of the first and second kinds, m is an integer, and ϑ is a polar angle. The k_{nm} values are determined by requiring the vanishing of the wave function (4.23) at the boundary $r = \ell$. By using the asymptotic form of the Hankel functions, we obtain $k_{nm}\ell = (2n+1)\pi/2 + (2|m|+1)\pi/4 - \delta_m$, where n is a positive integer. Since the field $\bar{\varepsilon}$ is real, we may rewrite the expansion (4.21) in the form

$$\bar{\varepsilon}(\mathbf{r},t) = \sum_{n,m\geq 0}\left(q_{nm}(t)\eta_{nm}(\mathbf{r}) + q_{nm}^*(t)\eta_{nm}^*(\mathbf{r})\right), \tag{4.24}$$

where we used the identities $\eta_{n,m} = e^{-2i\delta_m}\eta_{n,-m}^*$ and $\delta_m = \delta_{-m}$. Note that the sum in Eq. (4.24) is over the positive angular momenta, as will be the case in what follows.

The static defect solution $\Psi_v(\mathbf{r})$ of Eq. (4.11) is invariant under translation of the center of the defect (i.e., the position of the vortex or the center of mass of the vortex-antivortex pair). A consequence of this invariance [110] is that Eq. (4.22) admits zero-frequency modes. A consistent treatment of them requires the use of the collective coordinate method [106, 107, 108, 109, 110]. The center of mass of the defect is then promoted to a dynamical variable, yielding

$$\Psi_v(\mathbf{r}) \to \Psi_v(\mathbf{r} - \mathbf{R}(t)), \tag{4.25}$$

and

$$\bar{\varepsilon}(\mathbf{r}, t) \to \bar{\varepsilon}(\mathbf{r} - \mathbf{R}(t), t) \equiv \sum_{nm} (q_{nm}(t)\eta_{nm}(\mathbf{r} - \mathbf{R}(t)) + C.c.), \tag{4.26}$$

where the last sum is over all nonzero-frequency modes. By inserting these expressions into the full Lagrangian (4.20) evaluated at the saddle-point solution we obtain

$$\begin{aligned} \frac{\mathcal{N}}{4} \int dt d^2\mathbf{r} (\partial_t \Psi_v)^2 &= \frac{\mathcal{N}}{4} \int dt d^2\mathbf{r} \dot{R}_\alpha \dot{R}_\beta \partial_\alpha \Psi_v \partial_\beta \Psi_v \\ &= \frac{M}{2} \int dt \dot{\mathbf{R}}^2(t), \end{aligned} \tag{4.27}$$

where

$$M = \frac{\mathcal{N}}{2} \int d^2\mathbf{r} (\nabla \Psi_v)^2$$

is the mass of the topological defect, which is proportional to its energy (see App. D). The time derivative of the field $\bar{\varepsilon}$ yields

$$\begin{aligned} &\frac{\mathcal{N}}{4} \int dt d^2\mathbf{r} (\partial_t \bar{\varepsilon})^2 = \frac{\mathcal{N}}{4} \sum_{nm,kl} \int dt d^2\mathbf{r} \, [\dot{q}^*_{nm}(t)\eta^*_{nm} \\ - \quad & q^*_{nm} \partial_\alpha \eta^*_{nm} \dot{R}_\alpha(t) + C.c.\Big] \Big[\dot{q}_{kl}(t)\eta_{kl} - q_{kl}\partial_\beta \eta_{kl} \dot{R}_\beta(t) \\ + \quad & C.c.] = \frac{\mathcal{N}}{2} \sum_{nm} \int dt \Bigg[|\dot{q}_{nm}|^2 + \sum_{kl} \dot{\mathbf{R}}(t) \left(\dot{q}_{nm} q^*_{kl} \mathbf{G}^*_{nm,kl} \right. \\ + \quad & \left. \dot{q}^*_{nm} q_{kl} \mathbf{G}_{nm,kl} \right)] , \end{aligned} \tag{4.28}$$

where the coupling constants $\mathbf{G}$ are related to the eigenfunctions η via

$$\mathbf{G}_{nm,kl} = \int d^2\mathbf{r} \eta_{kl} \nabla \eta^*_{nm},$$

and we neglected terms of order $q^2\dot{\mathbf{R}}^2$. Here, we used that $\int d^2\mathbf{r} \eta_{nm}\eta_{kl} = 0$ and $\int d^2\mathbf{r} \eta_{nm} \nabla \eta_{kl} = 0$, for m and l positive. By substituting Eqs. (4.27) and (4.28)

into the Lagrangian (4.20), we obtain

$$\begin{aligned} L &= \frac{1}{2}M\dot{\mathbf{R}}^2 + \sum_{nm}(|\dot{q}_{nm}|^2 - \omega_{nm}^2|q_{nm}|^2) \\ &+ \sum_{nm,kl}\dot{\mathbf{R}}(t)\left(\dot{q}_{nm}q_{kl}^*\mathbf{G}_{nm,kl}^* + \dot{q}_{nm}^*q_{kl}\mathbf{G}_{nm,kl}\right), \end{aligned}$$

where we rescaled $q \to q\sqrt{\mathcal{N}/2}$. Using that $\mathbf{G}_{nm,kl}^* = -\mathbf{G}_{kl,nm}$ and neglecting terms which are quadratic in $\mathbf{G}$, the corresponding Hamiltonian reads

$$H = \frac{1}{2M}(\mathbf{P} - \mathbf{P}_E)^2 + \sum_{nm}(|p_{nm}|^2 + \omega_{nm}^2|q_{nm}|^2), \tag{4.29}$$

with

$$\mathbf{P}_E = \sum_{nm,kl}\left(p_{nm}\mathbf{G}_{nm,kl}q_{kl} + p_{nm}^*\mathbf{G}_{nm,kl}^*q_{kl}^*\right).$$

Here, $\mathbf{P}$ is the momentum canonically conjugate to the center of the defect $\mathbf{R}$, and q_{nm} and p_{nm} are the coordinates and momenta of the magnons. The classical Hamiltonian (4.29) can be promptly quantized by introducing two sets of independent creation and annihilation operators, $\hat{a}^\dagger$, $\hat{a}$, and $\hat{b}^\dagger$, $\hat{b}$. The quantum Hamiltonian then reads

$$\hat{H} = \hat{H}_v + \hat{H}_B + \hat{H}_I, \tag{4.30}$$

where

$$\hat{H}_v = \frac{\hat{\mathbf{P}}^2}{2M} \tag{4.31}$$

is the Hamiltonian of a free defect, and

$$\hat{H}_B = \sum_{nm}\hbar\omega_{nm}(\hat{a}_{nm}^\dagger\hat{a}_{nm} + \hat{b}_{nm}^\dagger\hat{b}_{nm}) \tag{4.32}$$

is the Hamiltonian of the bath of magnons which consists of two independent sets of noninteracting harmonic oscillators described by the operators $\hat{a}$, $\hat{a}^\dagger$ and $\hat{b}$, $\hat{b}^\dagger$, as it is expected in two dimensions. The interaction between the bath and the topological defect is described by the Hamiltonian

$$\begin{aligned} \hat{H}_I &= -\frac{\hbar\hat{\mathbf{P}}}{M}\sum_{nm,kl}\Big[\mathbf{D}_{nm,kl}\hat{a}_{nm}\hat{a}_{kl}^\dagger - \mathbf{D}_{kl,nm}\hat{b}_{nm}\hat{b}_{kl}^\dagger \\ &+ \mathbf{C}_{nm,kl}(\hat{a}_{nm}^\dagger\hat{b}_{kl}^\dagger - \hat{a}_{kl}\hat{b}_{nm})\Big] \end{aligned} \tag{4.33}$$

with the coupling constants given by

$$\begin{aligned}\mathbf{D}_{nm,kl} &= \frac{i}{2}\frac{\omega_{nm}+\omega_{kl}}{\sqrt{\omega_{nm}\omega_{kl}}}\mathbf{G}_{kl,nm} \\ \mathbf{C}_{nm,kl} &= \frac{i}{2}\frac{\omega_{nm}-\omega_{kl}}{\sqrt{\omega_{nm}\omega_{kl}}}\mathbf{G}_{nm,kl}.\end{aligned} \tag{4.34}$$

The terms with the coupling constants $\mathbf{D}/\mathbf{C}$ describe the scattering/creation (annihilation) of magnetic excitations by the defect. Since we consider here only the low-energy dynamics of the topological defect, we neglect the off-diagonal terms in the interaction Hamiltonian, i.e., we set $\mathbf{C} = 0$. In the following we will integrate out the bath degrees of freedom in order to study the effective dynamics of the defects. For that purpose we employ the Feynman-Vernon formalism [112].

4.3 Reduced Density Matrix

In this section we derive the reduced density matrix for the defect. The system under consideration consists of two subsystems: the topological defect and the bath of magnons. Thus, the Hilbert space of the full system, $\mathcal{H}$, is a direct product of the subsystem Hilbert spaces $\mathcal{H} = \mathcal{H}_v \otimes \mathcal{H}_B \equiv \mathcal{H}_v \otimes \mathcal{H}_B^{(a)} \otimes \mathcal{H}_B^{(b)}$, and the state of the full system is also a direct product, $|\mathbf{x}, \boldsymbol{\alpha}\rangle \equiv |\mathbf{x}\rangle \otimes |\boldsymbol{\alpha}\rangle \equiv |\mathbf{x}\rangle \otimes |\boldsymbol{\alpha}_a\rangle \otimes |\boldsymbol{\alpha}_b\rangle$. We use the coordinate representation for the defect ($\mathbf{x}$ are the eigenvalues of its center-of-mass position operator), and the coherent state representation for the bath, $\hat{a}_{nm}|\boldsymbol{\alpha}_a\rangle = \alpha_{nm,a}|\boldsymbol{\alpha}_a\rangle$ and $\hat{b}_{nm}|\boldsymbol{\alpha}_b\rangle = \alpha_{nm,b}|\boldsymbol{\alpha}_b\rangle$. The reduced density matrix is defined as $\hat{\tilde{\rho}}_v(t) = \mathrm{Tr}_B[\hat{\rho}(t)]$, where Tr_B denotes the trace over the bath degrees of freedom, and $\hat{\rho}(t)$ is the density matrix of the full system, whose evolution is described by

$$\hat{\rho}(t) = e^{-\frac{i\hat{H}t}{\hbar}}\hat{\rho}(0)e^{\frac{i\hat{H}t}{\hbar}}. \tag{4.35}$$

Here, $\hat{H}$ is the Hamiltonian of the full system given by Eqs. (4.30)-(4.34). The matrix elements of the density operator in the basis introduced before are

$$\hat{\rho}(\mathbf{x}, \boldsymbol{\alpha}; \mathbf{y}, \boldsymbol{\beta}; t) = \langle \mathbf{x}, \boldsymbol{\alpha}|\hat{\rho}(t)|\mathbf{y}, \boldsymbol{\beta}\rangle,$$

and the reduced density matrix of the vortex reads

$$\begin{aligned}\hat{\tilde{\rho}}_v(\mathbf{x}, \mathbf{y}, t) &= \int \frac{d^2\boldsymbol{\alpha}}{\pi^{2N}}\langle \mathbf{x}, \boldsymbol{\alpha}|\hat{\rho}(t)|\mathbf{y}, \boldsymbol{\alpha}\rangle \\ &= \int \frac{d^2\boldsymbol{\alpha}}{\pi^{2N}}\langle \mathbf{x}, \boldsymbol{\alpha}|e^{-\frac{i\hat{H}t}{\hbar}}\hat{\rho}(0)e^{\frac{i\hat{H}t}{\hbar}}|\mathbf{y}, \boldsymbol{\alpha}\rangle.\end{aligned} \tag{4.36}$$

After insertion of the unity operator on both sides of $\hat{\rho}(0)$ in Eq. (4.36), the reduced density matrix acquires the form

$$\hat{\tilde{\rho}}_v = \int \frac{d^2\boldsymbol{\alpha}}{\pi^{2N}} \int d^2\mathbf{x}' \int d^2\mathbf{y}' \int \frac{d^2\boldsymbol{\beta}}{\pi^{2N}} \int \frac{d^2\boldsymbol{\beta}'}{\pi^{2N}} \langle \mathbf{x}, \boldsymbol{\alpha}| e^{-\frac{i\hat{H}t}{\hbar}} |\mathbf{x}', \boldsymbol{\beta}\rangle \langle \mathbf{x}', \boldsymbol{\beta}|\hat{\rho}(0)|\mathbf{y}', \boldsymbol{\beta}'\rangle \langle \mathbf{y}', \boldsymbol{\beta}'| e^{\frac{i\hat{H}t}{\hbar}} |\mathbf{y}, \boldsymbol{\alpha}\rangle. \tag{4.37}$$

In order to calculate the time evolution of the reduced density matrix, we have to define the initial condition for the density matrix of the full system. For the sake of simplicity, we choose the factorizable one

$$\hat{\rho}(0) = \hat{\tilde{\rho}}_v(0)\hat{\tilde{\rho}}_B(0), \tag{4.38}$$

which implies that the bath and the topological defect are decoupled at $t = 0$. The bath is assumed to be initially in thermal equilibrium at temperature T,

$$\hat{\tilde{\rho}}_B = \frac{e^{-U\hat{H}_B}}{\mathrm{Tr}[e^{-U\hat{H}_B}]} = \hat{\tilde{\rho}}_{B,a}\hat{\tilde{\rho}}_{B,b}, \tag{4.39}$$

where $U \equiv \hbar/(k_B T)$. Here, we used the fact that the baths do not interact, so the density matrix of the full bath is the product of the density matrices for the separate baths. By substituting Eqs. (4.38) and (4.39) into Eq. (4.37), we obtain

$$\hat{\tilde{\rho}}_v(\mathbf{x}, \mathbf{y}, t) = \int d^2\mathbf{x}' \int d^2\mathbf{y}' J(\mathbf{x}, \mathbf{y}, t; \mathbf{x}', \mathbf{y}', 0)\hat{\tilde{\rho}}_v(\mathbf{x}', \mathbf{y}', 0), \tag{4.40}$$

with the superpropagator J given by

$$\begin{aligned} J(\mathbf{x}, \mathbf{y}, t; \mathbf{x}', \mathbf{y}', 0) \quad = \quad & \int \frac{d^2\boldsymbol{\alpha}}{\pi^{2N}} \int \frac{d^2\boldsymbol{\beta}}{\pi^{2N}} \int \frac{d^2\boldsymbol{\beta}'}{\pi^{2N}} \hat{\tilde{\rho}}_B(\boldsymbol{\beta}^*, \boldsymbol{\beta}', 0) \\ & K(\mathbf{x}, \boldsymbol{\alpha}^*; \mathbf{x}', \boldsymbol{\beta}; t) K^*(\mathbf{y}, \boldsymbol{\alpha}^*; \mathbf{y}', \boldsymbol{\beta}'; t). \end{aligned} \tag{4.41}$$

4.3.1 The Superpropagator

We consider the superpropagator (4.41). The kernel

$$K(\mathbf{x}, \boldsymbol{\alpha}^*; \mathbf{y}, \boldsymbol{\beta}; t) \equiv \langle \mathbf{x}, \boldsymbol{\alpha}| e^{-\frac{i\hat{H}t}{\hbar}} |\mathbf{y}, \boldsymbol{\beta}\rangle, \tag{4.42}$$

can be expressed in the path-integral formalism as (App. F)

$$\begin{aligned} & K(\mathbf{x}, \boldsymbol{\alpha}^*; \mathbf{y}, \boldsymbol{\beta}; t) = \int_{\mathbf{y}}^{\mathbf{x}} \mathcal{D}\mathbf{x} \exp\left\{ -\frac{|\boldsymbol{\alpha}|^2}{2} - \frac{|\boldsymbol{\beta}|^2}{2} \right\} \\ \times \quad & \int_{\boldsymbol{\beta}}^{\boldsymbol{\alpha}^*} \mathcal{D}\boldsymbol{\zeta} \exp\left\{ \frac{1}{2}[\boldsymbol{\zeta}^*(0) \cdot \boldsymbol{\beta} + \boldsymbol{\zeta}(t) \cdot \boldsymbol{\alpha}^*] \right\} \exp\left\{ \frac{i}{\hbar} S_0[\mathbf{x}] \right\} \\ \times \quad & \exp\left\{ S_I[\mathbf{x}, \boldsymbol{\zeta}] \right\}, \end{aligned} \tag{4.43}$$

where $S_0[\mathbf{x}] = \int_0^t dt'(M/2)\dot{\mathbf{x}}^2$ stands for the free action and

$$\begin{aligned} S_I[\mathbf{x},\boldsymbol{\zeta}] &= \int_0^t dt' \left\{ \frac{1}{2}(\boldsymbol{\zeta}\cdot\dot{\boldsymbol{\zeta}}^* - \boldsymbol{\zeta}^*\cdot\dot{\boldsymbol{\zeta}}) - \frac{i}{\hbar}\left[h_B(\boldsymbol{\zeta}^*,\boldsymbol{\zeta}) - \dot{\mathbf{x}}\cdot\mathbf{h}_I(\boldsymbol{\zeta}^*,\boldsymbol{\zeta})\right]\right\} \\ &\equiv S_{I,a}[\mathbf{x},\boldsymbol{\zeta}_a] + S_{I,b}[\mathbf{x},\boldsymbol{\zeta}_b] \end{aligned} \tag{4.44}$$

denotes the interaction. Here

$$\begin{aligned} h_B &= \sum_{nm,i=a,b} \hbar\omega_{nm}\zeta^*_{nm,i}\zeta_{nm,i} \equiv h_{B,a} + h_{B,b}, \\ \mathbf{h}_I &= \hbar\sum_{nm,kl} \mathbf{D}_{nm,kl}\zeta^*_{kl,a}\zeta_{nm,a} - \mathbf{D}_{kl,nm}\zeta_{nm,b}\zeta^*_{kl,b} \equiv \mathbf{h}_{I,a} + \mathbf{h}_{I,b}. \end{aligned}$$

By inserting Eq. (4.43) into Eq. (4.41) and using the reduced density matrix of the bath in the coherent state representation (App. G), we obtain a simpler expression for the superpropagator,

$$J(\mathbf{x},\mathbf{y},t;\mathbf{x}',\mathbf{y}',0) = \int_{\mathbf{x}'}^{\mathbf{x}} \mathcal{D}\mathbf{x}\int_{\mathbf{y}'}^{\mathbf{y}} \mathcal{D}\mathbf{y}\, e^{\frac{i}{\hbar}[S_0(\mathbf{x})-S_0(\mathbf{y})]}\mathcal{F}[\mathbf{x},\mathbf{y}], \tag{4.45}$$

where $\mathcal{F} = \mathcal{F}_a\mathcal{F}_b$ is the total influence functional, and $\mathcal{F}_i$ $(i = a, b)$ is the influence functional for the bath i given by (to simplify notation we omit the index i in the integration variables)

$$\begin{aligned} \mathcal{F}_i[\mathbf{x},\mathbf{y}] &= \int \frac{d^2\boldsymbol{\alpha}}{\pi^N}\int\frac{d^2\boldsymbol{\beta}}{\pi^N}\int\frac{d^2\boldsymbol{\beta}'}{\pi^N}\rho_B(\boldsymbol{\beta}^*,\boldsymbol{\beta}',0)\exp\left\{-|\boldsymbol{\alpha}|^2 - \frac{|\boldsymbol{\beta}|^2}{2} - \frac{|\boldsymbol{\beta}'|^2}{2}\right\} \\ \times &\int_{\boldsymbol{\beta}}^{\boldsymbol{\alpha}^*}\mathcal{D}\boldsymbol{\zeta}\int_{\boldsymbol{\beta}'^*}^{\boldsymbol{\alpha}}\mathcal{D}\boldsymbol{\gamma}\exp\left\{\frac{1}{2}\left[\boldsymbol{\zeta}^*(0)\cdot\boldsymbol{\beta} + \boldsymbol{\zeta}(t)\cdot\boldsymbol{\alpha}^* + \boldsymbol{\gamma}(0)\cdot\boldsymbol{\beta}'^* + \boldsymbol{\gamma}^*(t)\cdot\boldsymbol{\alpha}\right]\right\} \\ \times &\exp\left\{S_{I,i}[\mathbf{x},\boldsymbol{\zeta}] + S^*_{I,i}[\mathbf{y},\boldsymbol{\gamma}]\right\}, \end{aligned} \tag{4.46}$$

with the initial conditions

$$\boldsymbol{\zeta}(0) = \boldsymbol{\beta}, \qquad \boldsymbol{\zeta}^*(t) = \boldsymbol{\alpha}^*, \tag{4.47}$$

$$\boldsymbol{\gamma}^*(0) = \boldsymbol{\beta}'^* \qquad \boldsymbol{\gamma}(t) = \boldsymbol{\alpha}. \tag{4.48}$$

4.3.2 Influence Functional

We now evaluate the influence functional, which describes the influence of the bath on the effective dynamics of the defect. The only difference between the functionals $\mathcal{F}_a$ and $\mathcal{F}_b$ is in the form of the interaction S_I; see Eqs. (4.44) and (4.46). Note that the actions $S_{I,a}$ and $S_{I,b}$ are related by the substitution $\mathbf{D}_{nm,kl} \to -\mathbf{D}_{kl,nm}$. Thus, it is enough to calculate the functional $\mathcal{F}_a$, and consequently $\mathcal{F}_b$ is obtained using the latter transformation. In order to simplify notation, in what follows

we write the integration variables without the index a. First, we calculate the path-integrals in Eq. (4.46) using the stationary phase approximation (SPA). In order to apply the SPA, we have to solve the equations of motion corresponding to S_I and S_I^*. Because $S_I^*(\mathbf{x},\boldsymbol{\zeta}) = -S_I(\mathbf{x},\boldsymbol{\zeta})$, we need to consider only S_I. The equations of motion are promptly obtained from $\delta S_I/\delta\zeta^*_{nm} = 0$, $\delta S_I/\delta\zeta_{nm} = 0$, and they read

$$\dot{\zeta}_{nm} + i\omega_{nm}\zeta_{nm} - i\dot{\mathbf{x}}\cdot\sum_{kl}\mathbf{D}_{kl,nm}\zeta_{kl} = 0, \quad \dot{\zeta}^*_{nm} - i\omega_{nm}\zeta^*_{nm} + i\dot{\mathbf{x}}\cdot\sum_{kl}\mathbf{D}_{nm,kl}\zeta^*_{kl} = 0. \tag{4.49}$$

Notice that the two equations are identical; one is the complex conjugate of the other (recall that $\mathbf{D}_{nm,kl} = \mathbf{D}^*_{kl,nm}$).

The SPA requires the evaluation of the action S_I on the classical trajectory, which is the solution of the above equations of motion. Straightforward calculations show that the value of S_I at the stationary point is zero. If we define $\boldsymbol{\zeta} = \boldsymbol{\zeta}_{cl} + \boldsymbol{\Delta}$, then the functional integral over $\boldsymbol{\zeta}$ becomes the functional integral over the fluctuations $\boldsymbol{\Delta}$ around the saddle point. Expanding the action around its saddle point, we find that the relevant contribution comes from the second derivative of the action at the stationary point, because both the value and the first derivative of the action are zero at the saddle point. The second derivative of the action evaluated at the stationary point is a constant operator, so the integration over the fluctuations $\boldsymbol{\Delta}$ yields, up to an irrelevant constant,

$$\begin{aligned}\mathcal{F}_a[\mathbf{x},\mathbf{y}] &= \int\frac{d^2\boldsymbol{\alpha}}{\pi^N}\int\frac{d^2\boldsymbol{\beta}}{\pi^N}\int\frac{d^2\boldsymbol{\beta}'}{\pi^N}\rho_{B,a}(\boldsymbol{\beta}^*,\boldsymbol{\beta}')e^{-|\boldsymbol{\alpha}|^2-\frac{|\boldsymbol{\beta}|^2}{2}-\frac{|\boldsymbol{\beta}'|^2}{2}} \\ &\times \exp\left\{\frac{1}{2}\left[\boldsymbol{\zeta}^*(0)\cdot\boldsymbol{\beta}+\boldsymbol{\zeta}(t)\cdot\boldsymbol{\alpha}^*+\boldsymbol{\gamma}(0)\cdot\boldsymbol{\beta}'^*+\boldsymbol{\gamma}^*(t)\cdot\boldsymbol{\alpha}\right]\right\}. \end{aligned}\tag{4.50}$$

Therefore, in the SPA, S_I and S_I^* only contribute to the influence functional through the boundary terms, which may be determined using the solutions of the equations of motion (see App. H for details).

After inserting Eqs. (G.2) and (H.8) into Eq. (4.50), and performing the Gaussian integrals over $\boldsymbol{\alpha},\boldsymbol{\beta}$ and $\boldsymbol{\beta}'$, the influence functional acquires the form

$$\mathcal{F}_a[\mathbf{x},\mathbf{y}] = \frac{1}{\det(1-\bar{n}\Gamma^a)}, \tag{4.51}$$

where the matrix Γ^a is given by

$$\begin{aligned}\Gamma^a_{nm,kl}[\mathbf{x},\mathbf{y}] &= \frac{1}{2}[W_{kl,nm}(\mathbf{x},t) + \tilde{W}_{nm,kl}(\mathbf{x},0) + \bar{W}_{kl,nm}(\mathbf{y},0) + \tilde{\bar{W}}_{nm,kl}(\mathbf{y},t)] \\ &+ \frac{1}{4}\sum_{pq}[\tilde{W}_{nm,kl}(\mathbf{x},0) + W_{pq,nm}(\mathbf{x},t)][\bar{W}_{kl,pq}(\mathbf{y},0) + \tilde{\bar{W}}_{pq,kl}(\mathbf{y},t)], \end{aligned}\tag{4.52}$$

and $\bar{n}_{pq} = 1/[\exp(U\omega_{pq}) - 1]$ is the bosonic occupation number. Equation (H.7) enables us to express the matrix Γ^a only in terms of the functionals W and $\tilde{W}$

$$\Gamma^a_{nm,kl}[\mathbf{x},\mathbf{y}] = \frac{1}{2}[W_{kl,nm}(\mathbf{x},t) + \tilde{W}_{nm,kl}(\mathbf{x},0) + \tilde{W}^*_{kl,nm}(\mathbf{y},0) + W^*_{nm,kl}(\mathbf{y},t)]$$
$$+ \quad \frac{1}{4}\sum_{pq}[\tilde{W}_{nm,pq}(\mathbf{x},0) + W_{pq,nm}(\mathbf{x},t)][\tilde{W}^*_{kl,pq}(\mathbf{y},0) + W^*_{pq,kl}(\mathbf{y},t)]. \tag{4.53}$$

Using the formula $\ln\det\mathcal{A} = \mathrm{Tr}\ln\mathcal{A}$ for the matrix $\mathcal{A} = (1 - \bar{n}\Gamma^a)^{-1}$, we find

$$\mathcal{F}_a[\mathbf{x},\mathbf{y}] = \exp[\mathrm{Tr}(\bar{n}\Gamma^a)] = \exp\left[\sum_{pq}\bar{n}_{pq}\Gamma^a_{pq,pq}\right], \tag{4.54}$$

and the total influence functional reads

$$\mathcal{F} = \mathcal{F}_a\mathcal{F}_b = \exp\left[\sum_{pq}\bar{n}_{pq}\Gamma_{pq,pq}\right] \tag{4.55}$$

in the lowest order in $\bar{n}\Gamma$, where $\Gamma \equiv \Gamma^a + \Gamma^b$. The diagonal elements of the matrix Γ^a are obtained from Eq. (4.53), while the matrix Γ^b is obtained from Γ^a by the substitution $\mathbf{D}_{nm,kl} \to -\mathbf{D}_{kl,nm} = -\mathbf{D}^*_{nm,kl}$. The functionals W and $\tilde{W}$ are given implicitly by Eqs. (H.3). From their form we see that they actually represent the amplitude of scattering of the mode nm to the mode kl through virtual intermediate states. These functionals can be determined iteratively from these equations up to any order. Here, we study the motion of a vortex with small kinetic energy; therefore the Born approximation will be enough for our purpose. The functionals W and $\tilde{W}$ are calculated within the Born approximation in App. H. Using Eq. (H.4) the diagonal elements of the matrix Γ can be promptly evaluated (App. I), and the total influence functional reads

$$\mathcal{F}[\mathbf{x},\mathbf{y}] = \exp[\frac{i}{\hbar}\Phi]\exp[\tilde{\Phi}], \tag{4.56}$$

where

$$\Phi = \sum_{\mu,\nu=1}^{2}\int_0^t dt'\int_0^t dt''\theta(t'-t'')\epsilon^{\mu\nu}(t'-t'')[\dot{x}^\mu(t') - \dot{y}^\mu(t')][\dot{x}^\nu(t'') + \dot{y}^\nu(t'')], \tag{4.57}$$

$$\tilde{\Phi} = \sum_{\mu\nu}\int_0^t dt'\int_0^t dt''\theta(t'-t'')\tilde{\epsilon}^{\mu\nu}(t'-t'')[\dot{x}^\mu(t') - \dot{y}^\mu(t')][\dot{x}^\nu(t'') - \dot{y}^\nu(t'')]$$

with

$$\epsilon^{\mu\nu}(t) \;=\; -\hbar\sum_{\mu,\nu}\sum_{nm,kl}\bar{n}_{nm}\left(D^{\mu*}_{nm,kl}D^{\nu}_{nm,kl} + D^{\mu}_{nm,kl}D^{\nu*}_{nm,kl}\right)$$
$$\times \quad \sin(\omega_{nm} - \omega_{kl})t, \tag{4.58}$$

$$\tilde{\epsilon}^{\mu\nu}(t) = -\sum_{\mu,\nu}\sum_{nm,kl} \bar{n}_{nm}\left(D^{\mu *}_{nm,kl}D^{\nu}_{nm,kl} + D^{\mu}_{nm,kl}D^{\nu *}_{nm,kl}\right)\cos(\omega_{nm}-\omega_{kl})t.$$

From Eqs. (4.45) and (4.56) we see that the oscillatory part $\exp[i\Phi/\hbar]$ gives a contribution to the effective action of the defect due to its scattering by the magnons and leads to its dissipative motion, as we show in the following section. The decaying part $\exp[\tilde{\Phi}]$ is related to the diffusive properties of the vortex. The diffusive and damping properties of the defect are related at low temperatures by the fluctuation-dissipation theorem.

4.4 The dynamics of the defect

4.4.1 Transport properties of the defect

In this section we will study the effective dynamics of the defect after integrating out the magnons. According to Eqs. (4.45) and (4.56), the effective action describing the influence of magnons on the motion of the topological defect reads

$$S_{eff} = S_0[\mathbf{x}] - S_0[\mathbf{y}] + \Phi[\mathbf{x},\mathbf{y}], \tag{4.59}$$

where Φ is given by Eq. (4.57). Since $\Phi \propto \mathbf{D}$, we observe that if the coupling constants $\mathbf{D}$ were zero, then the motion of the defect would be free. The equations of motion for the defect can be directly obtained by extremizing the effective action (4.59), $\delta S_{eff}/\delta x^{\mu} = 0$ and $\delta S_{eff}/\delta y^{\mu} = 0$. In terms of the center of mass $\mathbf{v} = (\mathbf{x}+\mathbf{y})/2$ and relative $\mathbf{u} = \mathbf{x}-\mathbf{y}$ coordinates, they read

$$\begin{aligned}
&\ddot{v}^{\mu}(\tau) + \sum_{\nu}\int_0^{\tau} dt' \gamma^{\mu\nu}(\tau - t')\dot{v}^{\nu}(t') = 0,\\
&\ddot{u}^{\mu}(\tau) + \sum_{\nu}\int_{\tau}^{t} dt' \gamma^{\mu\nu}(t' - \tau)\dot{u}^{\nu}(t') = 0.
\end{aligned} \tag{4.60}$$

As a consequence, the damping matrix $\gamma^{\mu\nu}$ is given by

$$\begin{aligned}
\gamma^{\mu\nu}(t) &\equiv \frac{2}{M}\frac{d}{dt}\epsilon^{\mu\nu}(t) = -\frac{\hbar}{M}\sum_{nm,pl}(\bar{n}_{nm}-\bar{n}_{pl})(\omega_{nm}-\omega_{pl}) \\
&\times \left(D^{\mu *}_{nm,pl}D^{\nu}_{nm,pl} + D^{\mu}_{nm,pl}D^{\nu *}_{nm,pl}\right)\cos(\omega_{nm}-\omega_{pl})t \\
&= -\frac{\hbar}{4M}\sum_{nm,pl}(\bar{n}_{nm}-\bar{n}_{pl})\frac{(\omega_{nm}-\omega_{pl})(\omega_{nm}+\omega_{pl})^2}{\omega_{nm}\omega_{pl}} \\
&\times \left(G^{\mu *}_{nm,pl}G^{\nu}_{nm,pl} + G^{\mu}_{nm,pl}G^{\nu *}_{nm,pl}\right)\cos(\omega_{nm}-\omega_{pl})t \\
&= -\frac{\hbar}{2M}\sum_{nm,pl}(\bar{n}_{nm}-\bar{n}_{pl})\frac{(\omega_{nm}-\omega_{pl})(\omega_{nm}+\omega_{pl})^2}{\omega_{nm}\omega_{pl}} \\
&\times G^{\mu *}_{nm,pl}G^{\nu}_{nm,pl}\cos(\omega_{nm}-\omega_{pl})t, \qquad (4.61)
\end{aligned}$$

where $\epsilon^{\mu\nu}$ is defined in Eq. (4.58). Introducing the scattering matrix

$$S^{\mu\nu}(\omega,\omega') = \sum_{nm,pl} G^{\mu *}_{nm,pl}G^{\nu}_{nm,pl}\delta(\omega-\omega_{nm})\delta(\omega'-\omega_{pl}), \qquad (4.62)$$

and observing that because of the isotropy of the model the damping matrix is diagonal (see also Eq. (4.72) below), $\gamma^{\mu\nu}(t) = \gamma(t)\delta^{\mu\nu}$, the damping function $\gamma(t)$ is given by

$$\gamma(t) = -\frac{\hbar}{2M}\int_0^\infty d\omega \int_0^\infty d\omega'[\bar{n}(\omega)-\bar{n}(\omega')]\frac{(\omega-\omega')(\omega+\omega')^2}{\omega\omega'}S(\omega,\omega')\cos(\omega-\omega')t. \qquad (4.63)$$

Let us introduce the new variables $\xi = (\omega+\omega')/2$, $\psi = \omega-\omega'$. The damping function can be then rewritten as

$$\gamma(t) = \int_{-\infty}^{\infty} d\psi \mathcal{J}(\psi)\cos\psi t, \qquad (4.64)$$

where $\mathcal{J}(\psi)$ is the spectral function of the bath [104, 105] given by an additional integration

$$\mathcal{J}(\psi) = -\frac{2\hbar}{M}\int_0^\infty d\xi \left[\bar{n}\left(\xi+\frac{\psi}{2}\right) - \bar{n}\left(\xi-\frac{\psi}{2}\right)\right]\frac{\xi^2\psi}{\xi^2-\psi^2/4}S\left(\xi+\frac{\psi}{2},\xi-\frac{\psi}{2}\right). \qquad (4.65)$$

From the equations of motion (4.60) it can be readily concluded that if a charge q is associated with the defect (see next section), the corresponding optical conductivity is

$$\sigma(\omega) = \left.\frac{nq^2/M}{z+\hat{\gamma}(z)}\right|_{z\to -i\omega+0^+}, \qquad (4.66)$$

where n is the density of carriers and $\hat{\gamma}(z)$ is the Laplace transformation of the damping function

$$\hat{\gamma}(z) = \int_0^\infty dt\gamma(t)e^{-zt} = \int_{-\infty}^\infty d\psi \frac{z\mathcal{J}(\psi)}{z^2+\psi^2}. \tag{4.67}$$

When only quasielastic processes are taken into account $\psi \approx 0$, and thus we can approximate $\mathcal{J}(\psi) \approx \mathcal{J}(0)$. Using the fact the $\int_{-\infty}^\infty d\psi \cos\psi t = 2\pi\delta(t)$, we then find from Eqs. (4.64) and (4.65) that

$$\gamma(t) = \bar{\gamma}\delta(t), \quad \hat{\gamma}(z) = \bar{\gamma}/2,$$

with the damping coefficient $\bar{\gamma}(T)$

$$\bar{\gamma}(T) = 2\pi\mathcal{J}(0) = -\frac{4\pi\hbar}{M}\int_0^\infty d\xi\varphi(\xi)\frac{\partial\bar{n}(\xi)}{\partial\xi}, \tag{4.68}$$

where we defined

$$\varphi(\xi) = \lim_{\psi\to 0}\psi^2 S\left(\xi+\frac{\psi}{2}, \xi-\frac{\psi}{2}\right). \tag{4.69}$$

According to Eq. (4.66) the real part of the optical conductivity has a typical Drude-like shape

$$Re\sigma(\omega) = \frac{nq^2}{M}\frac{\bar{\gamma}/2}{\omega^2+(\bar{\gamma}/2)^2}, \tag{4.70}$$

where $\bar{\gamma}/2$ plays the role of the inverse scattering time. It is then natural to introduce the inverse mobility as

$$\mu^{-1} = \frac{M\bar{\gamma}}{2q}. \tag{4.71}$$

It is worth noting that, even though the formula (4.66) is general, in the computation of the damping function (4.61) we considered only low-energy quasielastic processes, which give rise to the Drude-like response (4.70). If one keeps in the evaluation of $\mathcal{J}(\psi)$ the next nonvanishing contribution to Eq. (4.67),

$$\mathcal{J}(\psi) \approx \mathcal{J}(0) + \mathcal{J}_2\psi^2, \quad \psi < \omega_c,$$

where ω_c is a proper cutoff for the previous expansion, $\hat{\gamma}(z)$ can be estimated as

$$\hat{\gamma}(z) = \pi\left[\mathcal{J}(0) - z^2\mathcal{J}_2\right] + 2\mathcal{J}_2\omega_c z.$$

The corresponding optical conductivity is then

$$Re\sigma(\omega) = \frac{nq^2}{M}\frac{\pi\mathcal{J}(0)+\pi\mathcal{J}_2\omega^2}{\omega^2(1+2\mathcal{J}_2\omega_c)^2+(\pi\mathcal{J}(0)+\pi\mathcal{J}_2\omega^2)^2},$$

which is qualitatively the same as the one given in Eq. (4.70). In particular, the dc conductivity is found to be the same. Since in the following we will address the issue of the temperature dependence of the dc resistivity, we can safely rely on the approximation (4.68) of the damping coefficient, which takes into account only the contribution of $\mathcal{J}(0)$.

4.4.2 Evaluation of the damping coefficient

In order to determine the damping coefficient (4.68), we first have to evaluate the function $\varphi(\xi)$ defined in Eq. (4.69). By rewriting the summations over the (radial) indexes n, p in Eq. (4.62) as integration over continuum variables, and taking into account that $\Delta q_n \sim \pi/\ell$, we find that

$$\begin{aligned} S(k,k') \;\equiv\; & S^{yy}(k,k') = S^{xx}(k,k') = \frac{\ell^2}{\pi^2 c^2} \sum_{ml} \int dq \int dq' |G^x_{qm,q'l}|^2 \\ \times\; & \delta(k-q)\delta(k'-q') = \frac{\ell^2}{\pi^2 c^2} \sum_{ml} |G^x_{km,k'l}|^2, \\ & S^{xy}(k,k') = \frac{\ell^2}{\pi^2 c^2} \sum_{ml} G^{x*}_{km,k'l} G^y_{km,k'l} = 0, \end{aligned} \tag{4.72}$$

where $k = \omega/c$, $k' = \omega'/c$, and the last equation follows from Eq. (J.8). The limit (4.69) thus acquires the form

$$\varphi(\xi) = \frac{\ell^2}{\pi^2} \lim_{(k-k')\to 0} (k-k')^2 \sum_{ml} |G^x_{mk,lk'}|^2. \tag{4.73}$$

From the above relation it is obvious that the only terms of $|G^x_{km,k'l}|^2$ which contribute to the limit (4.69) are those behaving like $\sim 1/(k-k')^2$, i.e., the term proportional to $\Lambda^{(2)}$ in Eq. (J.8). We then find

$$\sum_{ml} |G^{(2)}_{km,k'l}|^2 = \frac{2k^2}{\ell^2 (k-k')^2} \sum_{m} |\Lambda^{(2)}_{m+1,m}|^2, \tag{4.74}$$

where

$$\begin{aligned} \left|\Lambda^{(2)}_{m+1,m}\right|^2 \;=\; & \left(e^{i\pi/2} + e^{-i\pi/2} e^{2i(\delta_{m+1}-\delta_m)}\right) \\ \times\; & \left(e^{-i\pi/2} + e^{i\pi/2} e^{-2i(\delta_{m+1}-\delta_m)}\right) = 4\sin^2(\delta_{m+1}-\delta_m). \end{aligned} \tag{4.75}$$

Substituting Eq. (4.75) into Eq. (4.74), and evaluating the limit (4.73), we finally obtain

$$\varphi(\xi) = \frac{8\xi^2}{\pi^2 c^2} \mathcal{G}(\xi), \tag{4.76}$$

where $\xi = ck$, and we defined

$$\mathcal{G} \equiv \sum_{m=0}^{\infty} \sin^2(\delta_{m+1} - \delta_m). \tag{4.77}$$

Using the preceding equation, the damping coefficient (4.68) acquires the form

$$\bar{\gamma}(T) = \frac{32\hbar^2}{M\pi c^2 k_B T} \int_0^{\infty} d\xi \mathcal{G}(\xi) \frac{\xi^2 e^{\frac{\hbar\xi}{k_B T}}}{\left(e^{\frac{\hbar\xi}{k_B T}} - 1\right)^2}. \tag{4.78}$$

Observe that Eq. (4.78) is valid for both kinds of defect solution (4.12) and (4.13). However, since the phase shifts are determined by the eigenfunction η of the scattering problem (4.22), Ψ_{1v} or Ψ_{2v} will give rise to different potentials $V_{1v}(\mathbf{r})$ or $V_{2v}(\mathbf{r})$, and then different phase shifts. As a consequence, also the function $\mathcal{G}(\xi)$ in Eq. (4.77) will be different in the two cases, leading to a different temperature dependence of the damping coefficient (4.78).

4.5 Inverse mobility

We evaluate the phase shifts by adopting the Born approximation [111, 113]. The phase shift $\delta_m(k)$ of the wave function with angular momentum m and wave vector k then reads

$$\delta_m(k) = \arctan \pi \mathcal{A}_m(k), \tag{4.79}$$

where $\mathcal{A}_m(k)$ is the expectation value of the potential over the eigenfunction of the corresponding unperturbed Klein-Gordon equation, i.e., the Bessel function $J_m(kr)$ in the case of Eq. (4.22)

$$\mathcal{A}_m(k) = \int_0^{\infty} dr r [J_m(kr)]^2 V(r). \tag{4.80}$$

4.5.1 Vortex-antivortex pair

Let us first consider the case of the scattering of a vortex-antivortex pair by the magnons. In this case the potential $V(\mathbf{r})$ in Eq. (4.22) has the form

$$V_{2v}(\mathbf{r}) = \frac{1}{4}(\nabla\Psi_{2v})^2, \tag{4.81}$$

where $\Psi_{2v} = \Psi_{1v}^{(1)} - \Psi_{1v}^{(2)}$, with Ψ_{1v} given by Eq. (D.2). One can readily show that

$$\begin{aligned} \left(\nabla\Psi_{1v}^{(1,2)}\right)^2 &= \frac{1}{(\mathbf{r} - \mathbf{R}_{1,2})^2}, \\ \left(\nabla\Psi_{1v}^{(1)}\right)\left(\nabla\Psi_{1v}^{(2)}\right) &= \frac{(\mathbf{r} - \mathbf{R}_1)\cdot(\mathbf{r} - \mathbf{R}_2)}{(\mathbf{r} - \mathbf{R}_1)^2(\mathbf{r} - \mathbf{R}_2)^2}, \end{aligned}$$

which gives, using the translational invariance $\mathbf{r} - \mathbf{R} \to \mathbf{r}$

$$(\nabla \Psi_{2v})^2 = \frac{\mathbf{d}^2}{(\mathbf{r} - \mathbf{d}/2)^2 (\mathbf{r} + \mathbf{d}/2)^2} = \frac{d^2}{(r^2 + d^2/4)^2 - (\mathbf{r} \cdot \mathbf{d})^2}.$$

Since the distance d between defects is a fixed parameter and we consider length scales $r \gg d$, we can approximate the potential as

$$V_{2v}(\mathbf{r}) = \frac{d^2/4}{(r^2 + d^2/4)^2}. \tag{4.82}$$

For the potential (4.82), Eq. (4.80) can be evaluated analytically for $m \geq 1$, yielding

$$\begin{aligned} \mathcal{A}_m(k) &= \frac{\pi k d}{4} \{ I_m(kd/2) \left[K_{m-1}(kd/2) + K_{m+1}(kd/2) \right] \\ &- K_m(kd/2) [I_{m-1}(kd/2) + I_{m+1}(kd/2)] \}, \end{aligned}$$

where I_n and K_n are the modified Bessel functions of the first and the second kinds, respectively.

Returning to Eq. (4.77), we observe that $\mathcal{G}(\xi = k/c)$ is a function of the dimensionless variable $y = \xi d/2c$. Introducing the same variable also into Eq. (4.78), we may rewrite the inverse mobility given by Eq. (4.71) as

$$\mu^{-1}(T) = \mu_0^{-1} \frac{128}{\pi} \frac{E_c}{\alpha^3 T} \int_0^\infty dy y^2 \mathcal{G}(y) \frac{e^{\frac{2E_c y}{\alpha T}}}{(e^{\frac{2E_c y}{\alpha T}} - 1)^2}, \tag{4.83}$$

where $\mu_0^{-1} = \hbar/ea^2$ is the quantum of inverse mobility for a given lattice spacing a, $d = \alpha a$, and $E_c = \hbar c/ak_B$ is the characteristic temperature scale associated with the magnons. Although a quantitative estimate of Eq. (4.83) requires the knowledge of the values of these microscopic parameters, its qualitative behavior can be promptly understood. In particular, since all the temperature dependence of μ^{-1} is due to the Bose factor in Eq. (4.83), the inverse mobility is expected to vanish at zero temperature, where no thermally activated scattering processes exist, and increases linearly at high temperatures, with the slope determined by the shape of the function $\mathcal{G}(y)$. In the left panel of Fig. 4.5 we plot $(\mu/\mu_0)^{-1}$ as a function of T/E_c for several values of α. One observes that already at small fractions of the ratio T/E_c, the inverse mobility is *linear* in temperature. Moreover, as α increases the linear behavior arises at even smaller temperatures, and the overall value of the inverse mobility decreases.

4.5.2 Single vortex

Let us analyze now the behavior of the inverse mobility obtained when we identify the defect as a single vortex. In this case, instead of Eq. (4.81), the scattering

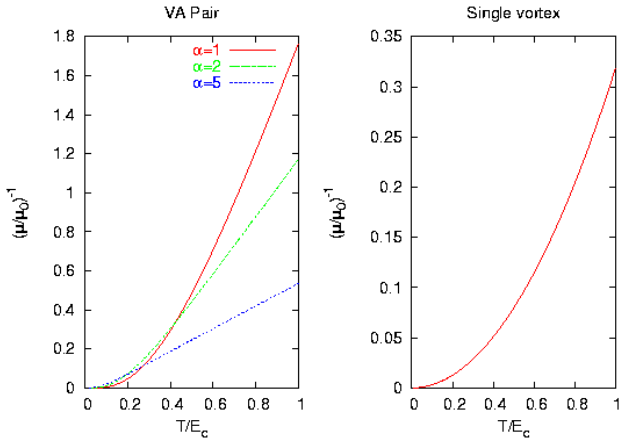

Figure 4.5: Inverse mobility in units of μ_0^{-1} as a function of the rescaled temperature T/E_c. Left panel: inverse mobility of a vortex-antivortex pair, according to Eq. (4.83), at several values of α. Right panel: inverse mobility of a single-vortex defect, according to Eq. (4.85)

potential reads

$$V_{1v}(\mathbf{r}) = \frac{1}{4}(\nabla\Psi_{1v})^2 = \frac{1}{4r^2}.$$

As a consequence, the phase shifts defined by Eqs. (4.79) and (4.80) are given by ($m \geq 1$)

$$\delta_m = \arctan\frac{\pi}{8m}. \tag{4.84}$$

Note that the phase shifts in the case of a single-vortex do not depend on the wave-vector, but only on the angular momentum. Thus, the function $\mathcal{G}$ defined by Eq. (4.77), does not depend on the frequency

$$\mathcal{G} = \sum_{m=1}^{\infty} \frac{64\pi^2}{64\pi^2 + [\pi^2 + 64m(m+1)]^2} \approx 0.032.$$

Because $\mathcal{G}$ is a constant, we can introduce the rescaled variable $y \equiv \hbar\xi/k_BT$ into the expression (4.71) for the inverse mobility, which yields

$$\mu^{-1}(T) = \mu_0^{-1}\frac{8\pi}{3}\mathcal{G}\left(\frac{T}{E_c}\right)^2. \tag{4.85}$$

Here, we used the fact that $\int_0^\infty dy y^2/(e^y-1)^2 = \pi^2/3$. In comparison with the case of a vortex-antivortex pair, the main difference is that here the inverse mobility

depends on the square of the temperature, for all the temperatures. In the right panel of Fig. 4.1 we plot $(\mu/\mu_0)^{-1}$ as a function of T/E_c: notice that the overall variation of the inverse mobility is smaller compared to the case of the vortex-antivortex pair, but they are still of the same order of magnitude.

4.6 Transport in the spin-glass phase of $La_{2-x}Sr_xCuO_4$

4.6.1 Microscopic origin of the $SO(3)$ nonlinear sigma model

Although the model we developed in this chapter could be applied to describe the dynamics of topological defects in several frustrated Heisenberg spin systems, here we concentrate on lightly doped LSCO. In order to relate the dynamics of the vortex-like defects to the transport properties in cuprates, it is necessary to connect the $SO(3)$ nonlinear sigma model, which describes the dynamics of the long-wavelength fluctuations around a noncollinear spin state, to a model, governing the dynamics of the microscopic degrees of freedom present in the system. Indeed, Klee and Muramatsu have considered this problem in Ref. [42], starting with the microscopic spin-fermion model, in which the itinerant fermions, representing the doping introduced in the system, are coupled to the Cu^{2+} spins, localized on the sites of a square lattice, via a Kondo-like interaction

$$H_{SF} = \sum_{\langle jj'\rangle\alpha} t_{jj'} c^{\dagger}_{j\alpha} c_{j'\alpha} + \sum_i \left(\sum_{\langle jj',i\rangle,\alpha\beta} J_K^{jj',i} c^{\dagger}_{j\alpha} \boldsymbol{\sigma}_{\alpha\beta} c_{j'\beta} \right) \cdot \mathbf{S}_i + J \sum_{\langle ii'\rangle} \mathbf{S}_i \cdot \mathbf{S}_{i'}. \quad (4.86)$$

Here, the operators $c^{\dagger}_{j\alpha}$ and $c_{j\alpha}$ create and annihilate, respectively, a hole with spin projection $\alpha = \pm 1/2$ on the site j, residing on the Cu-Cu bond. The operator $\mathbf{S}_i$ is the spin$-1/2$ operator for the Cu^{2+} spin localized on the site i. The kinetic term describes the hopping between the sites j and j', and include the direct hopping between these sites, as well as the indirect one mediated via the central site i. The term proportional to J_K describes a nonlocal Kondo-like interaction between the localized spins and the holes. The vector $\boldsymbol{\sigma}$ represents the Pauli matrices. The sum $\langle jj', i\rangle$ is over the pairs of sites j, j', which are nearest neighbors to the site i. The last term in the above Hamiltonian represents the Heisenberg interaction between the nearest neighboring localized spins.

The spin-fermion model is analytically tractable, which is an important advantage in comparison with other models adopted for describing strongly correlated fermion systems. In particular, starting with the a helicoidal spin ground state, Klee and Muramatsu have shown that it is possible to integrate out the fermions and they have obtained the corresponding $SO(3)$ nonlinear sigma model, which

describes the low-energy dynamics of the fluctuations around the noncollinear ground state. The derivation of the $SO(3)$ nonlinear sigma model from the spin-fermion model follows essentially the same steps as the one of the $O(3)$ nonlinear sigma model from the Heisenberg Hamiltonian. Here, we start with a noncollinear ground state, given by $\mathbf{S}_i/S \equiv \mathbf{n} = \mathbf{n}_1 \cos(\mathbf{k}_s \cdot \mathbf{r}) - \mathbf{n}_2 \sin(\mathbf{k}_s \cdot \mathbf{r})$, where $\mathbf{n}_1$ and $\mathbf{n}_2$ are constant vectors. In order to include the fluctuations around the ground state, a small uniform component, $\mathbf{L}$, is introduced, and the vectors $\mathbf{n}_1$ and $\mathbf{n}_2$ are allowed to vary in space and time. Thus, the total spin reads

$$\frac{\mathbf{S}}{S} = \frac{\mathbf{n} + a\mathbf{L}}{\sqrt{1 + 2a\mathbf{n}\cdot\mathbf{L} + a^2\mathbf{L}^2}}. \tag{4.87}$$

After the fermions have been integrated out, as well as the uniform spin component, $\mathbf{L}$, the resulting long-wavelength action has the form of the $SO(3)$ nonlinear sigma model (4.2) with an additional term

$$\mathcal{S}^{KM} = \int dt\, d^2\mathbf{r} \left[\kappa_k (\partial_t \mathbf{n}_k)^2 - p_{k\alpha} \left(\partial_\alpha \mathbf{n}_k\right)^2\right] - s_\alpha \int dt\, d^2\mathbf{r}\, \left(\mathbf{n}_1 \cdot \partial_\alpha \mathbf{n}_2\right). \tag{4.88}$$

In the above action both the superexchange J between the nearest neighboring spins and the fermionic susceptibilities contribute to the coupling constants κ and p_α. If only the Heisenberg interaction is considered, then the parameters of the effective model (4.88) read

$$\begin{aligned}
&\kappa_1 = \kappa_2 \equiv \kappa = \frac{1}{8Ja^2[2 + \sum_\alpha \cos(Q_\alpha a)]}, \qquad \kappa_3 \simeq 0, \\
&p_{1\alpha} = p_{2\alpha} = \frac{JS^2}{4}\cos(Q_\alpha a), \qquad p_{3\alpha} \simeq 0, \\
&s_\alpha = \frac{JS^2}{a}\sin(Q_\alpha a).
\end{aligned} \tag{4.89}$$

The subtle interplay between holes and spins is represented in the last term of the microscopically derived effective model (4.88). Indeed, since it is not positive definite, the weight of some field configurations in the path integral will tend to infinity, hence leading to instabilities. When only the Heisenberg interaction is considered in the microscopic Hamiltonian, this term is present for any incommensurate ground state, thus leading to the instability of such a ground state, which is known to occur in the pure Heisenberg model. In order to ensure the stability of the incommensurate ground state, the condition of the vanishing of the *full* coefficients $s_\alpha = \chi_\alpha - (JS^2/a)\sin(Q_\alpha a)$ must be imposed, where χ_α is the contribution arising from the presence of holes. This stability argument, in turn, determines the spiral incommensurability Q_α as a function of the microscopic parameters and the doping concentration within the effective theory, describing the long-wavelength fluctuations around the noncollinear state (4.1), which corresponds to the spin-fermion model (4.86) [42].

A more general derivation of the stability condition has been proposed recently by Hasselmann *et al.* [43, 44]. In this approach, Eq. (4.88) is considered as the continuum limit of the Heisenberg model alone and the effect of doping is included within a minimum coupling of the order parameter to a gauge field $\mathbf{B}_\alpha$ representing the dipolar character of the hole state, already emphasized by Shraiman and Siggia [71, 73, 86]. It has been then shown that the stability condition

$$p_{k\alpha}\partial_\alpha \mathbf{n}_k \cdot [\mathbf{B}_\alpha]_D \times \mathbf{n}_k + s_\alpha \mathbf{n}_1 \cdot \partial_\alpha \mathbf{n}_2 = 0,$$

where $[\mathbf{B}_\alpha]_D$ denotes the ordered fraction of dipoles, relates the incommensurate vector $\mathbf{Q}$ to the hole density [43, 44], in agreement with neutron scattering measurements in lanthanum cuprates [37, 38, 39, 40]. Moreover, the dipolar frustration described within this minimal-coupling scheme renormalizes the bare coefficients $p_{k\alpha}$, given by Eq. (4.88), leading the system toward a stable fixed point where $p_{1\alpha} = p_{2\alpha} = p_{3\alpha} \equiv p_\alpha$, which corresponds to the model (4.3) that we considered. In this picture we can also determine the parameter $\kappa = JS^2/4c^2$, where $c = \sqrt{c_\parallel c_\perp} \approx 2\sqrt{2}JSa$ and $(c_\parallel/c_\perp)^2 = \cos(Qa)$ [43, 44]. As a consequence, we can now apply our previous results to the spin-glass phase of the LSCO compound.

4.6.2 Inverse mobility in cuprates

Until now we evaluated the inverse mobility of the defect without specifying how this quantity can be accessed experimentally. As we explained above, in lightly doped cuprates the holes act at the same time as source and stabilizing mechanism of the dipolar frustration. When topological defects are present in the spiral spin texture, one could expect that the holes sit on top of the defects (single vortex or vortex-antivortex pair) to minimize the frustration. Thus, the measured in-plane inverse mobility of the holes would be described by Eq. (4.71) with the damping coefficient given by Eq. (4.78). However, this scenario should apply only for temperatures above 150 K, because below this temperature the experiments signal charge localization.

In the case of cuprates, the magnon temperature E_c is the antiferromagnetic coupling $J \approx 1200$ K measured at zero doping. Actually, a lower value is expected, if one takes into account the renormalization of the spin-spin interaction due to the disorder introduced by hole doping and quantum effects. The resulting inverse mobility as a function of temperature for the case of a vortex-antivortex pair is reported in Fig. 4.6 for several values of E_c and α. The linear temperature dependence of the inverse mobility at high temperatures can be obtained from Eq. (4.83) by expanding the exponential in that equation,

$$\mu^{-1}(T) \simeq \mu_0^{-1} \frac{T}{\alpha E_c} \int_0^\infty dy\, \mathcal{G}(y). \tag{4.90}$$

Observe that using $a = 3.8\mathring{A}$, as appropriate for cuprates, one obtains for the inverse mobility $\mu_0^{-1} = 0.46$ Vs/cm^2. The resistivity, in the low-doping regime,

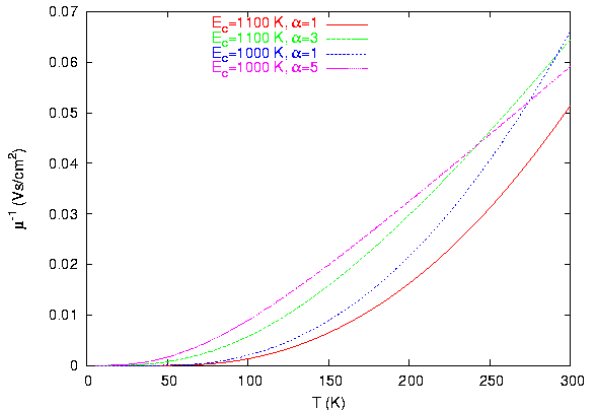

Figure 4.6: Contribution (4.83) of the motion of a vortex-antivortex pair to the inverse mobility of the holes in cuprates.

is related to the inverse mobility as $\rho = (\mu n_h e)^{-1}$, with n_h denoting the charge carrier concentration, which yields $\rho \sim 1\text{m}\Omega$, as experimentally observed, see Fig. 4.7. The resistivity depends linearly on temperature, as given by Eq. (4.90),

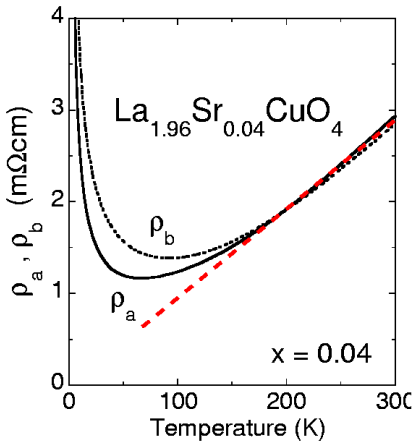

Figure 4.7: Comparison of the theoretically calculated resistivity at high temperatures (dashed line), given by Eq. (4.90), with the measured resistivity (solid and dotted lines) from Ref. [47].

which is expected to hold for $T < T_{KT}$, where T_{KT} is the Kosterlitz-Thouless

temperature, at which the vortex-antivortex pairs will eventually unbind. An attempt to roughly estimate T_{KT} has provided $T_{KT} \sim JS^2$ [43, 44]. Using that $J \sim 0.1$eV and $S = 1/2$, we find $T_{KT} \sim 300$K. Despite of the crudeness of the estimates, this result compares quite well with the experimental data [114], which shows deviations from linearity at $T \sim 400$K. Given that T_{KT} represents the temperature at which few pairs start to unbind, it is not surprising that the linear behavior can hold up to higher temperatures.

In order to provide also a comparison with the experimental data concerning the anisotropy in dc transport, we should include the spin-wave anisotropy in the helicoidal state. The analytical calculations which led to Eqs. (4.83) cannot be performed for an anisotropic magnon bath. Nevertheless, we provide a rough estimate of this effect by considering the dependence of the inverse mobility in Eq. (4.90) on the spin-wave velocity, c. Since the inverse mobility for the isotropic system is inversely proportional to the spin-wave velocity, $\mu^{-1} \sim c^{-1}$, it is then expected that in the original anisotropic system $\mu_\perp^{-1} \propto c_\perp^{-1}$ and $\mu_\parallel^{-1} \propto c_\parallel^{-1}$. This result can also be understood on physical grounds: since dissipation is provided by the excitations of the magnon bath, spin-waves with higher velocity are less effective in scattering the defects. As a consequence, the resistivity in the direction of helicoid is larger than that in the direction perpendicular to it, $\gamma_\perp/\gamma_\parallel = \rho_\perp/\rho_\parallel = c_\parallel/c_\perp = \sqrt{\cos(Qa)}$. For $x = 0.04$, we find $\sqrt{\cos(Qa)} = 0.98$, in agreement with transport measurements by Ando *et al.* [47], which found that for 100K$< T <$ 200K the resistivity along the a-axis in LSCO is slightly smaller than along the b-axis (in orthorhombic coordinates). We recall that the incommensurate peaks observed in neutron scattering correspond to the b-direction, which coincides with the axis of the helicoid. Thus, $\rho_\perp \equiv \rho_a, \rho_\parallel \equiv \rho_b$ and $\rho_a < \rho_b$, as experimentally observed. This result indicates that the anisotropy measured in the spin-glass phase does not provide evidence for the existence of diagonal stripes, but instead, it is also the result expected within a more realistic, albeit more complex, model which does not need to appeal to charge order at such small doping concentrations.

The inverse mobility of a single defect is shown in Fig. 4.8. The overall variation of the inverse mobility turns out to be quantitatively smaller in this case. As we explained in the previous section, the main difference between the temperature dependence of the inverse mobility obtained with the single vortex or with the vortex-antivortex pair is that in the former case $\mu^{-1} \propto T^2$ always, while in the latter case μ^{-1} evolves towards a linear behavior at a crossover temperature which depends on E_c and α. As we discussed in Sec. 4.2, the presence of the two kinds of defects depends on their energy, which scales as $E[\Psi_{1v}] \sim \ln \xi$ for the single vortex and $E[\Psi_{2v}] \sim \ln d$ for the pair, where ξ is the correlation length and d the distance between vortices, respectively. In the absence of disorder and at low temperatures, one would expect ξ to be finite, but still large enough to prevent the formation of free defects below the crossover temperature T_v, where pairs start to unbind [98, 99, 100, 101]. However, in Refs. [43, 44] it has been argued

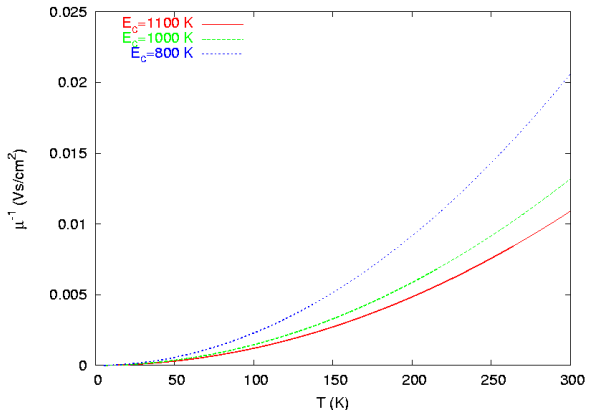

Figure 4.8: Contribution (4.83) of the motion of a single-vortex defect to the inverse mobility of the holes in cuprates.

that disorder leads to a strong reduction of the correlation length, and thus single defects start to proliferate already at temperatures lower than T_v. Comparison with recent resistivity data seems to support this conclusion. Indeed, studies performed by Ando *et al.* [115] for compounds in the spin-glass regime indicate that the second derivative of the in-plane resistivity with respect to the temperature is positive up to $\sim 300K$, implying that $\rho_{ab} \sim T^{\eta}$ with $\eta > 1$. Based on previous experiments [47], we interpreted the resistivity data for cuprates in terms of the dissipative motion of vortex-antivortex pairs only, which gives rise to a linear resistivity, as we discussed above. However, in the light of these more recent data, one could speculate about the coexistence of single-vortices and vortex-antivortex pairs, which would consequently lead to a power-law behavior of the resistivity with a more complicated exponent, expected to be larger than one.

Chapter 5

Conclusions and Outlook

In this thesis, we considered the magnetic properties of undoped and lightly doped $La_{2-x}Sr_xCuO_4$, i.e., for $x < 5\%$, within the framework of a generalized nonlinear sigma model, which includes the Dzyaloshinskii-Moriya and pseudodipolar anisotropies, and where the doping is represented by an effective dipole field coupled to a background magnetization current. We also addressed the problem of transport in the spin-glass phase of the compound, i.e., for $2\% < x < 5\%$, by studying the dissipative motion of the vortex-like topological defects that arise due to a nontrivial spiral magnetic ground state present at this doping level. We summarize below the main results contained in this thesis.

In Chapter 2, motivated by recent magnetic susceptibility measurements by Lavrov *et al.* [36], which revealed a complete anisotropy in the magnetic susceptibility response in La_2CuO_4 and a zero-temperature hierarchy different than the one expected for an ordinary easy-axis antiferromagnet, we considered the dynamics of the long-wavelength spin fluctuations starting with the single-layer spin Hamiltonian that includes anisotropic Dzyaloshinskii-Moriya and pseudodipolar interactions, besides the ordinary Heisenberg exchange. We mapped this microscopic model into a corresponding field theory, which describes the long-wavelength magnetic fluctuations, and appears to be a generalized nonlinear sigma model. The effect of these anisotropic interactions is to introduce finite gaps for the magnetic excitations, which lead to the magnetic ground state with a staggered magnetization oriented along the b orthorhombic axis and a weak ferromagnetic moment perpendicular to the CuO_2 planes, resulting in the canted Néel order for the spins within a single CuO_2 layer. A small antiferromagnetic coupling between the layers induces the staggered ordering of the weak ferromagnetic moments between the layers, leading to a 3D Néel ordering in the compound. In order to evaluate the magnetic susceptibility, we then considered the effect of an externally applied magnetic field to the system. We rederived the theory describing the long-wavelength

magnetic fluctuations about the ground state, and found that the resulting nonlinear sigma model, besides the usual shift in the time derivative of the staggered order parameter, describing the precession of the staggered magnetization around the applied field, contains an unexpected source term for the staggered magnetization, which is introduced by the Dzyaloshinskii-Moriya interaction. We showed that this term, in turn, leads to an additional contribution to the magnetic susceptibility, which is responsible for the observed complete anisotropy in the magnetic susceptibility response [36]. Finally, the same term accounts for the observed unusual zero-temperature hierarchy of the magnetic susceptibilities, rendering the La_2CuO_4 system an example of an unconventional easy-axis antiferromagnet.

In Chapter 3, we considered the role of the Dzyaloshinskii-Moriya and the pseudodipolar interactions in determining the magnetic properties when Sr doping is introduced in the La_2CuO_4 system, i.e., La^{3+} is replaced by Sr^{2+}, using the description based on the nonlinear sigma model, which includes these anisotropic interactions and was already employed in Chapter 2 for describing the magnetism of the undoped compound. Following the seminal ideas of Shraiman and Siggia [71, 73, 79], we represented the dopant holes via an effective dipole field that couples to the background magnetization current. We first considered the effect of the dipoles on the magnons in the Néel phase, for $x < 2\%$. By integrating out the dipole field at the one-loop level, we showed that the dipole-magnetization current interaction leads to a reduction of the Dzyaloshinskii-Moriya and the pseudodipolar spin gaps. Consequently, the magnetic susceptibility exhibits the same qualitative features as in the undoped compound, in particular the susceptibility when the magnetic field is applied along the a orthorhombic axis, χ_a, remains featureless. We calculated the reduction of the Dzyaloshinskii-Moriya gap due to the dipole-magnetization current interaction, and found that it is approximately 27% at the doping concentration of $x = 1\%$, in good agreement with recent Raman scattering experiments by Gozar *et al.* [46]. The decrease of the Dzyaloshinskii-Moriya gap with the doping is expected even without taking into account the interaction of the holes with magnons, because of the linear decrease of the tilting angle of the CuO_6 octahedra with doping. The reduction of the Dzyaloshinskii-Moriya gap caused by this mechanism is of the order of a few percent, much smaller than experimentally observed, showing the crucial role of the interaction of the dopant holes with magnons, represented by the dipole-magnetization current coupling within our model, in determining the doping dependence of the spin gaps in the compound. We found that, at the doping concentration $x_{AF} \simeq 2\%$, the dipole field acquires a non-zero expectation value, $\langle \mathbf{P}_\mu \rangle \neq 0$, with the spin part oriented along the b orthorhombic axis, and the Néel state thus becomes unstable. Assuming that the dipoles acquire a non-zero expectation value along the same direction in the lattice space, we found that the spins rearrange to form an incommensurate helicoidal configuration, with the pitch along the b orthorhombic axis and the spins rotating in the ac plane. In addition, the staggered magnetization, besides the he-

licoidal component, has a dominant component oriented along the b orthorhombic direction, thus giving rise to a total staggered magnetization oriented in the same direction. Consequently, the weak ferromagnetic moment is perpendicular to the CuO_2 planes, thus leading to the total spin confined to the bc plane, consistent with the recent magnetic susceptibility measurements by Lavrov *et al.* [36]. The incommensurability of the helicoidal state gives rise to two incommensurate peaks along the b orthorhombic axis observed by neutron scattering experiments in the spin-glass phase of $La_{2-x}Sr_xCuO_4$ [39]. Since the Dzyaloshinskii-Moriya gap vanishes at the onset of the spin-glass phase, the incommensurability, Q, is related to the pseudodipolar gap, M_c, and the doping concentration, x, as $Q^2 \sim x^2 - M_c^2/2$. Such a behavior can explain the deviation of the incommensurability from the linear doping dependence when the spin-glass phase sets in, as experimentally observed [39]. In addition, the same result allowed us to make a new experimental prediction that relates Raman and neutron scattering experiments, namely, that the pseudodipolar gap should vanish at the same doping level at which the linear doping dependence of the incommensurability is recovered. We also considered the behavior of the incommensurability in a magnetic field applied perpendicularly to the CuO_2 planes, and we found that an increase in the value of the incommensurability is expected in this case. The behavior of the incommensurability in the perpendicular magnetic field within the stripe model is completely different, namely, the incommensurability remains constant, with an increase in the intensity of the corresponding magnetic peaks. These findings led us to propose a measurement of the doping dependence of the incommensurability in a magnetic field perpendicular to the CuO_2 planes as a "smoking-gun" experiment that would discriminate between the helicoidal and the stripe picture in the spin-glass phase of $La_{2-x}Sr_xCuO_4$.

In Chapter 4, we considered the dynamics of topological defects in a spin system with a noncollinear ground state. The long-wavelength dynamics of the spin fluctuations is described by an $SO(3)$ nonlinear sigma model, and the corresponding topological defects, associated with the change of chirality of the noncollinear state, appear to be vortex-like. We concentrated on the contribution of these topological defects to transport properties. Our approach extends to a non-Abelian field theory the well-known collective-coordinate method employed previously to study the dissipative mechanism in one- and two-dimensional systems [106, 107, 108, 109]. We considered two kinds of topological defects: a single vortex and a vortex-antivortex pair. We showed that the interaction between the defect and the spin waves is described by a particle coupled to a bath of harmonic oscillators. The scattering of the defect by the magnons leads to its dissipative motion. We integrated out the bath and calculated the mobility of the defect. Quite generally, its temperature dependence is determined by the thermal activation of the magnons, which vanishes at zero temperature and follows, at higher temperatures, a power law whose exponent depends on the type of defect. In particular, we found that it

is linear for the vortex-antivortex pair and quadratic for the single vortex. At the end of this chapter, we applied the model to describe transport in lightly doped lanthanum cuprates, motivated by recent measurements of the dc resistivity inside the spin-glass phase of $La_{2-x}Sr_xCuO_4$ by Ando *et al.* [47]. Our results for the mobility indicate indeed that a possible mechanism of transport in these materials, for 150K$< T <$300K, could be the dissipative motion of an electrical charge attached to a single vortex or a vortex-antivortex topological defect. Although we applied the model to the particular case of lightly doped $La_{2-x}Sr_xCuO_4$, the approach presented here is quite general, and can be employed to investigate the role of topological defects in any frustrated spin system with the long-wavelength dynamics described by the $SO(3)$ nonlinear sigma model. Complementary to our work, Sushkov and Kotov have recently considered the problem of transport in the spin-glass phase of $La_{2-x}Sr_xCuO_4$ at lower temperatures, $T < 150$K, in Ref. [116] using the spiral solution of the $t - t' - t'' - J$ model (3.6) with the Coulomb impurities. Anisotropy in the in-plane resistivity, within this model, results from the deformation of the hole wave-function introduced by the spin spiral rather than the tendency of the holes to form charge stripes, and it is in good agreement with experiments [47]. An interesting problem that remains to be addressed within our model for transport, based on the dynamics of topological defects formed in a helicoidal state, is the coupling between vortex-like defects and the holes. Namely, we assumed that the holes are attached to the defects, which allowed us to relate the dissipative properties of the defects with the charge transport. The assumption is justified a posteriori by comparison with the experiments, but its theoretical foundation is still missing.

The final comment concerns the problem of reconciling the spiral and the stripe pictures in the superconducting phase of $La_{2-x}Sr_xCuO_4$, when the low-temperature tetragonal phase is stabilized, for instance, by Nd-co-doping. This issue has indeed been recently considered by Silva Neto in Ref. [117], where it has been argued that the magneto-elastic coupling between Cu^{2+} spins forming a spiral with the pitch along one of the main crystallographic axes in the tetragonal phase and the Dzyaloshinskii-Moriya vector, which determines the tilting axis of the CuO_6 octahedron, favors the formation of horizontal/vertical charge stripes. Namely, the magneto-elastic coupling gives rise to an equilibrium configuration such that the thermodynamic Dzyaloshinskii-Moriya vector, the staggered and the uniform spin component form a triad of mutually orthogonal vectors, which can only move rigidly. Therefore, when Cu^{2+} spins form a spiral state, the tilting of the CuO_6 octahedra follows the pattern of the spins, see Fig. 5.1. On the other hand, because two octahedra in neighboring rows share an oxygen ion, they tilt in the opposite directions, and thus the spins in the neighboring rows have an opposite sense of rotation. Consequently, starting with an antiferromagnetic spin configuration formed within one column, we find an entire column with the spins aligned in the same direction and identical octahedra, after the spins perform a

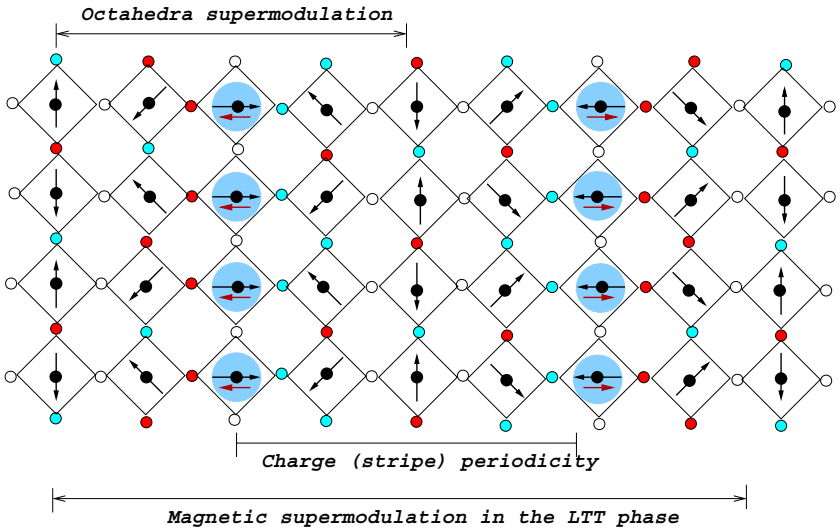

Figure 5.1: Spiralling of Cu^{2+} spins and tilting direction of the CuO_6 octahedra induced by magneto-elastic coupling in $La_{2-x}Sr_xCuO_4$, for $x = 1/8$, from Ref. [117]. Dark oxygen ions are canted up the plane, grey ones are canted down the plane, and the open ones are confined to the basal plane. The dopant holes (small arrows) form charge stripes in the columns with the spins aligned in the same direction and with the same octahedra.

rotation of $\pi/2$, as shown in Fig. 5.1. For a dopant hole is energetically favorable to form a Zhang-Rice singlet with a spin from this column, because there is no frustration involved in its motion within this column, and thus it is a valley with the least resistance for the hole motion. The same valley, but with the spins aligned in the opposite direction in comparison with the one previously described, is formed after the spins perform a π rotation, see Fig. 5.1. Therefore, the magnetic periodicity in the lattice space is twice the stripe space, i.e., the periodicity of the charge modulation associated with the dopant holes situated within each valley. In this way, the magneto-elastic coupling reconciles the formation of a spiral spin state with the self-organization of the dopant holes into the one-dimensional valleys of charge, or the stripes, within the low-temperature tetragonal phase.

In summary, we showed that the anisotropic Dzyaloshinskii-Moriya and the pseudodipolar interactions are responsible for the stability of the Néel phase, whereas, in the spin-glass phase, a helicoidal spin configuration is formed, which gives rise to two diagonal incommensurate peaks observed by neutron scattering. The helicoidal scenario is consistent with the formation of charge stripes in the superconducting phase, when the low-temperature tetragonal phase is stabilized.

Appendix A

Microscopic origin of the Dzyaloshinskii-Moriya and pseudodipolar interactions

In this Appendix, we sketch the derivation of the DM and XY Hamiltonians starting with the following Hubbard-like Hamiltonian for the holes in the CuO_2 plane, which includes the spin-orbit coupling on the Cu ion [53]

$$H = H_0 + H_t + H_{LS}, \tag{A.1}$$

with

$$H_0 = \sum_{j\sigma} \varepsilon_d d^\dagger_{j\sigma} d_{j\sigma} + \sum_{kn\sigma} \varepsilon_{p_n} p^\dagger_{kn\sigma} p_{kn\sigma} + U \sum_j n_j n_j, \tag{A.2}$$

$$H_t = \sum_{j\sigma} \sum_{k(j)n\sigma} (t_{j,kn} d^\dagger_{j\sigma} p_{kn\sigma} + H.c.), \tag{A.3}$$

and

$$H_{LS} = \lambda \sum_j \mathbf{L}_i \cdot \mathbf{S}_i, \tag{A.4}$$

where $k(j)$ denotes the kth oxygen site of the neighboring Cu site j, $d^\dagger_{j\sigma}$ is the creation operator of a hole with spin σ on the $d_{x^2-y^2}$ orbital of the jth Cu ion. U is the Coulomb repulsion between the holes on the Cu site, $t_{j,kn}$ denotes the hopping between the $3d_{x^2-y^2}$ orbital of the Cu ion and the $2p_n$ $(n = x, y, z)$ orbital of the neighboring O ion k. In the spin-orbit Hamiltonian, H_{LS}, $\mathbf{L}_j$ is the orbital

angular momentum operator of the hole in the $3d$ orbital of the Cu ion at the site j, $\mathbf{S}_j$ is the spin-$\frac{1}{2}$ operator at the site j, and λ is the spin-orbit coupling constant. The effective spin Hamiltonian has the form given by Eq. (2.6), which is obtained from Hamiltonian (A.1) by performing a perturbative expansion up to the fourth order terms in the hopping t and the spin-orbit coupling λ [53]. The parameters of the effective spin Hamiltonian may be expressed in terms of the microscopic parameters as follows

$$
\begin{aligned}
J &= 4\sum_{nn'}(t_{i,kn}t_{kn,j} + \mathbf{C}_{i,kn}\cdot\mathbf{C}_{kn,j})g_{nn'}(t_{j,kn'}t_{kn',i} + \mathbf{C}_{j,kn'}\cdot\mathbf{C}_{kn',i}),\\
\mathbf{D}_{ij} &= -4i\sum_{nn'}[(\mathbf{C}_{i,kn}t_{kn,j} + t_{i,kn}\mathbf{C}_{kn,j})g_{nn'}(t_{j,kn}t_{kn',i} + \mathbf{C}_{j,kn'}\cdot\mathbf{C}_{kn',i})\\
&-(t_{i,kn}t_{kn,j} + \mathbf{C}_{i,kn}\cdot\mathbf{C}_{kn,j})g_{nn'}(\mathbf{C}_{j,kn'}t_{kn',i} + t_{j,kn'}\mathbf{C}_{kn',i})]\\
\overleftrightarrow{\Gamma}_{ij} &= 4\sum_{nn'}\{(\overleftarrow{C}_{i,kn}t_{kn,j} + t_{i,kn}\overleftarrow{C}_{kn,j})g_{nn'}(\overrightarrow{C}_{j,kn'}t_{kn',i} + t_{j,kn'}\overrightarrow{C}_{kn',i}) + (i\leftrightarrow j)\\
&-\overleftrightarrow{1}[(\mathbf{C}_{i,kn}t_{kn,j} + t_{i,kn}\mathbf{C}_{kn,j})g_{nn'}(\mathbf{C}_{j,kn'}t_{kn',i} + t_{j,kn'}\mathbf{C}_{kn',i})]\},
\end{aligned}
\tag{A.5}
$$

with

$$
\mathbf{C}_{j,kn} = -\frac{\lambda}{2}\sum_{m}\frac{\mathbf{L}^{*}_{jm}}{\varepsilon_m}t_{jm,kn}, \tag{A.6}
$$

where $\mathbf{L}^{*}_{jm}$ is the complex conjugate of the matrix element of the operator $\mathbf{L}_j$ between the $3d_{x^2-y^2}$ orbital and the orbital m of the copper ion at the site j, and $t_{jm,kn}$ denotes the hopping between the mth orbital of the Cu ion at the site j and the $2p_n$ oxygen orbital at the site k. The vector with the arrow $\leftarrow$ or $\rightarrow$ indicates that the inner product is taken with the spin operator put in the direction of the arrow, and $\overleftrightarrow{1}$ is a 3×3 unity matrix. $g_{nn'}$ is given by

$$
g_{nn'} = \begin{cases} (U+\varepsilon_{p_n})/U\varepsilon^3_{p_n}, & (n=n')\\ \left[2\varepsilon_{p_n}\varepsilon_{p_{n'}} + U(\varepsilon_{p_n}+\varepsilon_{p_{n'}})\right]/2U\varepsilon^2_{p_n}\varepsilon^2_{p_{n'}}, & (n\neq n'). \end{cases}
$$

In order to obtain the parameters $\mathbf{C}$ and t, which determine the coupling constants of the spin Hamiltonian (2.6) via Eq. (A.5), we have to consider the crystal structure in the LTO phase. The CuO_6 octahedra perform a staggered rotation about the b-axis with an angle $\delta\sim 4^\circ$, which leads to a rearrangement of the copper $3d$

orbitals in the following way

$$
\begin{aligned}
|0\rangle &= |x^2-y^2\rangle + \frac{\delta}{\sqrt{2}}(|yz\rangle - |zx\rangle) \\
|1\rangle &= |3z^2-r^2\rangle + \frac{\delta\sqrt{3}}{\sqrt{2}}(|yz\rangle + |zx\rangle) \\
|2\rangle &= |yz\rangle - \frac{\delta}{\sqrt{2}}(|x^2-y^2\rangle + \sqrt{3}|3z^2-r^2\rangle - |xy\rangle) \\
|3\rangle &= |zx\rangle - \frac{\delta}{\sqrt{2}}(-|x^2-y^2\rangle + \sqrt{3}|3z^2-r^2\rangle - |xy\rangle) \\
|4\rangle &= |xy\rangle - \frac{\delta}{\sqrt{2}}(|yz\rangle + |zx\rangle).
\end{aligned} \tag{A.7}
$$

Here, the original copper orbitals, $|x^2-y^2\rangle$, $|3z^2-r^2\rangle$, $|xy\rangle$, $|yz\rangle$, $|zx\rangle$, are given in the tetragonal (xyz) coordinate system, which is obtained from the orthorhombic one by a rotation of 45°. The above form of the orbitals is used to derive the matrix elements $\mathbf{L}_{jm}$. The expressions for the hopping parameters t are obtained from the form of the oxygen orbitals in the LTO phase

$$
\begin{aligned}
|p_{x'}\rangle &= |p_x\rangle - \frac{\delta}{\sqrt{2}}|p_z\rangle \\
|p_{y'}\rangle &= |p_y\rangle + \frac{\delta}{\sqrt{2}}|p_z\rangle \\
|p_{z'}\rangle &= |p_x\rangle + \frac{\delta}{\sqrt{2}}(|p_x\rangle - |p_y\rangle),
\end{aligned} \tag{A.8}
$$

where the $x'y'z'$ is a tetragonal coordinate system fixed to a tilted CuO_6 octahedron. Inserting the orbitals given by Eqs. (A.7) and (A.8) into Eq. (A.5), we obtain the DM vectors on the bonds ij and ik (see Fig. 2.3) in the form $\mathbf{D}_{ij} = (-d, d, 0)/\sqrt{2}$ and $\mathbf{D}_{ik} = (d, d, 0)/\sqrt{2}$, respectively, with

$$
d = \lambda\delta\frac{4\sqrt{2}}{\varepsilon_{zx}}t_{zx,p_z}(t_{x^2-y^2})^3\left\{\frac{1}{\varepsilon_{p_\sigma}^2}\left[\frac{1}{\varepsilon_{p_\sigma}}+\frac{1}{U}\right] + \frac{1}{U\varepsilon_{p_\sigma}\varepsilon_{p_z}} + \frac{1}{2(\varepsilon_{p_\sigma}+\varepsilon_{p_z})}\left[\frac{1}{\varepsilon_{p_\sigma}}+\frac{1}{\varepsilon_{p_z}}\right]\right\}. \tag{A.9}
$$

Here, the relation $\varepsilon_{yz} = \varepsilon_{zx}$ was used, ε_{p_σ} is the energy of the $2p_\sigma$ orbital (σ is x or y for a bond along the x or y tetragonal direction), and t_{zx,p_z} is the hopping between the $3d_{zx}$ copper orbital and the $2p_z$ oxygen orbital.

Appendix B

Derivation of the magnetic susceptibilities

This Appendix is devoted to the derivation of the expression (2.51) for the zero-field magnetic susceptibilities, χ_δ, when the magnetic field is applied along one of the orthorhombic axes, $\delta = a, b, c$.

The zero-field magnetic susceptibility is defined as

$$\chi_\delta = \frac{1}{\beta V} \frac{\partial^2}{\partial B_\delta^2} \ln \mathcal{Z}[\mathbf{B}]|_{\mathbf{B}=0}, \tag{B.1}$$

where $\mathcal{Z}[\mathbf{B}]$ is the Euclidean partition function for the field $\mathbf{n}$,

$$\mathcal{Z}[\mathbf{B}] = \int \mathcal{D}\mathbf{n}\ \delta(\mathbf{n}^2 - 1)\ e^{-\mathcal{S}[\mathbf{B}]}, \tag{B.2}$$

with $\mathcal{S}$ being the action for the field $\mathbf{n}$, given by Eq. (2.47). By taking the derivatives in the above expression for the susceptibilities, we find the susceptibilities in terms of the correlation functions for the components of the $\mathbf{n}$ field

$$\chi_\delta = -\frac{1}{\beta V} \left[\left\langle \frac{\partial \mathcal{S}}{\partial B_\delta} \right\rangle_{\mathbf{B}=0} \right]^2 + \frac{1}{\beta V} \left\langle \left(\frac{\partial \mathcal{S}}{\partial B_\delta} \right)^2 \right\rangle_{\mathbf{B}=0} - \frac{1}{\beta V} \left\langle \frac{\partial^2 \mathcal{S}}{\partial B_\delta^2} \right\rangle_{\mathbf{B}=0}, \tag{B.3}$$

where $\langle\ \ \rangle$ denotes the correlator calculated with the partition function (B.2). In order to obtain the explicit form of the susceptibilities in terms of the correlation functions for the $\mathbf{n}$ field, it is convenient to rewrite the action (2.47), by performing

partial integrations, in the following equivalent form

$$\mathcal{S} = \frac{1}{2}\int d\tau d^2\mathbf{r}\int d\tau' d^2\mathbf{r}'\delta(\mathbf{r}-\mathbf{r}')\delta(\tau-\tau')n_\alpha(\mathbf{r},\tau)\Theta_{\alpha\beta}(\mathbf{r},\tau;\mathbf{r}',\tau')n_\beta(\mathbf{r}',\tau') + \int d\tau d^2\mathbf{r} J_\alpha n_\alpha, \tag{B.4}$$

with

$$\Theta_{\alpha\beta}(\mathbf{r},\tau;\mathbf{r}',\tau') \equiv \frac{1}{\tilde{g}c}\left[-(\partial^2_{\tau'} + c^2\nabla^2_{\mathbf{r}'} + \mathbf{B}^2 - m_\alpha^2)\delta_{\alpha\beta} - 2i\epsilon_{\alpha\beta\gamma}B_\gamma\partial_{\tau'} + B_\alpha B_\beta\right],$$
$$J_\alpha \equiv \frac{8S}{\tilde{g}c}\epsilon_{\alpha\beta\gamma}B_\beta D_{+\gamma}. \tag{B.5}$$

We now expand the local staggered magnetization about its ground state, $\mathbf{n} = \bar{\mathbf{n}} + \boldsymbol{\sigma}_0$, with $\langle\mathbf{n}\rangle \equiv \boldsymbol{\sigma}_0$, being the magnetization in the ground state of the system. Then, the action acquires the form

$$\begin{aligned}\mathcal{S} &= \frac{1}{2}\int d\mathbf{x}\int d\mathbf{x}'\delta(\mathbf{x}-\mathbf{x}')n_\alpha(\mathbf{x})\Theta_{\alpha\beta}(\mathbf{x};\mathbf{x}')n_\beta(\mathbf{x}') + \int d\mathbf{x}\ \mathbf{J}\cdot\mathbf{n} \\ &- \frac{\beta V}{2\tilde{g}c}(\boldsymbol{\sigma}_0\times\mathbf{B})^2 + \frac{\beta V}{2}\mathbf{J}\cdot\boldsymbol{\sigma}_0,\end{aligned} \tag{B.6}$$

where we renamed $\bar{\mathbf{n}} \to \mathbf{n}$, and shortened the notation by introducing $\mathbf{x} \equiv (\mathbf{r},\tau)$. The derivative of the previous action with respect to the magnetic field B_δ reads

$$\begin{aligned}\frac{\partial\mathcal{S}}{\partial B_\delta} &= \frac{1}{2}\int d\mathbf{x}\int d\mathbf{x}'\delta(\mathbf{x}-\mathbf{x}')n_\alpha(\mathbf{x})\frac{\partial\Theta_{\alpha\beta}(\mathbf{x};\mathbf{x}')}{\partial B_\delta}n_\beta(\mathbf{x}') + \frac{4S}{\tilde{g}c}\epsilon_{\alpha\delta\gamma}D_{+\gamma}\int d\mathbf{x}\, n_\alpha(\mathbf{x}) \\ &- \frac{\beta V}{\tilde{g}c}[\boldsymbol{\sigma}_0^2 B_\delta - \sigma_{0\delta}(\boldsymbol{\sigma}_0\cdot\mathbf{B})] + \beta V\frac{4S}{\tilde{g}c}\epsilon_{\alpha\delta\gamma}\sigma_{0\alpha}D_{+\gamma},\end{aligned} \tag{B.7}$$

with the derivative of the kernel Θ given by

$$\frac{\partial\Theta_{\alpha\beta}}{\partial B_\delta} = \frac{1}{\tilde{g}c}[-B_\delta\delta_{\alpha\beta} - 2i\epsilon_{\alpha\beta\delta}\partial_{\tau'} + \delta_{\alpha\delta}B_\beta + B_\alpha\delta_{\beta\delta}]. \tag{B.8}$$

Since the correlation function

$$\langle n_\alpha(\mathbf{x})n_\beta(\mathbf{x}')\rangle|_{\mathbf{B}=0} = \Theta^{-1}_{\alpha\beta}|_{\mathbf{B}=0} \equiv \tilde{g}cG_\alpha(\mathbf{x}-\mathbf{x}')\delta_{\alpha\beta} \tag{B.9}$$

is symmetric in the spin space, we obtain

$$\left\langle\frac{\partial\mathcal{S}}{\partial B_\delta}\right\rangle_{\mathbf{B}=0} = \beta V\frac{4S}{\tilde{g}c}\epsilon_{\alpha\delta\gamma}\sigma_{0\alpha}D_{+\gamma}. \tag{B.10}$$

Let us now calculate the second term in the expression (B.3) for the susceptibilities. It is easy to show that

$$\left\langle\left(\frac{\partial\mathcal{S}}{\partial B_\delta}\right)^2\right\rangle_{\mathbf{B}=0} = \left\langle\left(\frac{\partial\mathcal{S}}{\partial B_\delta}\right)^2_{\mathbf{B}=0}\right\rangle, \tag{B.11}$$

using the fact that the magnetic field is an external field, and thus not correlated. Straightforward calculations, using Eqs. (B.7) and (B.8), yield

$$\left(\frac{\partial \mathcal{S}}{\partial B_\delta}\right)^2_{\mathbf{B}=0} = -\frac{1}{\tilde{g}^2 c^2}\int d\mathbf{x}\int d\mathbf{x}'\int d\mathbf{x}''\int d\mathbf{x}'''\delta(\mathbf{x}-\mathbf{x}')\delta(\mathbf{x}''-\mathbf{x}''')$$
$$\epsilon_{\alpha\beta\delta}\epsilon_{\mu\nu\delta}n_\alpha(\mathbf{x})n_\mu(\mathbf{x}'')\partial_{\tau'}n_\beta(\mathbf{x}')\partial_{\tau'''}n_\nu(\mathbf{x}''') + \left(\frac{4S}{\tilde{g}c}\right)^2\epsilon_{\alpha\delta\gamma}\epsilon_{\beta\delta\mu}D_{+\gamma}D_{+\mu}$$
$$\times \int d\mathbf{x}\int d\mathbf{x}' n_\alpha(\mathbf{x})n_\beta(\mathbf{x}') + \left(\beta V\frac{4S}{\tilde{g}c}\epsilon_{\alpha\delta\gamma}\sigma_{0\alpha}D_{+\gamma}\right)^2 \equiv I_1 + I_2 + I_3. \tag{B.12}$$

The expectation value of the first term on the right-hand side in the previous equation, using Eq. (B.9), acquires the form

$$\begin{aligned}\langle I_1\rangle &= -\int d\mathbf{x}\int d\mathbf{x}'\int d\mathbf{x}''\int d\mathbf{x}'''\delta(\mathbf{x}-\mathbf{x}')\delta(\mathbf{x}''-\mathbf{x}''')\\ &\quad \epsilon_{\alpha\beta\delta}\epsilon_{\mu\nu\delta}\left\{\delta_{\alpha\nu}\delta_{\mu\beta}\partial_{\tau'''}G_\alpha(\mathbf{x}-\mathbf{x}''')\partial_{\tau'}G_\alpha(\mathbf{x}'-\mathbf{x}'')\right.\\ &+ \left.\delta_{\alpha\mu}\delta_{\beta\nu}G_\alpha(\mathbf{x}-\mathbf{x}'')\partial_{\tau'}\partial_{\tau'''}G_\alpha(\mathbf{x}'-\mathbf{x}''')\right\}.\end{aligned} \tag{B.13}$$

The previous form of the expectation value $\langle I_1\rangle$, after performing integrations over $\mathbf{x}'$ and $\mathbf{x}'''$, and partial integrations over the imaginary time variables, can be simplified to

$$\langle I_1\rangle = 2\int d\mathbf{x}\int d\mathbf{x}'\epsilon_{\alpha\beta\delta}\epsilon_{\alpha\beta\delta}G_\alpha(\mathbf{x}-\mathbf{x}')\partial_\tau^2 G_\beta(\mathbf{x}-\mathbf{x}'). \tag{B.14}$$

Finally, by taking the Fourier transform, $\langle I_1\rangle$ acquires the form

$$\langle I_1\rangle = -4\sum_{\mathbf{q}}\omega_n^2 G_\alpha(\mathbf{q})G_\beta(\mathbf{q}), \qquad \alpha\neq\beta\neq\delta, \tag{B.15}$$

with $\mathbf{q}\equiv(\omega_n,\mathbf{k})$. The expectation value of the term I_2 in Eq. (B.12), is readily obtained by using Eq. (B.9), and reads

$$\langle I_2\rangle = \beta V\frac{16S^2}{\tilde{g}c}\epsilon_{\alpha\delta\gamma}\epsilon_{\alpha\delta\mu}D_{+\gamma}D_{+\mu}G_\alpha(\mathbf{q}=0). \tag{B.16}$$

Using Eqs. (B.11), (B.15), and (B.16), we obtain

$$\left\langle\left(\frac{\partial \mathcal{S}}{\partial B_\delta}\right)^2\right\rangle_{\mathbf{B}=0} = -4\sum_{\mathbf{q}}\omega_n^2 G_\alpha(\mathbf{q})G_\beta(\mathbf{q}) + \beta V\frac{16S^2}{\tilde{g}c}\epsilon_{\alpha\delta\gamma}\epsilon_{\alpha\delta\mu}D_{+\gamma}D_{+\mu}G_\alpha(\mathbf{q}=0)$$
$$+ \left(\beta V\frac{4S}{\tilde{g}c}\epsilon_{\alpha\delta\gamma}\sigma_{0\alpha}D_{+\gamma}\right)^2, \tag{B.17}$$

where in the first term on the right-hand side $\alpha \neq \beta \neq \delta$.

Let us now evaluate the last term in Eq. (B.3). The second derivative of the action (B.6) respect to the magnetic field reads

$$\frac{\partial^2 \mathcal{S}}{\partial B_\delta^2} = \frac{1}{\tilde{g}c} \int d\mathbf{x} \int d\mathbf{y} \delta(\mathbf{x}-\mathbf{y}) n_\alpha(\mathbf{x}) n_\beta(\mathbf{y}) [\delta_{\alpha\delta}\delta_{\beta\delta} - \delta_{\alpha\beta}] - \frac{\beta V}{\tilde{g}c}(\boldsymbol{\sigma}_0^2 - \sigma_{0\delta}^2), \quad \text{(B.18)}$$

which, using Eq. (B.9), yields,

$$\left\langle \frac{\partial^2 \mathcal{S}}{\partial B_\delta^2} \right\rangle_{\mathbf{B}=0} = -\sum_{\mathbf{q}} [G_\alpha(\mathbf{q}) + G_\beta(\mathbf{q})] - \frac{\beta V}{\tilde{g}c}(\boldsymbol{\sigma}_0^2 - \sigma_{0\delta}^2), \quad \text{(B.19)}$$

with $\alpha \neq \beta \neq \delta$ imposed in the first term on the right-hand side. Substituting Eqs. (B.10), (B.17), and (B.19) into Eq. (B.3), we obtain the form of the magnetic susceptibilities as given by Eq. (2.51), when the field is applied along one of the orthorhombic axes, $\delta = a, b, c$.

Appendix C

One-loop correction to the spin stiffness

In this appendix, we calculate the one-loop correction to the spin stiffness, which is given by the following integral

$$J \equiv \int \frac{d^2\mathbf{k}}{(2\pi)^2} \frac{(k^2)^2 + \mu^4}{(k^2 + m_\beta^2/2)(k^2+\mu^2)^3} \equiv J_1 + \mu^4 J_2, \tag{C.1}$$

with the integrals J_1 and J_2 defined as follows

$$\begin{aligned} J_1 &\equiv \int \frac{d^2\mathbf{k}}{(2\pi)^2} \frac{(k^2)^2}{(k^2 + m_\beta^2/2)(k^2+\mu^2)^3}, \\ J_2 &\equiv \int \frac{d^2\mathbf{k}}{(2\pi)^2} \frac{1}{(k^2 + m_\beta^2/2)(k^2+\mu^2)^3}, \end{aligned} \tag{C.2}$$

which can be simplified by using the following formulae

$$\begin{aligned} J_1 &= \frac{1}{2}\partial_x^2 \int \frac{d^2\mathbf{k}}{(2\pi)^2} \frac{(k^2)^2}{(k^2+y^2)(k^2+x)} \equiv \frac{1}{2}\partial_x^2 I_1, \\ J_2 &= \frac{1}{2}\partial_x^2 \int \frac{d^2\mathbf{k}}{(2\pi)^2} \frac{1}{(k^2+y^2)(k^2+x)} \equiv \frac{1}{2}\partial_x^2 I_2, \end{aligned} \tag{C.3}$$

with $x \equiv \mu^2$ and $y \equiv m_\beta/\sqrt{2}$.

Let us first consider the integral I_1. This integral, after integrating over the angular variable, acquires the form

$$I_1 = \frac{1}{4\pi}\left(k_F^2 - (x+y^2)\int_0^{k_F^2} d\alpha \frac{\alpha}{(\alpha+y^2)(\alpha+x)} - xy^2 \int_0^{k_F^2} d\alpha \frac{1}{(\alpha+y^2)(\alpha+x)} \right).$$

The integrals in the previous equation can be readily evaluated, and read

$$\begin{aligned}\int_0^{k_F^2} d\alpha \frac{\alpha}{(\alpha+y^2)(\alpha+x)} &= \frac{1}{x-y^2}\left[x\ln\left(1+\frac{k_F^2}{x}\right)-y^2\ln\left(1+\frac{k_F^2}{y^2}\right)\right] \\ \int_0^{k_F^2} d\alpha \frac{\alpha}{(\alpha+y^2)(\alpha+x)} &= \frac{1}{x-y^2}\left[\ln\left(1+\frac{k_F^2}{y^2}\right)-\ln\left(1+\frac{k_F^2}{x}\right)\right]. \quad \text{(C.4)}\end{aligned}$$

The integral I_1 is now readily obtained from the above expressions, and has the form

$$I_1 = \frac{k_F^2}{4\pi} - \frac{1}{x-y^2}\left[x^2\ln\left(1+\frac{k_F^2}{x}\right)-y^4\ln\left(1+\frac{k_F^2}{y^2}\right)\right]. \quad \text{(C.5)}$$

Finally, the second partial derivative respect to the variable x of the above integral yields the integral J_1 in the following form

$$J_1 = \frac{y^4}{4\pi(x-y^2)^3}\left[\ln\left(1+\frac{k_F^2}{y^2}\right)-\ln\left(1+\frac{k_F^2}{x}\right)\right]+\frac{k_F^2(k_F^2x-2xy^2-3k_F^2y^2)}{8\pi(x-y^2)^2(x+k_F^2)^2}. \quad \text{(C.6)}$$

The integral I_2, defined in Eq. (C.3), can be straightforwardly calculated, and reads

$$I_2 = \frac{1}{4\pi(x-y^2)}\left[\ln\left(1+\frac{k_F^2}{y^2}\right)-\ln\left(1+\frac{k_F^2}{x}\right)\right], \quad \text{(C.7)}$$

which, after taking the second partial derivative with respect to the variable x, yields the following form of the integral J_2

$$\begin{aligned}J_2 &= \frac{1}{4\pi(x-y^2)^3}\left[\ln\left(1+\frac{k_F^2}{y^2}\right)-\ln\left(1+\frac{k_F^2}{x}\right)\right]-\frac{k_F^2}{8\pi x(x-y^2)(x+k_F^2)} \\ &\times \left[2+\frac{(x-y^2)(2x+k_F^2)}{x(x+k_F^2)}\right]. \quad \text{(C.8)}\end{aligned}$$

Finally, by substituting Eqs. (C.6) and (C.8) into Eq. (C.1) and recalling that $x \equiv \mu^2$ and $y \equiv m_\beta/\sqrt{2}$, we obtain the one-loop correction to the spin stiffness, in the form given by Eq. (3.28).

Appendix D

Energy of a single vortex and of a vortex-antivortex pair

In this appendix we will calculate the energy of the topological defects in the $SO(3)$ NLσ model. Static solutions of the model obey the Laplace equation

$$\nabla^2 \Psi(\mathbf{r}) = 0. \tag{D.1}$$

A single-vortex solution centered at $\mathbf{R} = (X, Y)$ has the form

$$\Psi_{1v}(\mathbf{r}, \mathbf{R}) = \arctan\left(\frac{x - X}{y - Y}\right), \tag{D.2}$$

with energy given by

$$E[\Psi_{1v}] = \mathcal{N} c^2 \int d^2\mathbf{r} (\nabla \Psi_{1v})^2 = 2\pi \mathcal{N} c^2 \ln \frac{\ell}{a}.$$

A bound vortex-antivortex pair described by

$$\Psi_{2v} = \Psi_{1v}(\mathbf{r}, \mathbf{R}_1) - \Psi_{1v}(\mathbf{r}, \mathbf{R}_2), \tag{D.3}$$

with Ψ_{1v} given by Eq. (D.2), is also a solution of Eq. (D.1). The vortex-antivortex defect can be written in a more compact form as

$$\Psi_{2v} = \arctan\left\{\frac{[\mathbf{d} \times (\mathbf{r} - \mathbf{R})]_z}{(\mathbf{r} - \mathbf{R})^2 - \mathbf{d}^2/4}\right\},$$

where the center of mass and relative coordinate, respectively, are defined as

$$\mathbf{R} = \frac{1}{2}(\mathbf{R}_1 + \mathbf{R}_2), \qquad \mathbf{d} = \mathbf{R}_2 - \mathbf{R}_1.$$

In order to evaluate the energy of the vortex-antivortex pair

$$E[\Psi_{2v}] = \mathcal{N}c^2 \int d^2\mathbf{r}(\nabla\Psi_{2v})^2,$$

we use Eq. (D.3), which yields

$$E[\Psi_{2v}] = \mathcal{N}c^2(I_{11} + I_{22} - 2I_{12}), \tag{D.4}$$

where

$$I_{jj'} \equiv \int d^2\mathbf{r}(\nabla\Psi^{(j)})(\nabla\Psi^{(j')}).$$

and $\Psi^{(1,2)} \equiv \Psi_{1v}(\mathbf{r}, \mathbf{R}_{(1,2)})$. It can be readily shown that I_{11} and I_{22} are equal,

$$I_{11} = I_{22} = 2\pi \ln\frac{\ell}{a}. \tag{D.5}$$

The integral I_{12} is highly nontrivial. After some calculations, it can be expressed in the form

$$\begin{aligned} I_{12} &= \frac{1}{2}\int d^2\mathbf{r}\frac{1}{(\mathbf{r}-\mathbf{R}_1)^2} + \frac{1}{2}\int d^2\mathbf{r}\frac{1}{(\mathbf{r}-\mathbf{R}_2)^2} \\ &- \frac{1}{2}(\mathbf{R}_1-\mathbf{R}_2)^2\int d^2\mathbf{r}\frac{1}{(\mathbf{r}-\mathbf{R}_1)^2(\mathbf{r}-\mathbf{R}_2)^2}. \end{aligned} \tag{D.6}$$

The first two integrals on the right hand side of Eq. (D.6) are identical and equal to I_{11}, whereas the last one must be evaluated separately. Let us denote it as $I_{12}^{(3)}$. After regularization, it becomes

$$I_{12}^{(3)} = \int d^2\mathbf{r}\frac{1}{[(\mathbf{r}-\mathbf{R}_1)^2+a^2][(\mathbf{r}-\mathbf{R}_2)^2+a^2]}.$$

By introducing new coordinates with $\mathbf{r}-\mathbf{R}_2 \to \mathbf{r}$, the last integral acquires the form

$$I_{12}^{(3)} = \int d^2\mathbf{r}\frac{1}{[\mathbf{r}^2+a^2][(\mathbf{r}+\mathbf{d})^2+a^2]}. \tag{D.7}$$

In order to simplify Eq. (D.7), we introduce polar coordinates $x = r\cos\varphi, y = r\sin\varphi$

$$I_{12}^{(3)} = \int_0^\ell dr\frac{r}{r^2+a^2}\int_0^{2\pi}\frac{d\varphi}{r^2+2rd\cos(\varphi-\phi)+d^2+a^2},$$

where (d,ϕ) are polar coordinates of $\mathbf{d}$. Integrating over the angle φ, we obtain

$$I_{12}^{(3)} = \int_0^\ell dr\frac{r}{r^2+a^2}\frac{2\pi}{\sqrt{(r^2-d^2)^2+2a^2(r^2+d^2)+a^4}}.$$

After substituting $u = 1/(r^2 + a^2)$, the above integral reads

$$I_{12}^{(3)} = \pi \int_{1/a^2}^{1/(\ell^2+a^2)} \frac{du}{\sqrt{u^2 d^2 (d^2 + 2a^2) - 2ud^2 + 1}}.$$

Straightforward calculations give

$$\begin{aligned} I_{12}^{(3)} &= \frac{\pi}{d\sqrt{d^2 + 2a^2}} \ln \left\{ \frac{1}{4a^4} \left[d^3 + \sqrt{d^6 + 8a^6} \right] \right. \\ &\quad \left. \left[d + \sqrt{d^2 + 2a^2} \right] \right\} \approx \frac{4\pi}{d\sqrt{d^2 + 2a^2}} \ln \frac{d}{a}. \end{aligned} \tag{D.8}$$

Substitution of Eq. (D.8) into Eq. (D.6) yields

$$I_{12} = 2\pi \left[\ln \frac{\ell}{a} - \frac{d}{\sqrt{d^2 + 2a^2}} \ln \frac{d}{a} \right]. \tag{D.9}$$

After inserting the last relation together with Eq. (D.5) into Eq. (D.4), we finally obtain the energy of the vortex-antivortex pair

$$E[\Psi_{2v}] = \frac{4\pi d}{\sqrt{d^2 + 2a^2}} \mathcal{N} c^2 \ln \frac{d}{a} \approx 4\pi \mathcal{N} c^2 \ln \frac{d}{a}, \tag{D.10}$$

which shows that the energy of the defect pair is finite.

Appendix E

Dynamics of the fluctuations around the defect

Using the identities

$$\begin{aligned} \sigma^a\sigma^b &= \delta^{ab} + i\epsilon^{abc}\sigma^c, \\ \exp\left(\frac{i}{2}\boldsymbol{\sigma}\cdot\boldsymbol{\alpha}\right) &= \cos\frac{\alpha}{2} + i\frac{\boldsymbol{\sigma}\cdot\boldsymbol{\alpha}}{\alpha}\sin\frac{\alpha}{2}, \end{aligned}$$

where $\alpha \equiv |\boldsymbol{\alpha}|$, together with Eq. (4.14), one can show that

$$\begin{aligned} \partial_\mu g_s &= \frac{i}{2}m^a\sigma^a g_s\partial_\mu\Psi_v, \qquad \text{(E.1)} \\ \partial_\mu g_\varepsilon &= \frac{i}{2}\frac{\boldsymbol{\sigma}\cdot\boldsymbol{\varepsilon}}{\varepsilon}\partial_\mu\varepsilon g_\varepsilon + \frac{i\sigma^a}{\varepsilon}\left[\partial_\mu\varepsilon^a - \frac{\varepsilon^a(\boldsymbol{\varepsilon}\cdot\partial_\mu\boldsymbol{\varepsilon})}{\varepsilon^2}\right]\sin\frac{\varepsilon}{2}. \end{aligned}$$

Here ε stands for $|\boldsymbol{\varepsilon}|$. By inserting Eqs. (E.1) into the field A^a_μ given by (4.5), we obtain

$$A^a_\mu \equiv A^a_{\mu 1} + A^a_{\mu 2} + A^a_{\mu 3} + A^a_{\mu 4}, \qquad \text{(E.2)}$$

with

$$\begin{aligned} A^a_{\mu 1} &= \frac{1}{4}\mathrm{Tr}(\sigma^a g_\varepsilon^{-1} g_s^{-1}\sigma^b g_s g_\varepsilon)m^b\partial_\mu\Psi_v, \\ A^a_{\mu 2} &= \frac{1}{2\varepsilon}\mathrm{Tr}(\sigma^a g_\varepsilon^{-1}\sigma^b)\partial_\mu\varepsilon^b\sin\frac{\varepsilon}{2}, \\ A^a_{\mu 3} &= -\frac{1}{2}\mathrm{Tr}(\sigma^a g_\varepsilon^{-1}\sigma^b)\frac{\varepsilon^b(\boldsymbol{\varepsilon}\cdot\partial_\mu\boldsymbol{\varepsilon})}{\varepsilon^3}\sin\frac{\varepsilon}{2}, \\ A^a_{\mu 4} &= \frac{1}{4\varepsilon}\mathrm{Tr}(\sigma^a g_\varepsilon^{-1}\sigma^b\partial_\mu\varepsilon g_\varepsilon)\varepsilon^b. \end{aligned}$$

The parameter ε is small, $\varepsilon \ll 1$, because g_ε describes fluctuations around the defect. Using the properties of the Pauli matrices, we find

$$g_\varepsilon = 1 + \frac{i}{2}\boldsymbol{\sigma}\cdot\boldsymbol{\varepsilon} - \frac{1}{8}\varepsilon^2 + \mathcal{O}(\varepsilon^3),$$

which allows us to write

$$\begin{aligned}
A^a_{\mu 1} &= \frac{1}{4}\mathrm{Tr}\left\{\sigma^a\left(\cos\frac{\Psi_v}{2} - i\mathbf{m}\cdot\boldsymbol{\sigma}\sin\frac{\Psi_v}{2}\right)\sigma^b\right. \\
&\quad \left.\left(\cos\frac{\Psi_v}{2} + i\mathbf{m}\cdot\boldsymbol{\sigma}\sin\frac{\Psi_v}{2}\right)\right\} m^b\partial_\mu\Psi_v\left(1-\frac{\varepsilon^2}{4}\right) \\
&+ \frac{i}{8}\mathrm{Tr}\left\{\sigma^a\left(\cos\frac{\Psi_v}{2} - i\mathbf{m}\cdot\boldsymbol{\sigma}\sin\frac{\Psi_v}{2}\right)\sigma^b\right. \\
&\quad \left.\left(\cos\frac{\Psi_v}{2} + i\mathbf{m}\cdot\boldsymbol{\sigma}\sin\frac{\Psi_v}{2}\right)(\boldsymbol{\sigma}\cdot\boldsymbol{\varepsilon})\right\} m^b\partial_\mu\Psi_v \\
&- \frac{i}{8}\mathrm{Tr}\left\{\sigma^a(\boldsymbol{\sigma}\cdot\boldsymbol{\varepsilon})\left(\cos\frac{\Psi_v}{2} - i\mathbf{m}\cdot\boldsymbol{\sigma}\sin\frac{\Psi_v}{2}\right)\right. \\
&\quad \left.\sigma^b\left(\cos\frac{\Psi_v}{2} + i\mathbf{m}\cdot\boldsymbol{\sigma}\sin\frac{\Psi_v}{2}\right)\right\} m^b\partial_\mu\Psi_v \\
&+ \frac{1}{16}\mathrm{Tr}\left\{\sigma^a(\boldsymbol{\sigma}\cdot\boldsymbol{\varepsilon})\left(\cos\frac{\Psi_v}{2} - i\mathbf{m}\cdot\boldsymbol{\sigma}\sin\frac{\Psi_v}{2}\right)\right. \\
&\quad \left.\sigma^b\left(\cos\frac{\Psi_v}{2} + i\mathbf{m}\cdot\boldsymbol{\sigma}\sin\frac{\Psi_v}{2}\right)(\boldsymbol{\sigma}\cdot\boldsymbol{\varepsilon})\right\} m^b\partial_\mu\Psi_v.
\end{aligned}$$

After some algebra, the last equation acquires the form

$$\begin{aligned}
A^a_{\mu 1} &= \frac{1}{2}m^a\partial_\mu\Psi_v\left(1-\frac{\varepsilon^2}{4}\right) + \frac{1}{2}\epsilon^{abc}\varepsilon^b m^c\partial_\mu\Psi_v \\
&+ \frac{1}{4}\varepsilon^a\varepsilon^b m^b\partial_\mu\Psi_v - \frac{1}{8}\varepsilon^2 m^a\partial_\mu\Psi_v + \mathcal{O}(\varepsilon^3).
\end{aligned} \tag{E.3}$$

Analogously, one can show that

$$\begin{aligned}
A^a_{\mu 2} &= \frac{1}{2}\partial_\mu\varepsilon^a + \mathcal{O}(\varepsilon^3) \\
A^a_{\mu 3} &= -\frac{\varepsilon^a(\boldsymbol{\varepsilon}\cdot\partial_\mu\boldsymbol{\varepsilon})}{\varepsilon^2} + \mathcal{O}(\varepsilon^3) \\
A^a_{\mu 4} &= \frac{\varepsilon^a}{2\varepsilon}\partial_\mu\varepsilon + \mathcal{O}(\varepsilon^3).
\end{aligned} \tag{E.4}$$

By substituting Eqs. (E.3) and (E.4) into the field A^a_μ given by (E.2), and retaining

terms up to the second order in ε, we obtain

$$\begin{aligned} A^a_\mu &= \frac{1}{2}m^a\partial_\mu\Psi_v\left(1-\frac{\varepsilon^2}{2}\right)+\frac{1}{4}\varepsilon^a\varepsilon^b m^b\partial_\mu\Psi_v \\ &+ \frac{1}{2}\epsilon^{abc}\varepsilon^b m^c\partial_\mu\Psi_v+\frac{1}{2}\partial_\mu\varepsilon^a+\frac{1}{4}\epsilon^{abc}\varepsilon^b\partial_\mu\varepsilon^c, \end{aligned} \tag{E.5}$$

and

$$\begin{aligned} A^a_\mu A^a_\mu &= \frac{1}{4}(\partial_\mu\Psi_v)^2+\frac{1}{4}(\partial_\mu\boldsymbol{\varepsilon})^2+\frac{1}{2}m^a\partial_\mu\varepsilon^a\partial_\mu\Psi_v \\ &+ \frac{1}{4}\epsilon^{abc}\partial_\mu\varepsilon^a\varepsilon^b m^c\partial_\mu\Psi_v. \end{aligned} \tag{E.6}$$

Appendix F

Evaluation of the kernel

In this appendix we will express the kernel K defined by Eq. (4.42) as a functional integral. First, we divide the time interval $[0,t]$ into $(m-1)$ subintervals of length ϵ, so $t=(m-1)\epsilon$, and use $(m-1)$ completeness relations between the $(m-1)$ exponential functions,

$$\begin{aligned} & K(\mathbf{x},\boldsymbol{\alpha}^*;\mathbf{y},\boldsymbol{\beta};t) \equiv \langle \mathbf{x},\boldsymbol{\alpha}|e^{-\frac{i\hat{H}t}{\hbar}}|\mathbf{y},\boldsymbol{\beta}\rangle \\ = & \int d^2\mathbf{x}_{m-1}...\int d^2\mathbf{x}_1 \int \frac{d^2\boldsymbol{\zeta}_{m-1}}{\pi^{2N}}...\int \frac{d^2\boldsymbol{\zeta}_1}{\pi^{2N}} \\ & \langle \mathbf{x}_m\boldsymbol{\zeta}_m|e^{-\frac{i\hat{H}\epsilon}{\hbar}}|\mathbf{x}_{m-1}\boldsymbol{\zeta}_{m-1}\rangle \\ & \langle \mathbf{x}_{m-1}\boldsymbol{\zeta}_{m-1}|e^{-\frac{i\hat{H}\epsilon}{\hbar}}|\mathbf{x}_{m-2}\boldsymbol{\zeta}_{m-2}\rangle...\langle \mathbf{x}_1\boldsymbol{\zeta}_1|e^{-\frac{i\hat{H}\epsilon}{\hbar}}|\mathbf{x}_0\boldsymbol{\zeta}_0\rangle, \end{aligned}$$

where

$$\begin{aligned} & \mathbf{x}_m \equiv \mathbf{x}, \quad \mathbf{x}_0 \equiv \mathbf{y} \\ & \boldsymbol{\zeta}_m \equiv \boldsymbol{\alpha}, \quad \boldsymbol{\zeta}_0 \equiv \boldsymbol{\beta}. \end{aligned} \tag{F.1}$$

By inserting m completeness relations in the momentum representation into Eq. (F.1), we obtain

$$\begin{aligned} & K(\mathbf{x},\boldsymbol{\alpha}^*;\mathbf{y},\boldsymbol{\beta};t) = \left(\prod_{k=1}^{m-1} d^2\mathbf{x}_k \frac{d^2\boldsymbol{\zeta}_k}{\pi^{2N}}\right)\left(\prod_{k=1}^{m} d^2\mathbf{P}_k\right) \\ & \prod_{k=1}^{m}\langle \mathbf{x}_k\boldsymbol{\zeta}_k|e^{-\frac{i\hat{H}\epsilon}{\hbar}}|\mathbf{P}_k\boldsymbol{\zeta}_{k-1}\rangle\langle \mathbf{P}_k|\mathbf{x}_{k-1}\rangle. \end{aligned} \tag{F.2}$$

The matrix element $\langle \mathbf{x}_k\boldsymbol{\zeta}_k|e^{-\frac{i\hat{H}\epsilon}{\hbar}}|\mathbf{P}_k\boldsymbol{\zeta}_{k-1}\rangle$, $(k=1,...,m)$, can be evaluated using

that $\epsilon \ll t$. It reads

$$\langle \mathbf{x}_k \boldsymbol{\zeta}_k | e^{-\frac{i\hat{H}\epsilon}{\hbar}} | \mathbf{P}_k \boldsymbol{\zeta}_{k-1} \rangle = \langle \mathbf{x}_k | \mathbf{P}_k \rangle \langle \boldsymbol{\zeta}_k | \boldsymbol{\zeta}_{k-1} \rangle$$
$$\exp\left[-\frac{i\epsilon}{\hbar} H(\mathbf{x}_k, \mathbf{P}_k; \boldsymbol{\zeta}_k^*, \boldsymbol{\zeta}_{k-1}) \right], \tag{F.3}$$

where

$$H(\mathbf{x}_k, \mathbf{P}_k; \boldsymbol{\zeta}_k^*, \boldsymbol{\zeta}_{k-1}) \equiv \frac{\langle \mathbf{x}_k \boldsymbol{\zeta}_k | \hat{H} | \mathbf{P}_k \boldsymbol{\zeta}_{k-1} \rangle}{\langle \mathbf{x}_k | \mathbf{P}_k \rangle \langle \boldsymbol{\zeta}_k | \boldsymbol{\zeta}_{k-1} \rangle}.$$

Substituting the matrix element given by Eq. (F.3) into Eq. (F.2), recalling that

$$\langle \mathbf{P} | \mathbf{x} \rangle = \frac{1}{2\pi\hbar} \exp\left(-\frac{i}{\hbar} \mathbf{P} \cdot \mathbf{x} \right),$$

and using the properties of the overlap of coherent states, we find that the kernel acquires the form

$$K(\mathbf{x}, \boldsymbol{\alpha}^*; \mathbf{y}, \boldsymbol{\beta}; t) = \int \frac{d^2\mathbf{P}_m}{2\pi\hbar} \left(\prod_{l=1}^{m-1} \int \frac{d^2\mathbf{x}_l d^2\mathbf{P}_l}{2\pi\hbar} \frac{d^2\vec{\zeta}_l}{\pi^{2N}} \right)$$
$$\exp\left\{ \sum_{k=1}^{m} \frac{1}{2} \left[\boldsymbol{\zeta}_{k-1} \cdot (\boldsymbol{\zeta}_k^* - \boldsymbol{\zeta}_{k-1}^*) - \boldsymbol{\zeta}_k^* \cdot (\boldsymbol{\zeta}_k - \boldsymbol{\zeta}_{k-1}) \right] \right.$$
$$\left. + \frac{i}{\hbar} \left[\mathbf{P}_k (\mathbf{x}_k - \mathbf{x}_{k-1}) - \epsilon H(\mathbf{x}_k, \mathbf{P}_k; \boldsymbol{\zeta}_k^*, \boldsymbol{\zeta}_{k-1}) \right] \right\}. \tag{F.4}$$

In order to integrate over the momenta $\mathbf{P}_k$, we have to explicitly calculate $H(\mathbf{x}_k, \mathbf{p}_k; \boldsymbol{\zeta}_k^*, \boldsymbol{\zeta}_{k-1})$. Using the coherent state representation for the bath of harmonic oscillators, we find

$$H(\mathbf{x}_k, \mathbf{P}_k; \boldsymbol{\zeta}_k^*, \boldsymbol{\zeta}_{k-1}) = \frac{\mathbf{P}_k^2}{2M} + \sum_{nm,i=a,b} \hbar\omega_{nm} \zeta_{nm,i}^{k*} \zeta_{nm,i}^{k-1}$$
$$- \frac{\mathbf{P}_k}{M} \sum_{nm,pq} \left[\mathbf{D}_{nm,pq} \zeta_{pq,a}^{k*} \zeta_{nm,a}^{k-1} - \mathbf{D}_{pq,nm} \zeta_{nm,b}^{k-1} \zeta_{pq,b}^{k*} \right],$$

which, after insertion into Eq. (F.4) and integration over the momenta $\mathbf{P}_k$, yields

$$K(\mathbf{x}, \boldsymbol{\alpha}^*; \mathbf{y}, \boldsymbol{\beta}; t) = \left(\frac{M}{2i\pi\hbar} \right)^{m/2} \left(\prod_{l=1}^{m-1} \frac{d^2\mathbf{x}_l}{2\pi\hbar} \frac{d^2\boldsymbol{\zeta}_l}{\pi^{2N}} \right) \tag{F.5}$$
$$\exp\left\{ \sum_{k=1}^{m} \frac{1}{2} \left[\boldsymbol{\zeta}_{k-1} \cdot (\boldsymbol{\zeta}_k^* - \boldsymbol{\zeta}_{k-1}^*) - \boldsymbol{\zeta}_k^* \cdot (\boldsymbol{\zeta}_k - \boldsymbol{\zeta}_{k-1}) \right] \right.$$
$$\left. - \frac{i\epsilon}{\hbar} \sum_{nm,i} \hbar\omega_{nm} \zeta_{nm,i}^{k*} \zeta_{nm,i}^{k-1} + \frac{iM\epsilon}{2\hbar} \left(\mathbf{h}_k + \frac{\mathbf{x}_k - \mathbf{x}_{k-1}}{\epsilon} \right)^2 \right\},$$

with

$$\mathbf{h}_k \equiv \frac{\hbar}{M} \sum_{nm,pq} \left(\mathbf{D}_{nm,pq} \zeta^{k*}_{pq,a} \zeta^{k-1}_{nm,a} - \mathbf{D}_{pq,nm} \zeta^{k-1}_{nm,b} \zeta^{k*}_{pq,b} \right).$$

Now, we consider the continuum limit, $\epsilon \to 0$, of the last equation. Using the boundary conditions (F.1), the first term in the exponential in (F.5) becomes

$$\begin{aligned}
& \exp\left\{ \sum_{k=1}^{m} \frac{1}{2} \left[\boldsymbol{\zeta}_{k-1} \cdot (\boldsymbol{\zeta}^*_k - \boldsymbol{\zeta}^*_{k-1}) - \boldsymbol{\zeta}^*_k \cdot (\boldsymbol{\zeta}_k - \boldsymbol{\zeta}_{k-1}) \right] \right\} \\
= \quad & \exp\left\{ \frac{1}{2} \sum_{k=0}^{m-1} \boldsymbol{\zeta}_k \cdot (\boldsymbol{\zeta}^*_{k+1} - \boldsymbol{\zeta}^*_k) - \frac{1}{2} \sum_{k=1}^{m} \boldsymbol{\zeta}^*_k \cdot (\boldsymbol{\zeta}_k - \boldsymbol{\zeta}_{k-1}) \right\} \\
= \quad & \exp\left\{ \frac{1}{2} [\boldsymbol{\zeta}_0 \cdot (\boldsymbol{\zeta}^*_1 - \boldsymbol{\zeta}^*_0) - \boldsymbol{\zeta}^*_m \cdot (\boldsymbol{\zeta}_m - \boldsymbol{\zeta}_{m-1})] \right\} \\
& \exp\left\{ \frac{1}{2} \sum_{k=1}^{m-1} [\boldsymbol{\zeta}_k \cdot (\boldsymbol{\zeta}^*_{k+1} - \boldsymbol{\zeta}^*_k) - \boldsymbol{\zeta}^*_k \cdot (\boldsymbol{\zeta}_k - \boldsymbol{\zeta}_{k-1})] \right\} \\
\to \quad & \exp\left(-\frac{1}{2} |\boldsymbol{\beta}|^2 - \frac{1}{2} |\boldsymbol{\alpha}|^2 \right) \exp\left\{ \frac{1}{2} \boldsymbol{\beta} \cdot \boldsymbol{\zeta}^*(0) + \frac{1}{2} \boldsymbol{\alpha}^* \cdot \boldsymbol{\zeta}(t) \right\} \\
& \exp\left\{ \frac{1}{2} \int_0^t dt' (\boldsymbol{\zeta} \cdot \dot{\boldsymbol{\zeta}}^* - \boldsymbol{\zeta}^* \cdot \dot{\boldsymbol{\zeta}}) \right\}.
\end{aligned}$$

The other terms in Eq. (F.5) can be trivially written in the continuum limit, yielding then Eq. (4.43).

Appendix G

Initial density matrix for the bath in the coherent state representation

In this appendix, we evaluate the matrix elements of the initial density matrix for the bath in the coherent state representation

$$\rho_B(\boldsymbol{\beta}^*, \boldsymbol{\beta}', 0) = \langle \boldsymbol{\beta} | \hat{\rho}_B(0) | \boldsymbol{\beta}' \rangle,$$

with

$$\hat{\rho}_B(0) = \frac{1}{Z} \prod_{pq} e^{-U\omega_{pq}(\hat{a}^\dagger_{pq}\hat{a}_{pq} + \hat{b}^\dagger_{pq}\hat{b}_{pq})},$$

where the partition function reads

$$Z \equiv \mathrm{Tr}\left[e^{-U\sum_{pq}\omega_{pq}(\hat{a}^\dagger_{pq}\hat{a}_{pq} + \hat{b}^\dagger_{pq}\hat{b}_{pq})}\right] = \prod_{pq}\left(1 - e^{-\frac{\hbar\omega_{pq}}{k_B T}}\right)^{-2}.$$

Since the baths a and b are not coupled, the total density matrix is the product

$$\rho_B(\boldsymbol{\beta}^*, \boldsymbol{\beta}', 0) = \rho_{B,a}(\boldsymbol{\beta}^*_a, \boldsymbol{\beta}'_a, 0)\rho_{B,b}(\boldsymbol{\beta}^*_b, \boldsymbol{\beta}'_b, 0)$$

of the density matrices $\rho_{B,a}$ and $\rho_{B,a}$ for the baths a and b, respectively, given by

$$\rho_{B,a}(\boldsymbol{\beta}^*_a, \boldsymbol{\beta}'_a, 0) = \frac{1}{Z_a} \prod_{pq} \langle \beta_{pq,a} | e^{-U\omega_{pq}\hat{a}^\dagger_{pq}\hat{a}_{pq}} | \beta'_{pq,a} \rangle$$

for the bath a, and analogously for the bath b, with the partition function

$$Z_b = Z_a = \mathrm{Tr}\left[e^{-U\sum_{pq}\omega_{pq}(\hat{a}^\dagger_{pq}\hat{a}_{pq})}\right] = \prod_{pq}\left(1 - e^{-\frac{\hbar\omega_{pq}}{k_B T}}\right)^{-1}.$$

We will evaluate the previous matrix element by inserting two unity operators in the occupation number representation for the bath a (in the following, to simplify notation we omit the index a in the $\boldsymbol{\beta}$, $\boldsymbol{\beta}'$ and $\bar{n}$)

$$\begin{aligned}\rho_{B,a}(\boldsymbol{\beta}^*, \boldsymbol{\beta}', 0) &= \frac{1}{Z_a}\prod_{pq}\langle\beta_{pq}|e^{-U\omega_{pq}\hat{a}^\dagger_{pq}\hat{a}_{pq}}|\beta'_{pq}\rangle \qquad \text{(G.1)}\\ &= \frac{1}{Z_a}\prod_{pq}\sum_{n_{pq},n'_{pq}}\langle\beta_{pq}|n_{pq}\rangle \\ &\quad \langle n_{pq}|e^{-U\omega_{pq}\hat{a}^\dagger_{pq}\hat{a}_{pq}}|n'_{pq}\rangle\langle n'_{pq}|\beta'_{pq}\rangle.\end{aligned}$$

Now, we use the scalar product of the states which define the coherent state and occupation number representations

$$\langle\beta_{pq}|n_{pq}\rangle = \frac{(\beta^*_{pq})^{n_{pq}}}{\sqrt{n_{pq}!}}e^{-\frac{|\beta_{pq}|^2}{2}}.$$

Substituting the above expression into Eq. (G.1), we obtain

$$\begin{aligned}\rho_{B,a}(\boldsymbol{\beta}^*, \boldsymbol{\beta}', 0) &= \frac{1}{Z_a}\prod_{pq}\exp\left(-\frac{|\beta_{pq}|^2}{2} - \frac{|\beta'_{pq}|^2}{2}\right) \\ &\quad \sum_{n_{pq}}\frac{1}{n_{pq}!}\left\{\exp\left(-\frac{\hbar\omega_{pq}}{k_B T}\right)\beta^*_{pq}\beta'_{pq}\right\}^{n_{pq}} \\ &= \frac{1}{Z_a}\prod_{pq}\exp\left(-\frac{|\beta_{pq}|^2}{2} - \frac{|\beta'_{pq}|^2}{2}\right) \\ &\quad \exp\left[\beta^*_{pq}\beta'_{pq}\exp(-U\omega_{pq})\right]. \qquad \text{(G.2)}\end{aligned}$$

Appendix H

Equations of motion

Our next step is to solve equations of motion (4.49). In order to achieve this aim, we introduce the ansatz

$$\begin{aligned}
\zeta_{nm}(\tau) &= e^{-i\omega_{nm}\tau}[\beta_{nm} + \sum_{kl\neq nm} W_{nm,kl}(\tau)\beta_{kl}], \\
\zeta^*_{nm}(\tau) &= e^{i\omega_{nm}\tau}[\alpha^*_{nm}e^{-i\omega_{nm}t} \\
&+ \sum_{kl\neq nm} \tilde{W}_{nm,kl}(\tau)e^{-i\omega_{kl}t}\alpha^*_{kl}],
\end{aligned} \tag{H.1}$$

where the functionals W and $\tilde{W}$ will be determined from the equations of motion and $0 \leq \tau \leq t$. By substituting the first time derivative of Eqs. (H.1) into the equations of motion (4.49), we obtain the expressions which determine the time evolution of the functionals W and $\tilde{W}$

$$\dot{W}_{nm,kl} = W^0_{nm,kl} + \sum_{pq} W^0_{nm,pq}W_{pq,kl},$$

$$\dot{\tilde{W}}_{nm,kl} = -\tilde{W}^0_{nm,kl} - \sum_{pq} \tilde{W}^0_{nm,pq}\tilde{W}_{pq,kl},$$

with

$$\begin{aligned}
W^0_{nm,kl}[\mathbf{x},\tau] &= i\dot{\mathbf{x}}\mathbf{D}_{kl,nm}e^{i(\omega_{nm}-\omega_{kl})\tau}, \\
\tilde{W}^0_{nm,kl}[\mathbf{x},\tau] &= i\dot{\mathbf{x}}\mathbf{D}_{nm,kl}e^{-i(\omega_{nm}-\omega_{kl})\tau}.
\end{aligned} \tag{H.2}$$

Notice that $\tilde{W}^0_{nm,kl} = -W^{0*}_{nm,kl}$. Because W and $\tilde{W}$ must satisfy the boundary conditions $W(\mathbf{x},0) = 0$ and $\tilde{W}(\mathbf{x},t) = 0$, we have

$$\begin{aligned} W_{nm,kl}[\mathbf{x},\tau] &= \int_0^\tau dt' W^0_{nm,kl}[\mathbf{x},t'] \\ &+ \sum_{pq} \int_0^\tau dt' W^0_{nm,pq}[\mathbf{x},t'] W_{pq,kl}[\mathbf{x},t'], \\ \tilde{W}_{nm,kl}[\mathbf{x},\tau] &= \int_\tau^t dt' \tilde{W}^0_{nm,kl}[\mathbf{x},t'] \\ &+ \sum_{pq} \int_\tau^t dt' \tilde{W}^0_{nm,pq}[\mathbf{x},t'] \tilde{W}_{pq,kl}[\mathbf{x},t'], \end{aligned} \tag{H.3}$$

which, using the Born approximation, acquires the form

$$\begin{aligned} W_{nm,kl}[\mathbf{x},\tau] &= \int_0^\tau dt' W^0_{nm,kl}[\mathbf{x},t'] \\ + \sum_{pq} \int_0^\tau dt' W^0_{nm,pq}[\mathbf{x},t'] &\int_0^{t'} dt'' W^0_{pq,kl}[\mathbf{x},t'], \end{aligned}$$

$$\begin{aligned} \tilde{W}_{nm,kl}[\mathbf{x},\tau] &= \int_\tau^t dt' \tilde{W}^0_{nm,kl}[\mathbf{x},t'] \\ + \sum_{pq} \int_\tau^t dt' \tilde{W}^0_{nm,pq}[\mathbf{x},t'] &\int_{t'}^t dt'' \tilde{W}^0_{pq,kl}[\mathbf{x},t']. \end{aligned} \tag{H.4}$$

The functions γ appearing in Eq. (4.46) obey the equations of motion (4.49) with the boundary conditions (4.48). We solve them by introducing the ansatz

$$\begin{aligned} \gamma_{nm}(\tau) &= e^{-i\omega_{nm}\tau}[\alpha_{nm} e^{i\omega_{nm}t} \\ &+ \sum_{kl\neq nm} \bar{W}_{nm,kl}(\tau)\alpha_{kl} e^{i\omega_{kl}t}], \\ \gamma^*_{nm}(\tau) &= e^{i\omega_{nm}\tau}[\beta'^*_{nm} + \sum_{kl\neq nm} \tilde{\bar{W}}_{nm,kl}(\tau)\beta'^*_{kl}], \end{aligned} \tag{H.5}$$

with the conditions $\bar{W}(t) = 0$ and $\tilde{\bar{W}}(0) = 0$. By inserting this ansatz into the corresponding equations of motion, we find, after some algebra,

$$\begin{aligned}
\tilde{\bar{W}}_{nm,kl}[\mathbf{x},\tau] &= \int_0^\tau dt' \tilde{\bar{W}}^0_{nm,kl}[\mathbf{x},t'] \\
&+ \sum_{pq} \int_0^\tau dt' \tilde{\bar{W}}^0_{nm,pq}[\mathbf{x},t'] \tilde{\bar{W}}_{pq,kl}[\mathbf{x},t'], \\
\bar{W}_{nm,kl}[\mathbf{x},\tau] &= \int_\tau^t dt' \bar{W}^0_{nm,kl}[\mathbf{x},t'] \\
&+ \sum_{pq} \int_\tau^t dt' \bar{W}^0_{nm,pq}[\mathbf{x},t'] \bar{W}_{pq,kl}[\mathbf{x},t'],
\end{aligned} \tag{H.6}$$

with

$$\tilde{\bar{W}}^0_{nm,kl} = W^{0*}_{nm,kl}, \qquad \bar{W}^0_{nm,kl} = \tilde{W}^{0*}_{nm,kl}.$$

The boundary values of the functionals obey the relations

$$\bar{W}_{nm,kl}[\mathbf{x},0] = \tilde{W}^*_{nm,kl}[\mathbf{x},0],$$

$$\tilde{\bar{W}}_{nm,kl}[\mathbf{x},t] = W^*_{nm,kl}[\mathbf{x},t], \tag{H.7}$$

which will be used later. From Eqs. (H.1) and (H.5) the boundary terms read

$$\begin{aligned}
\zeta_{nm}(t) &= \beta_{nm} e^{-i\omega_{nm}t} + \sum W_{nm,kl}(\mathbf{x},t) e^{-i\omega_{nm}t} \beta_{kl}, \\
\zeta^*_{nm}(0) &= \alpha^*_{nm} e^{-i\omega_{nm}t} + \sum \tilde{W}_{nm,kl}(\mathbf{x},0) e^{-i\omega_{kl}t} \alpha^*_{kl}, \\
\gamma_{nm}(0) &= \alpha_{nm} e^{i\omega_{nm}t} + \sum \bar{W}_{nm,kl}(\mathbf{y},0) e^{i\omega_{kl}t} \alpha_{kl}, \\
\gamma^*_{nm}(t) &= \beta'^*_{nm} e^{i\omega_{nm}t} + \sum \tilde{\bar{W}}_{nm,kl}(\mathbf{y},t) e^{i\omega_{nm}t} \beta'^*_{kl}.
\end{aligned} \tag{H.8}$$

Appendix I

Evaluation of $\Gamma_{nm,nm}$

In this appendix we evaluate the diagonal elements of the matrix $\Gamma = \Gamma^a + \Gamma^b$, where the elements $\Gamma^a_{nm,nm}$ are given by

$$\begin{aligned}\Gamma^a_{nm,nm} &= \frac{1}{2}\left[W_{nm,nm}[\mathbf{x},t] + \tilde{W}_{nm,nm}[\mathbf{x},0] + \tilde{W}^*_{nm,nm}[\mathbf{y},0] + W^*_{nm,nm}[\mathbf{y},t]\right] \\ &+ \frac{1}{4}\sum_{pq}\left[\tilde{W}_{nm,pq}[\mathbf{x},0] + W_{pq,nm}[\mathbf{x},t]\right]\left[\tilde{W}^*_{nm,pq}[\mathbf{y},0] + W^*_{pq,nm}[\mathbf{y},t]\right],\end{aligned} \tag{I.1}$$

and the ones of matrix Γ^b are obtained from the latter by the substitution $\mathbf{D}_{nm,kl} \to -\mathbf{D}_{kl,nm} = -\mathbf{D}^*_{nm,kl}$. Using the Born approximation for the functionals W and $\tilde{W}$, given by Eq. (H.4), and the form of the functionals W^0 and $\tilde{W}^0$, defined after Eq. (H.1), we find

$$\begin{aligned}&W_{nm,nm}[\mathbf{x},t] = -\sum_{\mu,\nu,pq}\int_0^t dt'\int_0^t dt''\theta(t'-t'')\dot{x}^\mu(t')\dot{x}^\nu(t'')D^{\mu*}_{nm,pq}D^{\nu}_{nm,pq} \\ \times\ & e^{i(\omega_{nm}-\omega_{pq})(t'-t'')} \\ &\tilde{W}_{nm,nm}[\mathbf{x},0] = -\sum_{\mu,\nu,pq}\int_0^t dt'\int_0^t dt''\theta(t''-t')\dot{x}^\mu(t')\dot{x}^\nu(t'')D^{\mu}_{nm,pq}D^{\nu*}_{nm,pq} \\ \times\ & e^{i(\omega_{nm}-\omega_{pq})(t''-t')} = W_{nm,nm}[\mathbf{x},t].\end{aligned} \tag{I.2}$$

Using Eq. (H.3), as well as its complex conjugate evaluated at $\mathbf{y}$ and retaining only the terms quadratic in the coupling constants, we can write the last term in

Eq. (I.1) as

$$\begin{aligned}
&\frac{1}{4}\sum_{pq}[\tilde{W}_{nm,pq}(\mathbf{x},0)+W_{pq,nm}(\mathbf{x},t)][\tilde{W}^{*}_{nm,pq}(\mathbf{y},0)+W^{*}_{pq,nm}(\mathbf{y},t)]\\
&\simeq \frac{1}{4}\int_0^t dt'\int_0^t dt''\left[\tilde{W}^{0}_{nm,pq}[\mathbf{x},t']+W^{0}_{pq,nm}[\mathbf{x},t']\right]\left[\tilde{W}^{0*}_{nm,pq}[\mathbf{y},t'']+W^{0*}_{pq,nm}[\mathbf{y},t'']\right]\\
&=\sum_{\mu,\nu,pq}\int_0^t dt'\int_0^t dt''\dot{x}^{\mu}(t')\dot{y}^{\nu}(t'')D^{\mu}_{nm,pq}D^{\nu*}_{nm,pq}e^{i(\omega_{pq}-\omega_{nm})(t'-t'')}\\
=&\int_0^t dt'\int_0^t dt''\theta(t'-t'')D^{\mu}_{nm,pq}D^{\nu*}_{nm,pq}\left(\dot{x}^{\mu}(t')\dot{y}^{\nu}(t'')e^{i(\omega_{pq}-\omega_{nm})(t'-t'')}\right.\\
&\left.+\dot{x}^{\mu}(t'')\dot{y}^{\nu}(t')e^{-i(\omega_{pq}-\omega_{nm})(t'-t'')}\right). \qquad \text{(I.3)}
\end{aligned}$$

Substituting Eqs. (I.2) and (I.3) into Eq. (I.1), we obtain the diagonal elements of the matrix Γ^{a}, in the lowest order in the coupling constants

$$\begin{aligned}
\Gamma^{a}_{nm,nm} &= -\sum_{\mu,\nu,pq}\int_0^t dt'\int_0^t dt''\theta(t'-t'')[\dot{x}^{\mu}(t')-\dot{y}^{\mu}(t')]\left[\dot{x}^{\nu}(t'')D^{\mu*}_{nm,pq}D^{\nu}_{nm,pq}\right.\\
&\times\ e^{i(\omega_{nm}-\omega_{pq})(t'-t'')}-\dot{y}^{\nu}(t'')D^{\mu}_{nm,pq}D^{\nu*}_{nm,pq}e^{-i(\omega_{nm}-\omega_{pq})(t'-t'')}\Big], \qquad \text{(I.4)}
\end{aligned}$$

yielding the diagonal elements of the matrix Γ

$$\begin{aligned}
\Gamma_{nm,nm} &= -\sum_{\mu,\nu,pq}\int_0^t dt'\int_0^t dt''\theta(t'-t'')\left(D^{\mu}_{nm,pq}D^{\nu*}_{nm,pq}+D^{\mu*}_{nm,pq}D^{\nu}_{nm,pq}\right)\\
&\times\ [\dot{x}^{\mu}(t')-\dot{y}^{\mu}(t')]\left[\dot{x}^{\nu}(t'')e^{i(\omega_{nm}-\omega_{pq})(t'-t'')}-\dot{y}^{\nu}(t'')e^{-i(\omega_{nm}-\omega_{pq})(t'-t'')}\right]. \qquad \text{(I.5)}
\end{aligned}$$

Appendix J

Evaluation of coupling constants

In this appendix we calculate the coupling constants

$$\mathbf{G}^*_{km,k'l} = \int d^2\mathbf{r}\eta^*_{k'l}\nabla\eta_{km}, \tag{J.1}$$

where the wave functions are given by

$$\eta_{km} = \sqrt{\frac{k}{2\ell}}\left[H^{(1)}_m(kr) + e^{-2i\delta_m}H^{(2)}_m(kr)\right]e^{im\vartheta}, \qquad (m > 0). \tag{J.2}$$

By expressing the gradient operator in polar coordinates we find that

$$\begin{aligned}
G^{x*}_{km,k'l} &= \pi\delta_{m-l,1}\int_0^\infty drr[R_l(k'r)S_m(kr) - mR_l(k'r)F_m(kr)] \\
&+ \pi\delta_{m-l,-1}\int_0^\infty drr[R_l(k'r)S_m(kr) + mR_l(k'r)F_m(kr)], \\
G^{y*}_{km,k'l} &= i\pi\delta_{m-l,1}\int_0^\infty drr[R_l(k'r)S_m(kr) + mR_l(k'r)F_m(kr)] \\
&- i\pi\delta_{m-l,-1}\int_0^\infty drr[R_l(k'r)S_m(kr) - mR_l(k'r)F_m(kr)],
\end{aligned} \tag{J.3}$$

where

$$
\begin{aligned}
R_l(kr) &= \sqrt{\frac{k}{2\ell}}[H_l^{(2)}(kr) + e^{2i\delta_l} H_l^{(1)}(kr)], && \text{(J.4)}\\
S_l(kr) &= \frac{k}{2}\sqrt{\frac{k}{2\ell}}[H_{l-1}^{(1)}(kr) + e^{-2i\delta_l} H_{l-1}^{(2)}(kr) - H_{l+1}^{(1)}(kr) + \\
&+ e^{-2i\delta_l} H_{l+1}^{(2)}(kr)], && \text{(J.5)}\\
F_l(kr) &= \frac{l}{r}\sqrt{\frac{k}{2\ell}}[H_l^{(1)}(kr) + e^{-2i\delta_l} H_l^{(2)}(kr)]. && \text{(J.6)}
\end{aligned}
$$

In evaluating the expression (J.3) one can use the asymptotic form of the Hankel functions

$$
\begin{aligned}
H_m^{(1)}(kr) &= \sqrt{\frac{2}{\pi kr}} e^{ikr} e^{-i\frac{\pi}{2}(m+1/2)},\\
H_m^{(2)}(kr) &= \sqrt{\frac{2}{\pi kr}} e^{-ikr} e^{i\frac{\pi}{2}(m+1/2)}.
\end{aligned}
$$

However, the terms coming from $F_m(kr)$ would then be divergent at $r = 0$. This divergence is an artifact of approximating up to $r = 0$ the true solution of the scattering problem (4.22) with the functions (J.2). At small r indeed a better approximation for the radial part of the functions η_{km} is provided by the Bessel functions $J_m(kr)$, which are regular at $r = 0$. Then we find that

$$
\begin{aligned}
\int_0^\infty dr r H_\nu^{(1,2)}(k'r) H_\mu^{(1,2)}(kr) &= \frac{2e^{\pm i\pi(\mu+\nu+1)/2}}{\pi\sqrt{kk'}}\left(\pi\delta(k+k') \pm \mathcal{P}\frac{1}{k+k'}\right),\\
\int_0^\infty dr r H_\nu^{(1)}(k'r) H_\mu^{(2)}(kr) &= \frac{2e^{i\pi(\mu-\nu)/2}}{\pi\sqrt{kk'}}\left(\pi\delta(k-k') + \mathcal{P}\frac{1}{k-k'}\right),\\
\int_0^\infty dr J_{m+1}(k'r) J_m(kr) &= \frac{k^m}{(k')^{m+1}}\Theta(k'-k) + \frac{1}{2k}\delta(k-k'). && \text{(J.7)}
\end{aligned}
$$

Because the terms in $S(\omega, \omega')$ proportional to $\delta(\omega \pm \omega')$ do not contribute to the damping matrix (4.63), we can directly discard them from the definition of the

coupling constants, which are then given by

$$\begin{aligned}
G^{x*}_{km,k'l} &= \frac{k}{\ell}\delta_{l,m\pm1}\left\{i\Lambda^{(1)}_{lm}\mathcal{P}\frac{1}{k+k'}-\Lambda^{(2)}_{lm}\mathcal{P}\frac{1}{k-k'}\right\}+\delta_{l,m-1}\frac{m\pi\sqrt{kk'}}{4\ell}\\
&\times \left[\frac{(k')^m}{k^{m+1}}\Theta(k-k')+\frac{1}{2k}\delta(k-k')\right]-\delta_{l,m+1}\frac{m\pi\sqrt{kk'}}{4\ell}\\
&\times \left[\frac{k^m}{(k')^{m+1}}\Theta(k'-k)+\frac{1}{2k}\delta(k'-k)\right],\\
G^{y*}_{km,k'l} &= i\frac{k}{\ell}(\delta_{l,m-1}-\delta_{l,m+1})\left\{i\Lambda^{(1)}_{lm}\mathcal{P}\frac{1}{k+k'}-\Lambda^{(2)}_{lm}\mathcal{P}\frac{1}{k-k'}\right\}+i\delta_{l,m-1}\frac{m\pi\sqrt{kk'}}{4\ell}\\
&\times \left[\frac{(k')^m}{k^{m+1}}\Theta(k-k')+\frac{1}{2k}\delta(k-k')\right]+i\delta_{l,m+1}\frac{m\pi\sqrt{kk'}}{4\ell}\\
&\times \left[\frac{k^m}{(k')^{m+1}}\Theta(k'-k)+\frac{1}{2k}\delta(k'-k)\right], \qquad \text{(J.8)}
\end{aligned}$$

where

$$\Lambda^{(1)}_{lm}=-e^{i\pi(l+m)/2}e^{-2i\delta_m}+e^{-i\pi(l+m)/2}e^{2i\delta_l}, \qquad \Lambda^{(2)}_{lm}=e^{i\pi(l-m)/2}+e^{-i\pi(l-m)/2}e^{2i(\delta_l-\delta_m)}.$$

Bibliography

[1] H. K. Onnes, Comm. Phys. Lab. Univ. Leiden **119, 120, 122** (1911).

[2] W. Meissner and R. Ochsenfeld, Naturwiss. **21**, 787 (1933).

[3] C. J. Gorter and H. B. Casimir, Physica **1**, 306 (1934).

[4] H. London and F. London, Proc. Roy. Soc. (London) **A149**, 71 (1935).

[5] H. London and F. London, Physica **2**, 341 (1935).

[6] V. L. Ginzburg and L. D. Landau, Zh. Eksp. Theor. Phys. **20**, 1064 (1950).

[7] H. Froehlich, Phys. Rev. **79**, 845 (1950).

[8] J. Bardeen, L. N. Cooper, and J. R. Schrieffer, Phys. Rev. **108**, 1175 (1957).

[9] J. G. Bednortz and K. A. Mueller, Z. Phys. B **64**, 189 (1986).

[10] A. Schilling *et al.*, Nature **363**, 56 (1993).

[11] E. Dagotto, Rev. Mod. Phys. **66**, 763 (1994).

[12] P. W. Anderson, *The Theory of Superconductivity in High-T_c Cuprate Superconductors* (Princeton University Press, Princeton, 1997).

[13] S. A. Kivelson *et al.*, Rev. Mod. Phys. **75**, 1201 (2003).

[14] M. S. Hybertsen, M. Schlueter, and N. E. Christensen, Phys. Rev. B **39**, 9028 (1989).

[15] S. Chakravarty, B. I. Halperin, and D. R. Nelson, Phys. Rev. B **87**, 2344 (1989).

[16] B. Keimer *et al*, Phys. Rev. B **46**, 14034 (1992).

[17] F. C. Zhang and T. M. Rice, Phys. Rev. B **37**, R3759 (1988).

[18] J. Zaanen and O. Gunnarsson, Phys. Rev. B **40**, 7391 (1989).

[19] A. H. Castro Neto and C. Morais Smith, *Interacting Electrons in Low Dimensions* (Kluwer, 2003), p. 277.

[20] J. M. Tranquada *et al.*, Phys. Rev. Lett. **78**, 338 (1997).

[21] J. M. Tranquada *et al.*, Nature **375**, 561 (1995).

[22] B. Buchner *et al.*, Phys. Rev. Lett. **73**, 1841 (1994).

[23] K. Yamada *et al.*, Phys. Rev. B **70**, 897 (1998).

[24] S. R. White and D. J. Scalapino, Phys. Rev. Lett. **80**, 1272 (1998).

[25] S. R. White and D. J. Scalapino, Phys. Rev. Lett. **81**, 3227 (1998).

[26] S. R. White and D. J. Scalapino, Phys. Rev. B **61**, 6320 (2000).

[27] A. Moreo *et al.*, Phys. Rev. B **43**, 11442 (1991).

[28] H. Fehske *et al.*, Phys. Rev. B **44**, 8473 (1991).

[29] D. Poilblanc, Phys. Rev. B **52**, 9201 (1995).

[30] M. Kohno, Phys. Rev. B **55**, 1435 (1997).

[31] V. J. Emery, S. A. Kivelson, and H. Q. Li, Phys. Rev. Lett. **64**, 475 (1990).

[32] A. L. Chernyshev, A. H. Castro Neto, and A. R. Bishop, Phys. Rev. Lett. **84**, 4922 (2000).

[33] B. Normand and A. P. Kampf, Phys. Rev. B **65**, 020509 (2002).

[34] O. P. Sushkov and V. N. Kotov, Phys. Rev. B **70**, 024503 (2004).

[35] B. Normand and A. P. Kampf, Phys. Rev. B **64**, 024521 (2001).

[36] A. N. Lavrov, Y. Ando, S. Komiya, and I. Tsukada, Phys. Rev. Lett. **87**, 017007 (2001).

[37] S. Wakimoto *et al.*, Phys. Rev. B **60**, R769 (1999).

[38] S. Wakimoto *et al.*, Phys. Rev. B **61**, 3699 (2000).

[39] M. Matsuda *et al.*, Phys. Rev. B **62**, 9148 (2000).

[40] S. Wakimoto *et al.*, Phys. Rev. B **65**, 064505 (2002).

[41] N. Hasselmann, A. H. Castro Neto, C. Morais Smith, and Y. A. Dimashko, Phys. Rev. Lett. **82**, 2135 (1999).

[42] S. Klee and A. Muramatsu, Nucl. Phys. B **473**, 539 (1996).

[43] N. Hasselmann, A. H. Castro Neto, and C. Morais Smith, Europhys. Lett. **56**, 870 (2001).

[44] N. Hasselmann, A. H. Castro Neto, and C. Morais Smith, Phys. Rev. B **69**, 014424 (2004).

[45] O. P. Sushkov and V. N. Kotov, Phys. Rev. Lett. **94**, 097005 (2005).

[46] A. Gozar, S. Komiya, Y. Ando, and G. Blumberg, *Frontiers in Magnetic Materials* (Springer-Verlag, 2005), p. 755.

[47] Y. Ando *et al.*, Phys. Rev. Lett. **88**, 137005 (2002).

[48] M. A. Kastner, R. J. Birgeneau, G. Shirane, and Y. Endoh, Rev. Mod. Phys. **70**, 897 (1998).

[49] Y. Endoh *et al*, Phys. Rev. B **37**, 7443 (1988).

[50] D. Vaknin *et al*, Phys. Rev. Lett. **58**, 2802 (1987).

[51] T. Thio *et al*, Phys. Rev. B **38**, R905 (1988).

[52] T. Thio and A. Aharony, Phys. Rev. Lett. **73**, 894 (1994).

[53] W. Koshibae, Y. Ohta, and S. Maekawa, Phys. Rev. B **50**, 3767 (1994).

[54] L. Shekhtman, O. Entin-Wohlman, and A. Aharony, Phys. Rev. Lett. **69**, 836 (1992).

[55] J. Stein, O. Entin-Wohlman, and A. Aharony, Phys. Rev. B **53**, 775 (1996).

[56] S. Sachdev, *Quantum Phase Transitions* (Cambridge University Press, New York, 2001).

[57] A. V. Chubukov, S. Sachdev, and J. Ye, Phys. Rev. B **49**, 11919 (1994).

[58] A. N. Bogdanov *et al.*, Phys. Rev. B **66**, 214410 (2002).

[59] A. Auerbach, *Interacting Electrons and Quantum Magnetism* (Springer-Verlag, New York, 1994).

[60] J. Chovan and N. Papanicolaou, Eur. Phys. J. B **17**, 581 (2000).

[61] L. Benfatto, M. B. Silva Neto, V. Juricic, and C. Morais Smith, Physica B **xx**, xxxxx (2006).

[62] M. B. Silva Neto, L. Benfatto, V. Juricic, and C. Morais Smith, Phys. Rev. B **73**, 045132 (2006).

[63] N. Petropoulos, hep-ph/0402136 (2004).

[64] V. Yu. Irkhin and A. A. Katanin, Phys. Rev. B **57**, 379 (1998).

[65] B. Keimer *et al*, Zeit. f. Phys. B **91**, 373 (1993).

[66] V. Juricic, M. B. Silva Neto, and C. Morais Smith, Phys. Rev. Lett. **96**, 077004 (2006).

[67] F. C. Chou *et al.*, Phys. Rev. Lett. **71**, 3671 (1993).

[68] F. Borsa *et al.*, Phys. Rev. B **52**, 7334 (1995).

[69] Y. C. Chen *et al.*, Phys. Rev. B **51**, 3671 (1995).

[70] P. Anderson, Science **235**, 1196 (1987).

[71] B. Shraiman and E. D. Siggia, Phys. Rev. Lett. **61**, 467 (1988).

[72] W. F. Brinkman and T. M. Rice, Phys. Rev. B **2**, 1324 (1970).

[73] B. Shraiman and E. D. Siggia, Phys. Rev. Lett. **62**, 1564 (1989).

[74] A. Auerbach and B. E. Larson, Phys. Rev. B **43**, 7800 (1991).

[75] H. Mori and M. Hamada, Phys. Rev. B **48**, 6242 (1993).

[76] J. Igarashi and P. Fulde, Phys. Rev. B **45**, 10419 (1992).

[77] A. V. Chubukov and K. A. Musaelian, Phys. Rev. B **51**, 12605 (1995).

[78] V. N. Kotov and O. P. Sushkov, Phys. Rev. B **70**, 195105 (2004).

[79] B. Shraiman and E. D. Siggia, Phys. Rev. B **46**, 8305 (1992).

[80] A. Gozar *et al.*, Phys. Rev. Lett. **93**, 027001 (2004).

[81] L. Benfatto and M. B. Silva Neto, cond-mat/0602419 (2006).

[82] B. Lake *et al.*, Nature **400**, 43 (1999).

[83] H. Kawamura, J. Phys. Condens. Matt. **10**, 4707 (1998).

[84] A. Pelisseto and E. Vicari, Phys. Rep. **368**, 549 (2002).

[85] B. Delamotte, D. Mouhanna, and M. Tissier, Phys. Rev. B **69**, 134413 (2004).

[86] B. I. Shraiman and E. D. Siggia, Phys. Rev. Lett. **60**, 740 (1988).

[87] C. L. Kane, P. A. Lee, T. K. Ng, B. Chakraborty, and N. Read, Phys. Rev. B **41**, 2653 (1990).

[88] H. J. Schulz, Phys. Rev. Lett. **65**, 2462 (1990).

[89] Z. J. Weng, Phys. Rev. Lett. **66**, 2156 (1991).

[90] H. Mori and M. Hamada, Phys. Rev. B **48**, 4262 (1993).

[91] T. Dombre and N. Read, Phys. Rev. B **39**, 6797 (1989).

[92] W. Apel, M. Wintel, and H. U. Everts, Zeit. f. Phys. B **86**, 139 (1992).

[93] P. Azaria, B. Delamotte, and D. Mouhanna, Phys. Rev. Lett. **68**, 1762 (1992).

[94] P. Azaria, B. Delamotte, and D. Mouhanna, Phys. Rev. Lett. **70**, 2483 (1993).

[95] P. Azaria, B. Delamotte, and T. Jolicoeur, Phys. Rev. Lett. **64**, 3175 (1990).

[96] P. Azaria, B. Delamotte, and T. Jolicoeur, Nucl. Phys. B **408**, 485 (1993).

[97] M. Wintel, H. U. Everts, and W. Apel, Europhys. Lett. **25**, 711 (1994).

[98] H. Kawamura and S. Miyashita, J. Phys. Soc. Jpn. **53**, 4138 (1984).

[99] B. Southern and P. Young, Phys. Rev. B **48**, 13170 (1993).

[100] M. Wintel, H. U. Everts, and W. Apel, Phys. Rev. B **52**, 13480 (1995).

[101] M. Caffarel, P. Azaria, B. Delamotte, and D. Mouhanna, Phys. Rev. B **64**, 014412 (2001).

[102] A. M. Polyakov, Phys. Lett. B **59**, 79 (1975).

[103] J. Kosterlitz and D. Thouless, J. Phys. C **6**, 1181 (1973).

[104] A. O. Caldeira and A. J. Leggett, Ann. Phys. (N. Y.) **149**, 374 (1983).

[105] A. O. Caldeira and A. J. Leggett, Physica A **121**, 587 (1983).

[106] A. H. Castro Neto and A. O. Caldeira, Phys. Rev. Lett. **67**, 1960 (1991).

[107] A. H. Castro Neto and A. O. Caldeira, Phys. Rev. B **46**, 8858 (1992).

[108] A. H. Castro Neto and A. O. Caldeira, Phys. Rev. E **48**, 4037 (1993).

[109] A. V. Ferrer and A. O. Caldeira, Phys. Rev. B **61**, 2755 (2000).

[110] R. Rajaraman, *Solitons and instantons* (North-Holland, Amsterdam, 1982).

[111] P. M. Morse and H. Feshbach, *Methods of Theoretical Physics* (McGraw-Hill, New York, 1953).

[112] R. P. Feynman and F. L. Vernon, Ann. Phys. (N. Y.) **24**, 118 (1963).

[113] K. Gottfried, *Quantum Mechanics I* (Benjamin, New York, 1966).

[114] H. Takagi *et al.*, Phys. Rev. Lett. **69**, 2975 (1992).

[115] Y. Ando *et al.*, Phys. Rev. Lett. **93**, 267001 (2004).

[116] V. N. Kotov and O. P. Sushkov, Phys. Rev. B **72**, 184519 (2005).

[117] M. B. Silva Neto, cond-mat/0602492 (2006).

Summary

In this thesis, the magnetic and the transport properties of $La_{2-x}Sr_xCuO_4$ in the undoped and lightly doped regime are investigated.

In Chapter 2, we consider the role of the Dzyaloshinskii-Moriya and the pseudodipolar interactions in determining the magnetic properties of the undoped material, La_2CuO_4. Our work is motivated by recent experiments, which show a complete anisotropy in the magnetic susceptibility response of the undoped, as well as of the lightly doped compound, for $x = 1\%, 2\%, 3\%$, and 4%, up to temperatures as high as 400K. We start with the microscopic spin model, which, besides the Heisenberg superexchange interaction, contains the anisotropic Dzyaloshinskii-Moriya and the pseudodipolar interactions, introduced by the crystal structure and the spin-orbit coupling present in the material. In order to study the long-wavelength dynamics of the magnetic excitations of the system, we map this microscopic model into a corresponding field theory, which turns out to be a generalized nonlinear sigma model. The effect of the anisotropies is to introduce gaps for the spin excitations, which are responsible for the ground-state properties of the material, in particular, for the orientation of the staggered magnetization along the b orthorhombic axis and the weak ferromagnetic moment perpendicular to the CuO_2 planes. We then consider the effect of a magnetic field applied to the system. In this case, the Dzyaloshinskii-Moriya anisotropy leads to an unexpected linear coupling of the staggered magnetization to the magnetic field, which is responsible for a completely anisotropic magnetic susceptibility, in agreement with experiments.

In Chapter 3, we investigate the effect of the Dzyaloshinskii-Moriya and the pseudodipolar anisotropies on the magnetism when Sr doping is introduced in La_2CuO_4, i.e., La^{3+} is replaced by Sr^{2+}. Our starting point is the nonlinear sigma model, which includes these anisotropies, and was employed in the previous chapter for describing the magnetism in the undoped compound. The dopant holes are represented via an effective dipole field which couples to the background magnetization current, and frustrates the underlying antiferromagnetic order. We first consider the effect of the doping in the antiferromagnetic phase, $x < 2\%$. The dipole-magnetization current coupling leads to a decrease of the spin gaps, as well as of the spin stiffness, but the magnetic susceptibility response is qualitatively the same as in the undoped compound. We calculate the reduction of the Dzyaloshinskii-Moriya gap with the doping, and obtain a result which is in good agreement with recent Raman scattering experiments. The Dzyaloshinskii-Moriya gap gives rise to the stability of the antiferromagnetic state up to the doping level $x_{AF} \simeq 2\%$, at which the dipole field acquires a non-zero expectation value, causing a change in the magnetic ground state of the system. Beyond this doping concentration, in the spin-glass phase, the spins rearrange to form an incommensurate helicoidal state, which is characterized by the pitch along the b orthorhombic axis and the staggered magnetization rotating in the ac plane. Besides the helicoidal component, the staggered magnetization has a dominant component in the b orthorhombic direction, which gives rise to a total staggered magnetization oriented in the same direction. The incommensurability of the helicoidal state gives rise to two incommensurate peaks along the b orthorhombic axis in the spin-glass phase of $La_{2-x}Sr_xCuO_4$, as observed by neutron scattering experiments. The incommensurability is related to the doping and the

pseudodipolar gap in a way that allows us to explain the linear doping dependence of the incommensurability at higher doping, inside the spin-glass phase, as well as the deviation from the linear behavior at the onset of this phase. Based on this result, we show that the recovery of the linear doping dependence of the incommensurability coincides with the vanishing of the pseudodipolar gap, which is a theoretical prediction that remains to be verified experimentally. We also consider the behavior of the incommensurability in a magnetic field applied perpendicularly to the CuO_2 planes, and propose a measurement of the doping dependence of the incommensurability in the magnetic field as a "smoking-gun" experiment that would discriminate between the helicoidal and the stripe scenarios in the spin-glass phase of $La_{2-x}Sr_xCuO_4$.

In Chapter 4, we study the dynamics of topological defects of a frustrated spin system displaying spiral or helicoidal order. As a starting point we consider the $SO(3)$ nonlinear sigma model to describe long-wavelength fluctuations around the noncollinear spin state. This model allows for topologically nontrivial static solutions of the equations of motion, associated with the change of chirality (clockwise or counterclockwise) of the noncollinear state. We consider two types of these topological defects, single vortices and vortex-antivortex pairs, and quantize the corresponding solutions by generalizing the semiclassical approach to a non-Abelian field theory. The use of the collective coordinates allows us to represent the defect as a particle coupled to a bath of harmonic oscillators, which can be integrated out employing the Feynman-Vernon path-integral formalism. The resulting effective action for the defect indicates that its motion is damped due to the scattering by the magnons. We derive a general expression for the damping coefficient of the defect, and evaluate its temperature dependence in both cases, for a single vortex and for a vortex-antivortex pair. Finally, motivated by recent experiments, we consider an application of the model for describing the transport in lightly doped $La_{2-x}Sr_xCuO_4$. By assuming that the dopant holes are attached to the defects, the calculated damping coefficient is related to the the dc resistivity, which exhibits an anisotropy and temperature dependence in agreement with experimental data for $150\text{K} < T < 300\text{K}$.

Samenvatting

In dit proefschrift bestuderen we de magnetische en elektrische geleidingseigenschappen van zowel ongedopeerd als licht gedopeerde $La_{2-x}Sr_xCuO_4$.

In hoofdstuk 2 beschouwen we de rol die de Dzyaloshinskii-Moriya en pseudo-dipolaire interacties spelen bij de magnetische eigenschappen van het ongedopeerde La_2CuO_4. Ons werk is gemotiveerd door recente experimenten die een sterke anisotropie hebben geobserveerd van de respons van de magnetische susceptibiliteit in de ongedopeerde en licht gedopeerde verbinding [*compound*] bij temperaturen tot wel 400K. Ons uitgangspunt is het microscopische spinmodel dat naast de Heisenberg superexchange-interactie ook de anisotrope Dzyaloshinskii-Moriya- en pseudo-dipolaire interacties bevatten die worden veroorzaakt door de kristalstructuur en de spin-baan koppeling van het materiaal.

Om de dynamische eigenschappen van de magnetische excitaties van het systeem bij lange golflengtes te kunnen bestuderen maken we gebruik van een veldentheoretische beschrijving van het microscopische model. Deze veldentheorie blijkt een gegeneraliseerd niet-linear sigma model te zijn.

Door de anisotropie krijgen de spinexcitaties, die verantwoordelijk zijn voor de eigenschappen van de grond-toestand, een energiesprong [*gap*]. In het bijzonder beinvloedt dit de orientatie van de wisselende magnetisatie [*staggered magnetization*] langs de b-orthorhombische as en het zwakke ferromagnetisch moment dat loodrecht staat op de CuO vlakken.

In dit geval leidt de Dzyaloshinskii-Moriya anisotropie tot een onverwachte lineare koppeling van de wisselende magnetisatie en het magneetveld. Hierdoor ontstaat een volledig anisotrope magnetische susceptibiliteit, in overeenstemming met de experimenten.

In hoofdstuk 3 onderzoeken we het effect van de Dzyaloshinskii-Moriya en de pseudo-dipolaire anisotropieen op de magnetische eigenschappen van La_2CuO_4 zodra we Sr dopering introduceren, d.w.z. we vervangen La^{3+} door Sr^{2+}. Ons uitgangspunt is het niet-lineaire sigma-model dat deze anisotropieën in rekening brengt en dat we in het vorige hoofdstuk hebben gebruikt voor de beschrijving van de ongedopeerde verbinding.

De gedopeerde gaten [*holes*] worden beschreven door middel van een effectief dipoolveld dat gekoppeld is aan de achtergrond-magnetisatiestroom en de onderliggende antiferromagnetische ordening frustreert. Allereerst bekijken we het effect van de dopering in de antiferromagnetische fase, waar $x < 2\%$. De dipool-magnetisatiestroomkoppeling leidt tot een afname van de spin energiesprongen en een afname van de spin-stijfheid. Echter, de respons van de magnetische susceptibiliteit is kwalitatief hetzelfde als die van de ongedopeerde verbinding. We berekenen de afname van de Dzyaloshinskii-Moriya energiesprong als functie van de dopering en het resultaat stemt overeen met recente Raman-verstrooingsexperimenten.

De Dzyaloshinskii-Moriya energiesprong zorgt voor de stabiliteit van de antiferromagnetische toestand tot een doperingsconcentratie van $x_{\rm AF} \simeq 2\%$, alwaar het dipool veld een verwachtingswaarde ongelijk nul krijgt, hetgeen een verandering in de magnetische grond-toestand teweeg brengt.

Voor grotere waarden van de doperingsconcentratie, in de spin-glasfase [*spin-glass*], hergroeperen de spins zich en vormen ze een niet commensurabele [*incommensurate*] helicoidale, toestand die wordt gekarakteriseerd door de hoogte [*pitch*] langs de b-orthorhombische

as en de wisselende magnetisatie roterend in het ac vlak. Naast de helicoidale component heeft de wisselende magnetisatie een dominante component in de b-orthorhombische richting. De incommensurabiliteit van de helicoidale toestand is verantwoordelijk voor twee incommensurabele pieken langs de b-orthorhombische as in de spin-glasfase van $La_{2-x}Sr_xCuO_4$ zoals is geobserveerd is in neutronenverstrooiing-experimenten. De incommensurabiliteit is gerelateerd aan de dopering en de pseudodipolaire energiesprong en geeft een verklaring voor de lineare doperings afhankelijkheid van de incommensurabiliteit bij hoge doperingen in de spin-glasfase en van de afwijking van dit lineare gedrag bij het opkomen van deze fase. Gebaseerd op dit resultaat laten we zien dat het herstel van het lineare doperingsgedrag van de incommensurabiliteit samenvalt met het verdwijnen van de dipolaire energiesprong. Deze theoretische voorspelling dient nog experimenteel geverifieerd te worden.

Ook beschouwen we het gedrag van de incommensurabiliteit in een extern magneetveld dat loodrecht op de CuO_2 vlakken staat en we stellen voor om de doperings afhankelijkheid van de incomensurability te meten. Zo'n meting fungeert als een "smoking gun" experiment dat een onderscheid kan maken tussen de helicoidale en streepscenarios [*stripe*] in de spin-glasfase van $La_{2-x}Sr_xCuO_4$.

In hoofdstuk 4 bestuderen we de dynamische eigenschappen van de topologische defecten van een gefrustreerd spin systeem dat spirale of helicoidale ordening vertoont. Als uitgangspunt beschouwen we het SO3 niet-lineaire sigma model om de lange-golflengtefluctuaties van de anti-collineaire spin toestand te beschrijven. Dit model beschrijft topologisch niettriviale statische oplossingen van de bewegingsvergelijkingen die geassocieerd worden met de verandering van de chiraliteit van de anti-collineare toestand.

We beschouwen twee types van deze topologische defecten, namelijk, losse vortices en vortex-antivortexparen en we kwantiseren de de corresponderende oplossingen door de semi-klassieke aanpak te generalizeren naar een niet-abelse veldentheorie.

Door de invoering van de collectieve coördinaten kunnen we defecten voorstellen als één deeltje dat gekoppeld is aan een bad van oscillatoren die we vervolgens kunnen uitintegreren door gebruik te maken van het Feynman-Vernon pad-integraal formalisme.

De resulterende effectieve actie van de defecten laat zien dat de beweging van het defect gedempt wordt door de verstrooing van magnonen [*magnons*]. We leiden een algemene uitdrukking af voor de dempingscoëfficiënt van het defect en we evalueren de temperatuurafhankelijkheid in beide gevallen van een losse vortex en een vortex-antivortexpaar.

Tenslotte, gemotiveerd door recente experimenten beschouwen we de geleidings eigenschappen van licht gedopeerd $La_{2-x}Sr_xCuO_4$ als een toepassing van het model. Door aan te nemen dat de gedopeerde gaten zich hechten aan de defecten wordt de berekende dempingscoefficient gerelateerd aan de gelijkstroom-weerstand welke een anisotropie en temperatuurafhankelijkheid vertoont, in overeenstemming met de experimentele data voor $150K < T < 300K$.

Curriculum Vitae

I was born in Smederevska Palanka, Serbia, on June 4$^{\text{th}}$, 1976. After completing high school in Velika Plana in 1995, I began my undergraduate studies at the Faculty of Physics of the University of Belgrade. I graduated in 1999 with the thesis "Gravitational Kinks" under the supervision of Prof. Milovan Vasilić. The same year I began Master's studies in Elementary Particles Theory. I received the Master's degree with the thesis "Canonical Method of Bosonization of Two-Dimensional Systems" under the supervision of Prof. Branislav Sazdović. In 2002, I joined the group of Prof. Cristiane Morais Smith at University of Fribourg, Switzerland, to pursue my Ph.D. studies. In 2004, I moved to Utrecht, where I continued to work with Prof. Cristiane Morais Smith. The results of my research are presented in this thesis. During my Ph.D. studies, I presented my work at several conferences and workshops, among which

1. Swiss Workshop on Materials with Novel Electronic Properties, September-October 2003, Les Diablerets, Switzerland,

2. "Rencontre Romande sur les Systèmes Fortement Corrélés", November 2003, Neuchatel, Switzerland,

3. XXIX Conference of the Middle European Cooperation in Statistical Physics, March 2004, Bratislava, Slovakia,

4. Workshop "Complex Behavior in Correlated Electron Systems", August 2005, Leiden, The Netherlands,

5. March Meeting of the American Physical Society, March 2006, Baltimore, United States.

I also participated at the "Enrico Fermi" summer school in Varenna, Italy, in 2003. I was invited to presented my work at several universities and research institutes:

1. Lorentz Institute, Leiden University, The Netherlands (2003, 2005),

2. Institute of Physics, University of Belgrade, Serbia (2004),

3. Material Science Center, Groningen University, The Netherlands (2005),

4. Brookhaven National Laboratory, United States (2006),

5. Physics Department, Boston University, United States (2006),

6. Physics Department, Harvard University, United States (2006).

I have been a teaching assistant for several courses in Fribourg and Utrecht.

I will continue my career as a postdoctoral fellow in the group of Prof. Igor Herbut at the Simon Fraser University in Vancouver, Canada, starting in September 2006.

Publication List

- V. Juricic, M. B. Silva Neto, and C. Morais Smith
Lightly Doped $La_{2-x}Sr_xCuO_4$ as a Lifshitz helimagnet
Phys. Rev. Lett. **96**, 077004 (2006).

- M. B. Silva Neto, L. Benfatto, V. Juricic, and C. Morais Smith
Magnetic susceptibility anisotropies in a two-dimensional quantum Heisenberg antiferromagnet with Dzyaloshinskii-Moriya interactions
Phys. Rev. B **73**, 045132 (2006).

- L. Benfatto, M. B. Silva Neto, V. Juricic, and C. Morais Smith
Derivation of the generalized non-linear sigma model in the presence of the Dzyaloshinskii-Moriya interaction
Physica B (2006) (article in press).

- V. Juricic, L. Benfatto, A. O. Caldeira, and C. Morais Smith
Dissipative Dynamics of Topological Defects in Frustrated Heisenberg Spin Systems
Phys. Rev. B **71**, 064421 (2005).

- V. Juricic, L. Benfatto, A. O. Caldeira, and C. Morais Smith
Dynamics of Topological Defects in a Spiral: a Scenario for the Spin-Glass Phase of Cuprates
Phys. Rev. Lett. **92**, 137202 (2004).

- V. Juricic and B. Sazdovic
Thirring Sine-Gordon Relationship by Canonical Methods
Eur. Phys. J. C **32**, 443 (2004).

- D. Makogon, V. Juricic, and C. Morais Smith
Transport Properties of a Luttinger Liquid in the presence of several time-dependent impurities
Preprint.

- V. Juricic, M. B. Silva Neto, and C. Morais Smith
Stripes Versus Spirals in Lightly Doped $La_{2-x}Sr_xCuO_4$
In preparation.

Acknowledgements

During four years I was in Fribourg and Utrecht many people supported me to get through the process of acquiring Ph.D. degree. It is my pleasure to acknowledge them.

First of all, I am greatly indebted to Prof. Cristiane de Morais Smith for her scientific and moral support during the time I spent in Fribourg and Utrecht. She introduced me to the physics of high-temperature superconductors which was a completely new area for me at the time I started my PhD studies. She was a brilliant supervisor and her ideas profoundly influenced my work during these four years. Thanks Cristiane!

I would like to express my gratitude to Dr. Marcello Barbosa da Silva Neto, who was a post-doc in the group, and with whom I worked for a few months in Fribourg and two years in Utrecht. It was a great pleasure working with Marcello whose ideas had great impact on the work presented in this thesis. I am also greatly indebted to Dr. Lara Benfatto, who was a post-doc in the group during the two years I spent in Fribourg. Lara's inspirational ideas, as well as invaluable discussions with her, greatly contributed to the shape of this work. A collaboration with Prof. Amir Caldeira is also greatly acknowledged. I wish to acknowledge all the people in Cristiane's group, especially Dr. Ricardo Doretto for carefully reading the thesis and giving many helpful suggestions. Special thanks to Hosana Celeste who designed the cover of this thesis.

During my stay in Fribourg I had a great pleasure to meet Vladimir Gritsev with whom I had many discussions and became a great friend. Sharing the office with Mark Görbig was also a great experience. I also wish to thank Leo Tincani.

From the people in the Netherlands, I would like to acknowledge Dennis Dickerscheid for being more than a friend. Thanks to Aleksandar Perić and Jelena Mihajlović for their support and the great time we spent together mostly in Rotterdam. Hvala, Periša!! Hvala, Jelo!! I had a great pleasure to share the house for almost a year with Nabila Bardine whose help and support were invaluable. Merçi beaucoup, Brate!!! I would also like to thank Vladimir Cvetković and Jelena Bogdanović for the time we spent together in Leiden and Utrecht. It was a great pleasure sharing the office for two years in Utrecht with Henk Vocks.

I wish to thank Dunja Popović who is "responsible" for my coming to Fribourg, and more than that.

Last, but not least, I would like to thank Sina Lenherr for her support and unforgettable times we spent together in Fribourg and Utrecht.